Petrological evolution of the Middle Triassic Predazzo Intrusive Complex, Italian Alps

Journal:	*International Geology Review*
Manuscript ID	TIGR-2017-0107.R3
Manuscript Type:	Data Article
Date Submitted by the Author:	n/a
Complete List of Authors:	Casetta, Federico; Universita degli Studi di Ferrara Dipartimento di Fisica e Scienze della Terra, Coltorti, Massimo; Universita degli Studi di Ferrara Dipartimento di Fisica e Scienze della Terra, Department of Physics and Earth Sciences Marrocchino, Elena; Universita degli Studi di Ferrara Dipartimento di Fisica e Scienze della Terra
Keywords:	Predazzo Intrusive Complex, Caldera collapse, Triassic shoshonitic magmatism, Multi-pulse intrusion

Petrological evolution of the Middle Triassic Predazzo Intrusive Complex, Italian Alps

Federico Casetta*

Department of Physics and Earth Sciences, University of Ferrara

Via Saragat 1, 44121 Ferrara, Italy

Massimo Coltorti

Department of Physics and Earth Sciences, University of Ferrara

Via Saragat 1, 44121 Ferrara, Italy

Elena Marrocchino

Department of Physics and Earth Sciences, University of Ferrara

Via Saragat 1, 44121 Ferrara, Italy

* Corresponding author.

Phone +39 0532 974721.

E-mail: cstfrc@unife.it

Petrological evolution of the Middle Triassic Predazzo Intrusive Complex, Italian Alps

Abstract

The Predazzo Intrusive Complex (PIC), a Ladinian plutonic body located in the Southern Alps (NE Italy), is made up of a 4.5 km^3 gabbroic to syenitic and syenogranitic intrusion, basaltic to latitic volcanic products (about 6 km^3 in volume) and by an extended dike swarm intruding both intrusive and volcanic rocks. An extensive field survey of the complex, followed by detailed petrographic and geochemical analyses, allowed the identification of three different magmatic units: a Shoshonitic Silica Saturated Unit (SS), 3.1 km^3 in volume, a Shoshonitic Silica Undersaturated Unit (SU), 0.3 km^3 in volume, and a Granitic Unit (GU), 1.1 km^3 in volume. K-affinity, marked Nb and Ti negative anomalies and a strong Pb enrichment are distinctive markers for all PIC lithotypes. A general HFSE (Th, U, Pb), LREE (La, Ce, Pr, Nd) and Na enrichment characterises the SU suite with respect to the SS series. Mass balance calculations, based on major and trace element whole rock and mineral compositions, have been used to simulate the fractionation process of SS and SU suites, showing (i) the complexity of the evolutionary stages of the PIC and (ii) the analogy between the calculated subtracted solid assemblages and the natural cumulitic lithotypes outcropping in the area. The field relationships between the various portions of the intrusive complex, the volcanic products and the dike swarm define the temporal evolution of the PIC, in which the SS magma batch was followed by the GU and later on by the SU intrusion. The presence, in both eastern and western portions of the complex, of a transitional magmatic contact between the intrusive rocks of the SS suite and the volcanics is not in favour of the hypothesis of a caldera collapse to explain the ring-like shape of the PIC.

Keywords

Predazzo Intrusive Complex; Caldera collapse; Triassic shoshonitic magmatism; Multi-pulse intrusion

1. Introduction

The Predazzo Intrusive Complex (PIC), together with Mt. Monzoni and Cima Pape areas, represents one of the main intrusive expressions of the Triassic magmatism within the Dolomites (Southern Alps domain, Italy), which is strongly dominated by the presence of volcanics and dikes throughout all the Schlern/Seiser Alm (NW) and the Cadore (NE) regions (Figure 1). This ring-shaped intrusive body is surrounded by a large amount of volcanic products, covering an area of nearly 25 km^2. PIC is a Late Ladinian complex (237.3 ± 1.0 Ma) intruded in Permian to Middle Triassic volcanic and sedimentary formations (Mundil *et al*., 1996; Brack *et al*., 1996, 1997, 2005; Mietto *et al*., 2012). The occurrence of a well-defined metamorphic contact and the relationships between the igneous rocks and the surrounding limestones attracted the interest of scientists since the XIX century, making the Predazzo - Mt. Monzoni volcano-plutonic area one of the main subjects of the debate on the origin of igneous rocks, also known as the neptunistic - plutonistic controversy (Fondazione Dolomiti UNESCO). Mt. Monzoni intrusion played also a central role for the development of the petrography, giving the name to the monzonitic rocks themselves. Many petrological studies were carried out in order to explain the orogenic character of these complexes and the intrusion sequence: the clearly shoshonitic affinity of the Middle Triassic magmatism, both in effusive, subvolcanic and intrusive terms, is in fact concomitant with the general anorogenic tectonic regime of the region during the Ladinian (Rossi *et al*., 1976; Castellarin, 1983; Bonin, 1988; Zanetti *et al*., 2013). The origin of this magmatic event was afterwards linked to an extensional tectonic regime, dominated by vertical differential movements and subsidence (Gianolla *et al*., 2010), which were able to generate shoshonitic magmas by decompression melting of a subduction-related, previously metasomatized mantle source (Sloman, 1989;

Bonadiman *et al*., 1994). After having been at the heart of the petrographic debate for decades, the study of PIC was abandoned, despite its key role in the interpretation of the Southern Alps Triassic magmatism. This volcano-plutonic complex has been in fact almost completely preserved, in both its intrusive and volcanic portions, from the action of the alpine tectonic event, resulting one of the rare places worldwide where the relationship between an ancient magma chamber, its volcanic products and the host rocks could be observed. PIC, unlike Mt. Monzoni and Cima Pape, is characterised by the presence of multiple shoshonitic silica saturated, oversaturated and undersaturated plutons, whose genetic relationships gave rise to various debates (Sloman, 1989; Bonadiman *et al*., 1994; Menegazzo Vitturi *et al*., 1995; Visonà, 1997; Marrocchino *et al*., 2002). The present study is aiming at a complete geological and petrological reconstruction of the complex, which can also foster a deeper understanding of the Triassic magmatism in the Southern Alps. Detailed field survey and sampling, togheter with an accurate petrological investigations (whole rock and mineral major/trace element analyses) on more than 180 samples, were carried out in order to define i) the differentiation processes occurring within the feeding system, ii) the relationships between the various intrusive bodies and iii) their petrological signature.

2. Geological setting and geodynamic

At the end of the Hercynian orogenesis, the Dolomitic Area was initially involved in a ductile tectonic regime, characterised by greenschist facies metamorphism, and then uplifted and eroded (Gianolla *et al*., 2010). During this period, the Southern Alps were involved in a continental rifting phase (Doglioni and Bosellini, 1987; Bertotti *et al*., 1993) with a gradual, asymmetric, passive extension of the European and African continental lithosphere (Lemoine *et al*., 1987; Piccardo *et al*., 1994). Permian intrusions, such as the Ivrea-Verbano Mafic Complex (Western Alps, Italy, Quick *et al*., 2003; Sinigoi *et al*., 2011, 2016), Mt. Cervino (Western Alps, Italy) and Mt. Collon (Western Alps, Switzerland), are the result of extension-

related mantle partial melting as consequence of the thinning of the continental lithosphere displaced along a master detachment fault at the northwestern margin of the future Adria plate (Dal Piaz, 1993). This event was characterised by the activation of a brittle/ductile intra-lithospheric shear zone, thermal perturbations connected with mantle-derived basic intrusions in the lower crust, and hybrid anatectic to mafic-derived acidic magmatism in the upper crust (Barth *et al*., 1993; Quick *et al*., 2003; Marocchi *et al*., 2008; Sinigoi *et al*., 2016). Passive mechanisms for the extension of the subcontinental lithospheric mantle have been also proposed for the onset of the Ligure-Piemontese oceanic basin (Beccaluva *et al*., 1984), associated with precursory Permian magmatic episodes (Rampone and Piccardo, 2000). The mature stage of the continental rifting is marked by Middle-Late Triassic widespread deposition of shallow-water carbonates and by the development of narrow seaways (Scandone, 1975; Gianolla, 2011). Several Triassic magmatic occurrences (Figure 1), mostly intercalated within the sedimentary sequence, are reported from the western margins of the Adria plate (Sicily, Calabria, Sardinia, Tuscany and Liguria) and the eastern Dynarides-Hellenides orogenic belts, these latter being characterised by calc-alkaline to shoshonitic affinity (Beccaluva *et al*., 2005).

The Triassic magmatism (Table 1) is also widely represented among the entire Southern Alps, from the Brescian Alps (Cassinis *et al*., 2008) and the Alto Vicentino Area (Bellieni *et al*., 2010), towards the Dolomitic Area, the Carnia region (Gianolla, 1992; Brack *et al*., 2005) and the Karavanke ragion in Austria (Lippolt and Pidgeon, 1976; Bellieni *et al*., 2010).

The Dolomitic Area represents a large part of the Southern Alps, and was characterised, during the Ladinian, by the presence of isolated carbonatic platforms, elevated over deep marine basins, formed as a conseguence of the extensional tectonic regime. Evidence for volcanic activity during the Ladinian and Carnian may be found, as above mentioned, throughout the Southern Alps, even if its main expressions developed in the western Dolomites (Salomon, 1895; Cornelius and Cornelius-Furlani, 1924; Vardabasso, 1929, 1930;

Leonardi, 1968; Brondi *et al*., 1977; Calanchi *et al*., 1977, 1978; Pisa *et al*., 1979; Castellarin *et al*., 1980; Lucchini *et al*., 1982; Sloman, 1989; Gianolla *et al*., 2010), where a thick sequence of calc-alkaline to shoshonitic subaerial lavas, pillow lavas, lava breccias, hyaloclastites and volcanoclastic sandstones, with associated intrusive bodies (PIC, Cima Pape and Mt. Monzoni) and dike swarms can be found (Bonadiman *et al*., 1994; Beccaluva *et al*., 1996; Coltorti *et al*., 1996; Gianolla, 2011). The orogenic affinity of this magmatism, contrasting with the geodynamic setting of the entire Southern Alps domain during the Triassic, has been the matter of a longstanding debate (Table 1). Bernoulli and Lemoine (1980) considered this area as part of an aborted rift in a passive margin contest, while Castellarin *et al*. (1980) placed it in a compressive margin, at the northwetsern limb of the Paleo-Tethys. More recent studies invoked also the involvement of an "active" mantle upwelling (Stähle *et al*., 2001), as well as a transition to back-arc conditions started in Carboniferous-Permian times, triggered by the northward subduction of the Paleotethys remnants (Ziegler and Stampfli, 2001; Stampfli and Borel, 2002; Stampfli *et al*., 2002; Armienti *et al*., 2003; Cassinis *et al*., 2008; Schmid *et al*., 2008). In order to explain the discrepancy between the orogenic affinity of the magmas and the "anorogenic" geodynamic setting, Bonadiman *et al*. (1994) proposed a partial melting of a mantle source previously metasomatised by subduction-related components during the Hercynian orogenic cycle. On the other hand, crustal and mantle rocks of the Ivrea-Verbano Zone recorded a subduction-related signature for the Middle Triassic magmatic event (Zanetti *et al*., 2013), where the closure of the Paleotethys activated the rotation and the strike-slip displacement of several micro-plates, generating local transtensional dynamics (Doglioni, 1984, 1987; Stampfli and Borel, 2002, 2004). This type of tectonic kinematics caused the development of block-faulting, flower-type and en-enchelon structures, and the development of the magmatism along a general N70E axis. This geodynamic setting may account for the discontinuous emplacement of deep-seated to shallow levels magmas through lithospheric transtensional

faults. These contemporary evidences of extensional and compressive dynamics have therefore led to put forward the existence of a back-arc basin in the Southern Alps, linked to the Paleotethys subduction or due to the collision of Apulia and Adria plates (Stampfli and Borel, 2002, 2004; Zanetti *et al*., 2013). This setting would be also in agreement with the rapid subsidence recorded for the Dolomitic Area (Doglioni, 2007) and the orogenic affinity of the magmas (Table 1).

The first petrographic studies on PIC rocks are dated back to about 200 years ago (Marzari Pencati, 1820), when the relationship between the Triassic magmatic intrusion and the surrounding limestone was documented for the first time. Since then, several authors (Vardabasso, 1930; Paganelli and Tiburtini, 1964; Petersen *et al*., 1980; Castellarin *et al*., 1982; Lucchini *et al*., 1982; Menegazzo Vitturi *et al*., 1995; Coltorti *et al*., 1996; Visonà, 1997) identified the multi-pulse nature of the ring-like shaped intrusion and the high variability of lithotypes of which it is composed. The large compositional spectrum of PIC rocks, resulting in the presence of both quartz- and nepheline-normative lithotypes, created a large number of debates on the petrogenesis of the magmatic complex (Vardabasso, 1930; Lucchini *et al*., 1982; Menegazzo Vitturi *et al*., 1995; Coltorti *et al*., 1996; Visonà, 1997). Commonly accepted is the monzo-gabbroic (i.e. trachybasaltic) nature of the PIC parental magmas and their orogenic affinity (Bonadiman *et al*., 1994; Marrocchino *et al*., 2002). However, the presence of various differentiates (quartz- and nepheline-bearing syenites, and oversaturated granites/syenogranites), as well as of clinopyroxenitic bodies at the intrusion borders makes the genetic processes of each portion of the complex extremely controversial. As a consequence, PIC petrographic and geochemical features have been interpreted either as a result of flow differentiation or mingling processes (Lucchini and Morten, 1977; Visonà, 1997), giving rise to a large number of uncertainties on the nature of one of the longer-term studied intrusive bodies of the Southern Alps.

3. Materials and methods

Whole rock major and trace element analyses of PIC samples have been carried out at the Department of Physics and Earth Sciences (University of Ferrara, Italy).

XRF analyses on a first batch of samples was performed by Marrocchino *et al*. (2002). Further on PIC sampling was extended and a second analytical stage for major and trace elements, using a wavelength - dispersive ARL Advant'XP X-Ray fluorescence spectrometer was carried out. The full matrix correction procedure and the intensities were elaborated following Traill and Lachance (1966). Accuracy and precision are better than 2-5% for major elements and 5-10% for trace elements. The detection limit is 0.01% and 1-3 ppm for most of the major and trace element concentrations, respectively (Allahyari *et al*., 2014). Both batches of samples were compared with the same internal standards to assure the homogeneity and coherence of the results. Moreover, a set of representative samples from the first group was re-analyzed. Results indicate that differences between the two datasets are within analytical error.

Rare earth elements (REE) and Y were analysed using an inductively coupled plasma mass spectrometer (ICP-MS) VG Plasma Quad2 Plus with precision and accuracy better than 10% for all elements, well above the detection limit (see also Allahyari *et al*., 2014).

Mineral compositions were analysed at the IGG-CNR hosted at Department of Geosciences (University of Padova, Italy) using a Cameca-Camebax electron microprobe (EMP) system, operating at an accelerating voltage of 15 kV and specimen current of 15 nA with a counting time of 10s for peak and 20s for background. Natural and synthetic compounds and oxides were used as standards. Accuracy and precision were within 2% for major and 5 % for minor elements.

4. Field characters and volume estimation

The main part of PIC is made up of a monzo-gabbroic to syenitic external ring-shaped body (with minor gabbros and clinopyroxenites) and by subordinated more differentiated intrusions, outcropping in the central (granites to syenogranites) and in the eastern part of the ancient magma chamber (Figure 2). A huge amount of volcanic and volcanoclastic products, ranging in composition from basalts to latites, surrounds the intrusive portion, outcropping mainly in the northern and western sectors of the magmatic complex. A dike swarm, basaltic to trachytic in composition, variable in width from tens of centimetres to few metres and with two prevalent strike directions (NNW-SSE and E-W), cut sedimentary, volcanic and intrusive rocks. The entire complex is nowadays largely covered by vegetation, whereas during the XX century it was famous for the syenogranite quarries, as well as for the Bedovina Mine, a W, Mo, Sn, Bi, Cu, Pb, Zn, Ag, Te, Co and Ni mineralization (Frizzo *et al*., 2010) lying at the northeastern contact between PIC and the volcanic products (Figure 2).

A detailed geological survey together with an extensive sampling of the Predazzo area allowed the reconstruction of the outcrop geometries for the entire PIC, as well as the mapping of the volcanic and volcanoclastic deposits. As shown further on, this field work defined the existence of three different magmatic units. In an overall view, both intrusive and volcanic portions are exposed to the surface, making possible to study the relationship between the ancient magma chamber and the overlying extrusive rocks, mainly in the central and in the eastern parts (Figure 2). Here, in fact, the intrusion outcrops almost continuously over about 1000 m of vertical gap, preserving both its inner portions and its upper edges, where the contact with the corresponding volcanic products and the host rocks is clearly delineated. At the bottom of the PIC (about 900 m a.s.l.) the contact between the various lithotypes is well preserved: the relationships between the portions of the intrusion, as well as between them and the widespread dike swarm, contributed also to constrain the intrusive sequence that formed the magmatic complex. In addition, these intrusions show a gradual transition to the volcanic rocks over a distance of hundred metres, marked by the presence of

relatively fine-grained monzo-gabbroic to monzonitic lithotypes, with a hypabyssal texture (Figure 3). These rocks outcrop almost symmetrically above the Bedovina Mine (Mt. Mulat) on the eastern side of the complex and at the Malga Gardoné on its western side, suggesting the presence of a transitional, magmatic contact between the intrusion and the volcanics, i.e. the absence of a tectonic contact between these two lithotypes. The widespread vegetation covering the whole complex, together with the length of such transition, makes not possible to show these contacts.

For decades one of the most debated topics linked to the PIC has been the relationship between the intrusive and the volcanic portions. Due to its ring-like shape the historical definition of "Predazzo caldera" was introduced, suggesting a highly explosive volcanic event (Leonardi, 1968; Castellarin *et al*., 1982; Doglioni, 1984; Gianolla *et al*., 2010). The above-mentioned transitional contact, together with the absence of large caldera-fill deposits (Quick *et al*., 2009; Sinigoi *et al*., 2011), as clearly evidenced in the cross-section of Figure 2, cast however some doubts on the presence of a caldera structure for the Predazzo magmatic complex.

After the field survey, the use of QGis 2D and Polyworks (InnovMetrics) 3D softwares enabled us to convert the field relationships in a 3D surface model for the estimate of the volume of each portion of the complex. Due to the large volume of magmatic rocks that characterise the Predazzo complex, which is over 10 km^3 for an area of about 25 km^2, the edges of each magmatic unit within the complex were geometrically simplified to get a processable data, with an accuracy adequate for the focus of the present study. Such estimations were in fact aimed to obtain an order of magnitude for the volume of the different portions of the intrusion, as well as to develop a volumetric comparison between the intrusives and the volcanics. Results from the 3D modelling show that the entire PIC volume is $4.51 \pm 0.136 * 10^9$ m^3, i.e. about 4.5 km^3; by contrast, the volume of the volcanic deposits

(lava flows, pillow lavas, lava breccias and explosive breccias) resulted slighlty larger, being $5.97 \pm 0.179 * 10^9$ m^3, i.e. about 6 km^3.

5. Petrography and whole rock geochemistry

Previous works on PIC (Visonà, 1997; Marrocchino *et al*., 2002) proposed a subdivision into four units, named M1 (shoshonitic silica-saturated series), M2 (shoshonitic silica-oversaturated series), M3 (potassic-alkaline series) and calc-alkaline series, this latter made up only by granitic and syenogranitic lithotypes. The improvement of the sample collection carried out in the present study, as well as new petrographic and geochemical data, suggest the subdivision of PIC into three main units (Figure 2), based on the silica saturation degree and the mineral assemblages, in which M1 and M2 have been merged into a single saturated (SS) series. According to our sampling, in fact, the rare oversaturated rocks that were found scattered within the complex do not support the existence of a clearly independent series (M2), which is also in contrast with the general overlap of the petrographic and geochemical features of the two previously defined M1 and M2 series. Silica saturation, resulting in the modal and normative presence of quartz, well displayed in the QAPF diagram (Figure 4), is in fact an important discriminating factor between the three units that constitute the PIC. The Shoshonitic Silica Saturated Unit (SS) is composed of a noticeable amount of quartz (up to 15-20%) from the less differentiated monzo-gabbroic to the evolved syenitic terms, while the Granitic Unit (GU) is constituted by granites and syenogranites with up to 35-40% of quartz. On the other side, the Shoshonitic Silica Undersaturated Unit (SU) suite is nepheline-normative along the entire differentiation trend.

5.1 Petrography

Shoshonitic Silica Saturated Unit (SS)

It represents the main portion of the intrusion (67% of PIC, with a volume of about 3.1 km^3), outcropping in the external part of the plutonic ring. This unit is mainly constituted by gabbros, monzo-gabbros, monzo-diorites, monzonites and syenites, and is thought to be derived from the first magmatic pulse. The gabbros crop out at the western border of the intrusion, dark-coloured, with medium to large grain size (1.2-6.8 mm) and, in some cases, mesocumulitc texture. The most common mineral phases are slightly zoned, light green and sometimes twinned augitic clinopyroxene (Cpx), olivine (Ol) and hypersthenic orthopyroxene (Opx). The intercumulus assemblage is composed of zoned plagioclase (Plag), magnetite (Mt), quartz (Qz) and pecilitic biotite (Bt). The monzo-gabbros represent the most abundant lithotype, with fine to large grain size (0.3-6.8 mm), hypidiomorphic texture and low colour index. Peculiar is the presence of augitic Cpx showing, in some cases, incipient local replacement by brown amphibole (Amph). The primary Amph are horneblende in composition, while Ol and Opx are absent. Other common phases are Plag, minor alkali feldspar (K-feld), Bt, sometimes altered to chlorite (Chlr), and Mt. Monzo-diorites are characterised by a grain size comparable to that of monzo-gabbros, and by a slightly higher colour index. Monzonites show fine to medium grain size (0.3-4.5 mm), with large K-feld, often characterised by perthitic structure, containing other mineral phases, (i.e. Bt and Plag). The augitic Cpx is often altered, while Amph is characterised by a compositional range from horneblende (primary formed terms) to actinolite-tremolite (replacing Cpx). Qz is also present, in an amount generally between 5 and 20%. Syenites are pink coloured, with granular structure: strongly perthitic K-feld is common, even if clouded by clay alteration; Qz and Plag are smaller in size and less abundant. The only mafic phases are represented by rare Cpx, Amph and Bt. Sphene (Sph), apatite (Ap) and zircon (Zirc), considered as accessory phases in almost all lithotypes, become quite abundant in syenites. At the southern border of the intrusion, directly in contact with the SS unit, outcrops a small dark-coloured mesocumulitic clinopyroxenitic body, with grain size ranging from medium to large (1.1-6.2 mm). It is

mainly constituted by Cpx, Ol, Bt, Mt and Plag. Its cumulitic nature, together with its marginal position, suggest that these rocks represent the first minerals crystallized at the border of the SS intrusion.

The SS hypabyssal monzo-gabbros and monzonites are mainly constituted by large Plag and Cpx embedded in a microcrystalline assemblage of K-feld, Bt, Plag, Cpx and Amph. They gradually pass into the volcanic lithotypes at the eastern and western side of the complex, as it is evident in the photomicrographs of Figure 3.

Granitic Unit (GU)

It outcrops in the central part of PIC, where forms a half-ring of about 2 km^2 in extension and about 1.1 km^3 in volume (25% of the intrusion). This unit is constituted by pink granites to syenogranites, sometimes with pegmatitic facies. The most abundant phase in such rocks is large-sized perthitic K-feld, with Plag, Qz and Fe-rich Bt in decreasing order of abundance. Accessory minerals are fluorite, allanite, Ap and Zirc, these two latters being often hosted in Qz crystals. Some samples are characterised by the presence of secondary Chlr crystals, formed over Bt, as well as centimetric black aggregates of tourmaline. Paganelli and Tiburtini (1964) and Menegazzo Vitturi *et al*. (1995) reported also the presence, in some cases, of small amounts of Amph intergrew with Bt. The relationships between granites and the SS series, suggest that the GU unit was intruded after SS, representing the second magmatic pulse of the PIC.

Shoshonitic Silica Undersaturated Unit (SU)

This series, about 0.3 km^3 in volume (8% of the PIC), outcrops in the easternmost part of the intrusion. It is characterised by the abundant presence of differentiated products, with subordinate gabbros, monzo-gabbros and monzonites, all of them nepheline (Ne)-normative in composition. The most mafic rocks (gabbros and monzo-gabbros) are characterised by the

presence of Plag, K-feld, salitic/aegirinaugitic Cpx, hastingsitic/Fe-pargasitic Amph, and minor Bt and Mt. Peculiar is also the presence of ugranditic-melanitic garnet (Grt). Monzonites are characterised by the absence of Qz, and by the presence of some altered Plag and K-feld, as well as rare altered Cpx, Amph and Bt. Syenites are grey coloured, with glomeroporphiric texture, where K-feld, melanitic Grt and minor altered Plag are the dominant phases. Small crystals of dark green Cpx and brown Amph are rarely present, embedded in a fine matrix constituted by K-feld, Plag, and dark green Cpx. Sph, ilmenite, Mt, Ap and epidote are present in the less differentiated lithotypes, while in the most differentiated rocks the accessory phases are Ti-Mt and Sph. In some differentiated samples the presence of nepheline has been documented (Vardabasso, 1930; Visonà, 1997). The finding of dike with similar undersaturated affinity cutting the GU unit suggest that the SU unit was the last pulse to enter the magma chamber.

5.2 Major element geochemistry

The three main units of the PIC (SS, SU and GU) show independent geochemical behaviour, well discriminated in QAPF (Figure 4), TAS (Figure 5) and K_2O vs. SiO_2 (Figure 6) diagrams. The entire dataset is characterised by a potassic affinity (Figure 7), only a few extremely differentiated syenogranites and syenites lie in the high-K affinity field.

The SS series is composed of gabbroic (mg# = 58-59) to monzo-gabbroic (mg# = 46-64), monzo-dioritic, monzonitic and syenitic samples, with SiO_2 and K_2O contents ranging from 42 to 68 wt% and 0.3 to 8.4 wt%, respectively, and Na_2O content up to 4.3 wt% in the most differentiated samples (Supplementary Table 1). Clinopyroxenites and cumulitic gabbros are characterised by a lower silica and potassium contents, ranging from 39 to 46 wt% and from 0.3 to 0.8 wt%, respectively (Supplementary Table 2). Their affinity is potassic and fits well with the SS series, although the abundant presence of Bt results in a normative (CIPW) silica undersaturation. These cumulitic samples are characterised by the highest MgO, TiO_2, CaO,

FeO and contents (Figure 8); except for the MgO/SiO_2 ratio, all diagrams confirm their affinity to the SS series. It is very likely that they could be derived from the early stage of fractional crystallization of the SS magma (Figure 8; see discussion below).

Rocks belonging to the GU are highly differentiated granitic to syenogranitic lithotypes, with high silica (up to 76 wt%) and alkali (7 to 11 $Na_2O + K_2O$ wt%) contents; their K/Na ratio is generally similar to that of SS series, except for few samples showing a low-K content (Supplementary Table 3). Granites and syenogranites are also characterised by TiO_2 and CaO contents comparable to those of the SS syenites, whereas their low MgO/SiO_2 and high FeO/SiO_2 ratios (Figure 8) highlight their peculiar petrological behaviour.

The SU series is composed of silica-undersaturated Ne-normative lithotypes, with K_2O (from 2.2 to 9.2 wt%) and Na_2O (0.4 up to 6.3 wt%) contents higher than those of SS rocks (Supplementary Table 4). A few gabbroic (mg# = 46-56) to monzogabbroic (mg# = 44) rocks belong to this series, that is generally composed of more differentiated terms (monzonites and syenites) with respect to the SS series, where the entire fractionation sequence is commonly represented. In Figure 8, the CaO and FeO contents of the entire dataset are plotted against silica and the parallel SS and SU differentiation patterns are clearly distinguishable. At comparable differentiation degree, SU samples are in fact characterised by higher Na_2O, but lower MgO, CaO, FeO and TiO_2 contents, further supporting their origin from an independent magmatic pulse, whose fractionation trend is related to the subtraction of compositionally and modally different mineral phases (see discussion below).

5.3 Trace element geochemistry

N-MORB-normalised (Sun and McDonough, 1989) trace element distributions for PIC lithotypes are reported in Figure 9. They show a general enrichment in Low Field Strength Elements (LFSE), such as Ba, Rb, Th, U, and K, and marked negative Nb and Ti anomalies. These features, together with the late Mt crystallisation and the consequent absence of Fe-Ti

enrichment trend, as well as with Bt, Amph and K-feld modal abundances, support the affinity to the shoshonitic series from active continental margins (Ewart, 1982).

All lithotypes show a marked enrichment in Pb, which ranges in composition from 20 up to about 90 ppm. Irrespective of lithotypes, this trace element represents a discrimination feature between SS and SU series, being slightly higher in the latter. Such a large positive anomaly is peculiar of the Dolomitic Triassic magmatism, as it is often accompanied by small polymetallic copper-bearing deposits (Nimis *et al*., 2012). Bedovina Mine represents in fact one of the most famous copper-wolfram deposits of the area, where the presence of a "sulphide copper phase", i.e. chalcopyrite, pyrite, sphalerite and galena, was genetically related to the effect of late magmatic lead-enriched fluids (Frizzo *et al*., 2010). Together with Pb, all HFSE are generally enriched in SU suite with respect to SS one. Clinopyroxenites and gabbros display normalised patterns lower than monzo-gabbros, monzo-diorites and monzonites, in agreement with their cumulitic nature. Sr and Ba show a behavior shifting from incompatible in mafic and intermediate lithologies to more compatible in sialic rocks, where the content of these elements decreases, in relation to Plag and K-feld fractionation, still manteining a slight positive anomaly. Similarly, from clinopyroxenites and gabbros to syenites a negative P anomaly is recorded, probably due to Ap fractionation. Extremely differentiated syenites are characterised by the highest content of incompatible elements (Rb, Th and Nb), but show moderate to strong Ba, Sr, P, Zr, Ti and Y depletions, suggesting a considerable removal of K-feld, Mt, Ap and Zirc (see discussion below).

N-MORB-normalised REE spidergrams (Sun and McDonough, 1989) show that PIC rocks are characterised by parallel but higher REE distribution (Figure 9, Supplementary Table 5) from clinopyroxenites and gabbros throughout monzo-gabbros, monzo-diorites, monzonites and syenites, as it would be expected by a normal fractionation trend. La_N/Yb_N ratio for the SS suite ranges from 5 to 7 in clinopyroxenites, up to 9 in gabbros, from 9 to 12 in monzo-gabbros and from 10 to 22 in monzo-diorites, monzonites and syenites. The SU lithotypes are

extremely enriched in LREE, with La_N/Yb_N reaching the highest values of 15-29. GU samples show a general REE enrichment, with La_N/Yb_N ranging between 8 and 21. Almost all SS and SU lithotypes, except for gabbros and clinopyroxenites, are also characterised by a negative Eu anomaly, probably related to feldspar fractionation: this anomaly, more evident in the differentiated syenite samples, is extremely marked in all GU samples.

The consistent increase of incompatible elements, like Rb, Nb, Zr, Th, Y, La, Ce, at increasing the differentiation index (SiO_2; Figure 10), is well evident. A gradual enrichment in Rb, Zr and Nb are observed both with increasing silica content and varying the serial alkalinity from SS to SU series. The highest values of Rb (ca. 330 ppm) and Zr (ca. 640 ppm) are observed in the syenitic rocks of the SU series. In Rb and Zr vs. SiO_2 diagrams (Figure 10), GU samples and clinopyroxenites plot in well separated fields. Clinopyroxenites are characterised by a Rb content below 50 ppm, while GU granites and syenogranites display higher concentrations (up to 440 ppm). At comparable SiO_2, Rb content is generally higher in the SU suite with respect to SS one. On the other hand, Zr content increases markedly from the less evolved monzo-gabbros (< 100 ppm) to SS and SU syenites, being the SU suite characterised by an average higher content. In GU lithotypes, the Zr content decreases markedly from 360 to 80 ppm with increasing silica content up to 77 wt%, probably due to Zirc fractionation.

6. Mineral chemistry

The composition of the most representative PIC mineral phases was carried out to better characterise the geochemical features of SS, SU and GU suites and to develop the mass balance fractionation model illustrated below (see also Figures 8 and 10). Fe^{2+}/Fe^{3+} ratio was stoichiometrically determined for the anhydrous phases, whereas for Amph and Bt it was calculated according to the models of Leake *et al*. (1997) and Dymek (1983) respectively.

6.1 Olivine

Ol (Supplementary Table 6), often altered to iddingsite, is present only in a few mafic samples of the SS series, like clinopyroxenites, gabbros and rare monzo-gabbros. Its compositional range varies from Fo_{62} to Fo_{38} in both gabbros and clinopyroxenites.

6.2 Magnetite

Magnetite (Figure 11, Supplementary Table 6) is characterised by an almost homogeneous composition among the three magmatic suites. The TiO_2 content is in fact always below 5 wt%, reaching its lowest values in the more differentiated samples (i. e. monzonites) as well as in the GU syenogranites, where is slightly above zero.

6.3 Pyroxenes

As for Ol, Opx (Figure 11, Supplementary Table 7) is present only in a few mafic samples of the SS series. It occurs in reaction relationship with Ol in clinopyroxenites and gabbros, and in a few cases it is also present in monzonites. Its composition ranges from En_{71-61} in clinopyroxenites, En_{69-63} in gabbros to En_{60-52} in monzonites. Cpx (Figure 11, Supplementary Table 7) is reported from both SS and SU suites, with different composition for the two suites. Cpx from SS series are quite homogeneous, being diopsidic and augitic in composition with a Wo content < 50. On the other hand, SU Cpx show a generally higher CaO content, with Wo > 50, ranging from salitic to ferro-salitic in composition, almost comparable to Cpx from alkaline rocks as described by Dal Negro *et al*. (1986).

6.4 Amphibole

Analogously to Cpx, Amph (Figure 12, Supplementary Table 8) is very different between the two series, the alkali content is a peculiar feature of the SU lithotypes. Amph from SS gabbros to syenites are mainly Mg-hornblende to actinolite in composition, followed by edenite and

Fe-edenite terms. In this series, actinolite is a reaction product upon primary Mg-hornblende and Cpx. On the other hand, Amph from SU gabbros to syenites range in composition between hastingsite, Mg-hastingsitie and Fe-pargasite. At comparable evolution degree (from gabbros to syenites), Amph composition show a remarkable differences between the two suites (Figure 12), SS Amph being higher in SiO_2, as well as lower in K_2O, Na_2O and Al_2O_3 contents with respect to Amph from SU series. In this latter, Na_2O and K_2O contents of Amph can reach up to 2.6 and 2.2 wt% respectively. Amph is absent in GU granites and syenogranites.

6.5 Biotite

Bt (Figure 12, Supplementary Table 9) occurs in SS, SU and GU lithotypes, testifying to the K-affinity of the PIC magmas. This phase is generally characterised by a high TiO_2 (0.9-6.1 wt%) content, except for granites and syenogranites of the GU suite ($TiO_2 \leq 3.3$ wt%), where Bt have also low Al_2O_3 and SiO_2 contents. At comparable SiO_2 content, Bt from SU monzo-gabbros are slightly enriched in Al_2O_3 with respect to those from SS monzo-gabbros (Figure 12). Discriminating feature is also the FeO content of Bt, separating the iron-rich GU Bt (FeO content up to 28.5 wt%) from the SS and SU ones. On the base of the FeO vs. SiO_2 content, SS Bt plot into two distinct fields: a first one is characterised by a lower Fe/Si ratio, and a second one, is described by an higher Fe content. Both of them are representative for Bt from gabbros to monzonites. SU Bt composition, whose iron content range from 10.0 to 11.4 wt%, fall within the second compositional spectrum (Figure 12).

6.6 Feldspars

Plag (Figure 11, Supplementary Table 10) is a common phase in all PIC rocks**,** often characterised by oscillatory zoning. In SS samples, Plag shows a compositional range from An_{81-56} in clinopyroxenites, An_{78-49} in monzo-gabbros and An_{50-43} in monzonites and An_7 in

the syenites. In the SU series, the average composition is about An_{48-29} in monzo-gabbros and monzonites. Orthoclase content in more differentiated lithotypes generally reaches values up to about 7%. K-feld (Figure 11, Supplementary Table 10), one of the main phases that characterise GU granites and syenogranites, has an almost negligible An content, as the orthoclase term increases up to 90%.

7. FC processes in the magma chamber

Petersen *et al*. (1980), Gasparotto and Simboli (1991), and Bonadiman *et al*. (1994) hypotesised the derivation of the intrusive rocks of the Dolomites from a monzo-gabbroic magma that mainly experienced fractional crystallization (FC) processes in an almost closed system, with subsequent generation of Cpx cumulates. PIC is the only multi-pulse intrusion of the Dolomitic Area in which more than one geochemical suite can be identified. Thus, major/trace element whole rock compositions, as well as major element mineral chemistry, were used for develop a mass balance calculation for modelling the main differentiation trends for the geochemical suites of the PIC (SS, GU and SU). This model is typically applied to effusive rocks. In closed system crystallization, assuming equilibrium conditions, also coarse grained intrusive rocks can be considered as magmatic liquids. According to the previous studies on this area (Petersen *et al*., 1980; Gasparotto and Simboli, 1991; Bonadiman *et al*., 1994) and on the petrographic features above mentioned, PIC rocks crystallization occurred in closed system-like conditions, making it possible to model their genesis via FC processes. This statement is also streghten by the comparison with the very similar composition of basaltic and hypoabyssal rocks outcropping in the area (Casetta *et al*., in prep.).

Aim of our model is to better constrain the genetic relationships between the various lithotypes (Figures 8, 10 and 13). In this respect, for example, the link between clinopyroxenites and gabbros or monzo-gabbros of both SS and SU series is not well defined.

Thus, two FC models were developed, for both SS and SU suites. FC calculations have been firstly attempted by using MELTS and Rhyolite-MELTS softwares: however, being the SS and SU magmatic suites enriched in Amph and Bt, no reliable results have been produced. In fact, application of such softwares to magmas fractionating under wet conditions is limited by the lack of appropriate thermodynamic models for hydrous mafic silicates, particularly Amph and Bt (Gualda *et al*., 2012). As a consequence, least squares mass balance calculations have been computed to simulate the FC processes that generated the PIC.

Monzo-gabbros were taken as starting material, while the final products were syenites. Accuracy on the major element mass balance model has been evaluated by means of the least squares error (r^2) between natural and calculated compositions. Trace element distribution in the calculated compositions was obtained using the partition coefficients (Kd, Supplementary Table 11) extracted by the GERM Database (earthref.org/KDD) and using the formulation of Shaw (1970) for Rayleigh fractionation, $C_L=C_0*F^{(D-1)}$, where: C_0 is the amount of the chosen element in the starting (natural) magma; C_L the amount of trace element calculated in the arrival magma; F the residual melt percentage; D the partition coefficients weighted for the percentage of fractionated minerals obtained by the mass balance calculation.

7.1 SS series

Monzo-gabbro FC43B was chosen as the nearest composition to a primary magma for this series (Supplementary Table 12) for its low SiO_2 and high mg#, Ni and Co amounts. The first step towards the more differentiated monzo-gabbro EM53 (Figure 13) accounts for the removal of 54% of a solid assemblage (SA1SS, $r^2 = 0.89$) made up of Ol (8.3%), Opx (5.1%), Cpx (21.3%), Plag (49.4%), Ap (2.3%), Mt (3.5%) and Bt (10.1%) with an overall gabbroic composition. The errors in the model for most of the trace elements are lower than 2% (Supplementary Table 12), except for Th and La, due to their low concentrations in the primary sample. The second stage from monzo-gabbro EM53 to monzonite EM85 is modelled

by removing 73% of a monzo-gabbroic assemblage (SA2SS, $r^2 = 0.68$), constituted by K-feld (6.2%), Amph (0.7%), Cpx (17.6%), Plag (52.2%), Ap (1.4%), Mt (5.3%) and Bt (16.6%), with errors on trace element contents lower than 14%. The last step from monzonite EM85 to syenite EM110 is derived by removal of 47% of a solid assemblage (SA3SS, $r^2 = 0.26$) of K-feld (16.3%), Amph (2.6%), Cpx (12.1%), Plag (41.9%), Ap (1.1%), Mt (4.1%), Bt (10.5%), Qz (10.6%), and Zirc (0.8%), with monzo-dioritic composition. Having Qz and Zirc the same effect on SiO_2 balance, Zirc modal fractionation (0.8%) was calculated based on Zr trace element modelling (Figure 10). Trace element composition of theoretical melt match very well with that of the natural magma, resulting in an error lower than 2% for all the elements except for Th (20%), due to its low concentration in the syenitic sample (9 ppm), and La (16%). Syenite is the result of 94% fractionation (Figures 8 and 10) corresponding to a solid residuum made up of gabbroic to monzo-gabbroic and monzo-dioritic lithotypes. The compositions calculated for the three solid assemblages (Figure 13) are similar to those of natural clinopyroxenitic and gabbroic to monzo-dioritic lithotypes found within the SS suite (Figure 8 and Figure 10), lending further support to the theoretical results. Moreover, several FC modelling attempts have been made to find a link between the SS suite and the GU granites and syenogranites. However, the mass balance calculation did not explain the genesis of the GU rocks via simple FC trends belonging to the SS suite.

7.2 SU series

The parent magma chosen as starting point for the modelling of the fractionation of this suite (Supplementary Table 13) was the nepheline normative monzo-gabbro EM10, characterised by high mg#, Ni and Co amounts (Figure 13). Monzo-gabbro EM10 can reach the monzonite EM7 by 63% fractionation of a solid assemblage (SA1SU, $r^2 = 0.98$), constituted by K-feld (4.7%), Amph (12.2%), Cpx (27.5%), Plag (35.9%), Ap (1.7%), Mt (11.0%) and Bt (7.0%), with gabbroic composition. The trace element (Rb, Ba, Th, Nb, La, Ce, Pb, Sr, Nd, Zr and Y)

distribution for this first step has an errors < 4%. The second stage from monzonite EM7 to syenite 11* can be modelled by removal of 44% of a monzo-dioritic assemblage (SA2SU, r^2 = 0.73) constituted by K-feld (32.1%), Amph (14.6%), Plag (44.2%), Ap (2.4%), Mt (4.1%) and Bt (2.6%). Trace element distribution errors are <1%, except for Pb and Th, whose errors are respectively 14% and 23%, being this latter due to the high amount of Th in the more differentiated rock. SU Syenite is the result of 79% fractionation (Figures 8 and 10) corresponding to a solid residuum made up of gabbroic to monzo-dioritic rocks (Figure 13), that fits well with the compositional spectrum of the similar lithotypes found within this portion of the complex, as highlighted also by the variation diagrams of Figure 8 and Figure 10.

8. Discussion

Whole rock major and trace element composition, as well as mineral chemistry and detailed field surveys, allowed to discriminate between the three magmatic suites that compose the PIC, after a re-evaluation of the petrogenetic subdivision proposed by Visonà (1997) and Marrocchino *et al*. (2002). All the three suites, namely SS, SU and GU are characterised marked Nb and Ti negative anomalies and a high positive Pb anomaly. Modal abundance of Bt, Amph and K-Feld, as well as late Mt crystallisation, leading to the lack of a Fe-Ti enrichment trend, support the by K-affinity of the magmas, typical of the shoshonitic series from active continental margins (Ewart, 1982). The progressive differentiation trend for both SS and SU series is marked by the appearance of a significant Eu negative anomaly, particularly in the more evolved syenites. On the other side, SU suite is characterised by lower K/Na ratios, as well as by higher LFSE and LREE content than SS and GU. Amph, absent in GU lithotypes, is markedly enriched in Al_2O_3, Na_2O and K_2O in the SU with respect to the SS suite, while iron-rich Bt is a peculiar feature of GU rocks. All these features lead to speculate

about the belonging of the SU suite to a magma pulse different to that of the SS one, likely related to spatial and/or temporal heterogeneities of their sources.

By means of this discrimination, mass balance calculations have been developed for both SS and SU series in order to model the FC processes in an almost closed system (Petersen *et al*., 1980; Gasparotto and Simboli, 1991; Bonadiman *et al*., 1994) responsible for the genesis of all PIC lithologies (Figures 8, 10 and 13). The calculated subtracted solids are quite similar in composition to the natural pyroxenitic and gabbroic to monzo-dioritic samples found within the complex, further supporting the accuracy of the model and suggesting that FC is the main differentiation process controlling the magmatic evolution. Still unsolved remains the relationship between the GU granites and syenogranites and the SS-SU suites, because of the independent geochemical behaviour of the formers. The alkali and silica content of the GU body, together with a marked Eu negative anomaly, may indicate a differentiation from a silica-oversaturated series, but the lack of any differentiated volcanic rock with similar features in the area surrounding PIC, as well as of any petrological relationships with the intrusive rocks of the complex, does not allow to put forward a robust cogenetic mechanism. Visonà (1997) proposed the existence of a calc-alkaline and/or oversaturated trend able to generate the granites and syenogranites. However, several attempts to reconstruct the geochemical features of the GU lithotypes via FC processes from the SS suite have been unsuccesfull. It has also to be noted that no rhyolitic products are found within the volcanics, thus, contrary of what occurs for the other two seires, there would not be a correspondence between GU and its effusive counterpart.

Together with the petrological distinction of the three suites, an accurate study of the field relationships of the intrusive portions, the volcanics, and the dike swarm outlines a detailed PIC temporal evolution (Figure 14) and defines the relationships with the effusive portions of the complex. According to our findings, PIC evolution is characterised by the emplacement of three magma batches with different petrological affinities in a relatively short time. The first

most voluminous SS pulse (3.1 km^3) was emplaced as what nowadays appears as an external ring. It was followed by the GU intrusion (1.1 km^3) in the central part of the complex, and then by the alkaline SU batch (0.3 km^3) in the eastern portion of the PIC. From field survey and volume estimates, it is evident that the SU series represents a minor contribution to the whole PIC: it likely constitutes the ultimate melt produced in the vanishing stage of the magmatic intrusion. During this last stage, several undersaturated dikes intruded the SS and GU lithotypes, indirectly constraining the temporal relationships between the three intrusive bodies by means of these cross-cutting relationships.

The presence of a fourth silica-oversaturated suite, identified by Visonà (1997) and Marrocchino *et al*. (2002) has been furthermore ruled out because of the paucity of oversaturated rocks scattered within the PIC, and of the overlap of their petrographic and geochemical features with the SS suite, in case of both whole rock and mineral chemistry. The origin of such rocks, whose Qz modal content lies between 4 and 15%, could be instead explained by the last stage of the FC processes for the SS suite (Figure 13). In this, the genesis of a SS syenite from a monzonitic material results by the removal of a monzo-dioritic solid assemblage with up to 11% Qz content (Supplementary Table 12), that is close to the natural monzo-diorites defined as "oversaturated" by Visonà (1997) and Marrocchino *et al*. (2002). This evidence suggests that the rare oversaturated rocks in PIC are fractionation products of the SS suite, making unlikely the existence of an independent oversaturated suite from which the GU lithotypes could have been derived.

The extended fieldwork along the contact between the PIC and the surrounding volcanites provided also important constraints about the so-called "Predazzo caldera" definition, introduced by Leonardi (1968), Castellarin *et al*. (1982), Doglioni (1984) and Gianolla *et al*. (2010) to take somehow into account the ring-shape of the PIC. In this context the transitional magmatic contact between the volcanics and the SS lithotypes (Figure 3) that has been found

on both the eastern and western part of the complex, as well as the lack of evolved caldera-filling materials, casts some doubts on the existence of a structure of this type.

9. Conclusions

Within the Dolomitic Area, the Predazzo magmatic complex is the most developed volcano-plutonic centre, being characterised by a 6 km^3 of volcanites surrounding 4.5 km^3 of intrusive rocks (PIC). This area is an entirely preserved magmatic complex, in which the relationships between the intrusion, the dike swarm, the host rocks and the volcanic products are exposed onto the surface, making it a perfect petrographic and petrological laboratory. Moreover, the PIC multi-pulse nature and high petrological variability point out its key role to constrain the main features of the Triassic magmatism in the Dolomites and in the whole Southern Alps domain. The combination of field, petrographic and petrological studies leads to the following considerations:

1. The K-affinity, the marked Nb and Ti negative anomalies, as well as the widespread occurrence of Amph and Bt in almost all PIC rocks, indicate a relationship with the shoshonitic series from active continental margins, suggesting the presence of a subduction setting in the Southern Alps domain, as already hypotised by Zanetti *et al.* (2013). However, the model of mixing between mantle-derived basic and crustal-derived acid magmas put forward by Sinigoi *et al*. (2011, 2016) for the Ivrea-Verbano magmatic complex and the related upper crustal section leaves the question still unanswered.

2. The PIC is a multi-pulse body, dominated by three main magmatic suites (SS, GU and SU), characterised by different HFSE and LREE contents, as well as by peculiar mineral assemblages, where Amph and Bt are a clear distinctive feature.

3. SS and SU differentiation trends explain the occurrence of cumulitic gabbros and pyroxenites within the complex, as well as the scattered presence of silica oversaturated lithotypes. The origin and nature of the GU suite remains uncertain, because of the absence of similar effusive products in the surrounding area and due to the impossibility to model the genesis of granites and syenogranites via simple FC process for the SS suite. Further studies are under way to investigate the relationships between such rocks, the PIC intrusive and effusive products.

4. The magmatic transitional contact identified between the PIC and the volcanites, as well as the lack of "caldera-filling"-like materials, lead to exclude the presence of a calderic collapse structure in the area, invoked by several authors to explain the ring-shape of the complex. By means of these considerations, the outcropping relationships between the PIC, the volcanic products, and the host rocks have to be considered in a different light. Such a finding will constitute a fundamental starting point to develope future accurate models on the magma chamber emplacement history and timing, in one of the few worldwide examples of an entirely preserved and "frozen" volcano-plutonic system.

Acknowledgements

Authors thank Raul Carampin (Department of Geosciences and CNR-IGG, University of Padova, Italy), for the electron microprobe (EMP) analyses. Authors would also acknowledge the Editor Robert J. Stern, whose suggestions significantly improved the manuscript, as well as Silvio Mollo and two anonymous Reviewers for their thoughtful comments.

References

Allahyari, K., Saccani, E., Rahimzadeh, B. and Zeda, O., 2014, Mineral chemistry and petrology of highly magnesian ultramafic cumulates from the Sarve-Abad (Sawlava)

ophiolites (Kurdistan, NW Iran): New evidence for boninitic magmatism in intra-oceanic fore-arc setting in the Neo-Tethys between Arabia and Iran: Journal of Asian Earth Sciences, v. 79, p. 312-328.

Armienti, P., Corazzato, C., Groppelli, G., Natoli, E. and Pasquarè, G., 2003, Geological and petrographical study of Montecampione Triassic subvolcanic bodies (Southern Alps, Italy): preliminary geodynamic results: Bollettino della Società Geologica Italiana, v. 2, p. 67-78.

Barth, S., Oberli, F., Meier, M., Blattner, P., Bargossi, G. M. and Di Battistini, G., 1993, The evolution of a calc-alkaline basic to silicic magma system: geochemical and Rb–Sr, Sm–Nd, and $^{18}O/^{16}O$ isotopic evidence from the Late Hercynian Atesina-Cima d'Asta volcanoplutonic complex, northern Italy: Geochimica et Cosmochimica Acta, v. 57, p. 4285-4300.

Beccaluva, L., Dal Piaz, G.V. and Macciota, G., 1984, Transitional to normal MORB affinities in ophiolitic metabasites from the Zermatt-Saas, Combin and Antrona units, Western Alps: implications for the paleogeographic evolution of the Western Tethyan Basin: Geologie en Mijnbouw, v. 63, p. 165-177.

Beccaluva, L., Coltorti, M., Saccani, E., Siena, F. and Zeda, O., 1996, Triassic Magmatism and Jurassic Ophiolites at the Margins of the Adria Plate, in Finetti I. R. ed., Crop Project: Deep Seismic Exploration of the Central Mediterranean and Italy: Elsevier, v. 28, p. 607-622.

Beccaluva, L., Bianchini, G., Bonadiman, C., Coltorti, M., Macciotta, G., Siena, F. and Vaccaro, C., 2005, Within-plate Cenozoic volcanism and lithospheric mantle evolution in the western-central Mediterranean area, in Finetti I. R. ed., Crop Project: Deep Seismic Exploration of the Central Mediterranean and Italy: Elsevier Special Volume, p. 641-664.

Bellieni, G., Fioretti, A. M., Marzoli, A. and Visonà, D., 2010, Permo–Paleogene magmatism in the eastern Alps: Rendiconti Lincei, v. 21, p. S51-S71.

Bernoulli, D. and Lemoine, M., 1980, Birth and Early Evolution of the Tethys: the Overall Situation: Mémoires du Bureau de recherches géologiques et minières, v. 115, p. 168-179.

Bertotti, G., Picotti, V., Bernoulli, D. and Castellarin, A., 1993, From rifting to drifting: tectonic evolution of the South-Alpine upper crust from the Triassic to the Early Cretaceous: Sedimentary Geology, v. 86, p. 53-76.

Bonadiman, C., Coltorti, M. and Siena, F., 1994, Petrogenesis and T-fO_2 estimates of Mt. Monzoni complex (Central Dolomites, Southern Alps): a Triassic shoshonitic intrusion in a trascurrent geodynamic setting: European Journal of Mineralogy, v. 6, p. 943-966.

Bonin, B., 1988, From orogenic to anorogenic environments: evidence from associated magmatic episodes: Schweizerische Mineralogische und Petrographische Mitteilungen, v. 68, p. 301-311.

Brack, P., Mundil, R., Oberli, F., Meier, M. and Rieber, H., 1996, Biostratigraphic and radiometric age data question the Milankovitch characteristics of the Latemar cycles (Southern Alps, Italy): Geology, v. 24, no. 4, p. 371-375.

Brack, P., Mundil, R., Oberli, F., Meier, M. and Rieber, H., 1997, Biostratigraphic and radiometric age data question the Milankovitch characteristics of the Latemar cycles (Southern Alps, Italy): Reply: Geology, v. 25, no. 5, p. 471-472.

Brack, P., Rieber, H., Nicora, A. and Mundil, R., 2005, The Global boundary Stratotype Section and Point (GSSP) of the Ladinian Stage (Middle Triassic) at Bagolino (Southern Alps, Northern Italy) and its implications for the Triassic time scale: Episodes, v. 28, no. 4, p. 233-244.

Brondi, A., Mittempergher, M., Panizza, M., Rossi, D., Sommavilla, E. and Vuillermin, F., 1977, Note Illustrative della Carta Geologica d'Italia, Foglio 028 La Marmolada: Servizio Geologico d'Italia, Roma, scale 1:50.000, 1 sheet.

Calanchi, N., Lucchini, F. and Rossi, P.L., 1977, M. Agnello: un apparato a condotto centrale delle Dolomiti: Mineralogica et Petrografica Acta, v. 21, p. 221-229.

Calanchi, N., Lucchini, F. and Rossi, P.L., 1978, The volcanic rocks from the Mount Agnello area (Fiemme Valley, Italy): a contribution to the knowledge of the Mid-Triassic magmatism of the Southern Alps: Tschermaks Mineralogische und Petrographische Mitteilungen, v. 25.

Cassinis, G., Cortesogno, L., Gaggero, L., Perotti, C. R. and Buzzi, L., 2008, Permian to Triassic geodynamic and magmatic evolution of the Brescian Prealps (eastern Lombardy, Italy): Bollettino della Società Geologica Italiana, v. 127, no. 3, p. 501-518.

Castellarin, A., Lucchini, F., Rossi, P.L., Simboli, G., Bosellini, A. and Sommavilla, E., 1980, Middle Triassic magmatism in Southern Alps II: A geodynamic model: Rivista Italiana di Paleontologia e Stratigrafia, v. 85, no. 3-4, p. 1111-1124.

Castellarin, A., Lucchini, F., Rossi, P.L., Sartori, L., Simboli, G. and Sommavilla, E., 1982, Note geologiche sulle intrusioni di Predazzo e dei M. Monzoni. Guida alla geologia del Sudalpino centro-orientale: Guide geologiche regionali S.G.I., p. 211-219.

Castellarin, A., Lucchini, F., Rossi, P.L., Selli, L. and Simboli, G., 1988, The Middle-Triassic magmatic-tectonic arc development in the Southern Alps: Tectonophysics, v. 146, p. 79-89.

Castellarin, A., 1983, Alpi Meridionali. Magmatismo e tettonica triassica: Memorie della Società Geologica Italiana, v. 24, p. 5-7.

Coltorti, M., Siena, F. and Visonà, D., 1996, Aspetti petrologici del magmatismo Triassico dell'area di Predazzo: Libro dei Riassunti, 78° Riunione Estiva S.G.I.

Cornelius, H.P. and Cornelius-Furlani, M., 1924, Zur Geologie der Tuffbildungen im Marmolatagebiet (Südtirol): Zentralblatt für Geologie und Paläontologie, v. 12, p. 366-373.

Dal Negro, A., Cundari, A., Piccirillo, E.M., Molin, G.M. and Uliana, D., 1986, Distinctive Crystal-chemistry and Site Configuration of the Clinopyroxene from Alkali Basaltic Rocks - the Nyambeni Clinopyroxene Suite, Kenya: Contributions to Mineralogy and Petrology, v. 92, p. 35-43.

Dal Piaz, G., 1993, Evolution of Austro-Alpine and Upper Penninic basement in the northwestern Alps from Varisican convergence to post-Varisican extension: Pre-Mesozoic geology in the Alps: Springer-Verlag, p. 327-344.

Dal Piaz, G., Bistacchi, A. and Massironi, M., 2003, Geological outline of the Alps: Episodes, v. 26, no. 3, p. 175-180.

Doglioni, C., 1984, Triassic diapiric structure in the central Dolomites (Northen Italy): Eclogae Geologicae Helvetiae, v. 77, p. 2.

Doglioni, C., 1987, Tectonics of the Dolomites (Southern Alps, Northern Italy): Journal of Structural Geology, v. 9, p. 181-193.

Doglioni, C. and Bosellini, A., 1987, Eoalpine and Mesoalpine tectonics in the Southern Alps: Geologische Rundschau, v. 76, no. 3, p. 735-754.

Doglioni, C. and Carminati, E., 2008, Structural styles and Dolomites field trip: Memorie Descrittive della Carta Geologica d'Italia, v. 82, p. 280.

Dymek, F.R., 1983, Titanium, aluminium and interlayercalation substitution in biotite from high-grade gneisses, West Greenland: American Mineralogist, v. 68, p. 880-899.

Ewart, A., 1982, The mineralogy and petrology of Tertiary-Recent orogenic volcanic rocks: with special reference to the andesitic-basaltic compositional range, in Thorp R.S. ed., Andesites: Orogenic Andesites and Related Rocks: John Wiley and Sons, New York, v. 724, p. 25-95.

Fondazione Dolomiti Dolomiten Dolomites Dolomitis UNESCO, Sito web ufficiale delle Dolomiti Patrimonio dell'Umanità UNESCO, www.dolomitiunesco.info

Frizzo, P., Peruzzo, L. and Dellantonio, E., 2010, The copper-wolfram deposit of Bedovina (Trento, Italy): Geo.Alp, v. 7, p. 55-70.

Gasparotto, G. and Simboli, G., 1991, Mineralogia, petrografia e schemi evolutivi delle magmatiti triassiche del complesso di Cima Pape (Dolomiti Orientali): Mineralogica et Petrografica Acta, v. 34, p. 205-234.

GERM, Partition Coefficient (Kd) Database, development and maintenance by the EarthRef.org Database Team, Data contribution by Roger Nielsen. Earthref.org/KDD.

Gianolla, P., Avanzini, M., Breda, A., Kustatscher, E., Preto, N., Roghi, G., Furin, S., Massari, F., Picotti, V. and Stefani, M., 2010, Dolomites, 7th International Triassic Field Workshop, Field trip to the World Heritage Site of the Tethyan Triassic. September 5-10 2010, Dolomites, Southern Alps, Italy. With the adesion of Fondazione Dolomiti-Dolomiten-Dolomites-Dolomitis Unesco.

Gianolla, P., 1992, Evoluzione mediotriassica del vulcanismo di Rio Freddo (Api Giulie, Italia): Memorie di Scienze Geologiche, v. 44, p. 193-209.

Gianolla, P., 2011, Il Libro di Roccia: Cierre Edizioni.

Gualda, G. A. R., Ghiorso, M. S., Lemons, R. V., Carley, T. L., 2012, Rhyolite-MELTS: a Modified Calibration of MELTS Optimized for Silica-rich, Fluid-bearing Magmatic Systems: Journal of Petrology, v. 53, p. 875-890.

Le Maitre, R. W., Bateman, P., Dudek, A., Keller, J., Lameyre Le Bas, M. J., Sabine, P. A., Schmid, R., Sorensen, H., Streckeisen, A., Woolley, A. R. and Zanettin, B., 1989, A classification of igneous rocks and glossary of terms: Blackwell, Oxford.

Leake, B. E., Arps, C. E. S. and Birch, W. D., 1997, Nomenclature of amphiboles: Report of the Subcommittee on Amphiboles of the International Mineralogica Association, Commission on New Minerals and Mineral Names: American Mineralogist, v. 82, p. 1019-1037.

Lemoine, M., Tricart, P. and Boillot, G., 1987, Ultramafic and gabbroic ocean floor of the Ligurian Tethys (Alps, Corsica, Appennines): In search of a genetic model: Geology, v. 15, p. 622-625.

Leonardi, P., 1968, Centro eruttivo di Predazzo: Le Dolomiti, Geologia dei monti tra Isarco e Piave, v. 52.

Lippolt, H. and Pidgeon, R., 1974, Isotopic mineral ages of a diorite from the Eisenkappel intrusion, Austria: Zeitschrift für Naturforschung, v. 29a.

Lucchini, F. and Morten, L., 1977, An example of flow differentiation: clinopyroxenite of the Predazzo igneous complex (north Italy): Lithos, v. 10, p. 39-47.

Lucchini, F., Rossi, P.L. and Simboli, G., 1982, Il magmatismo triassico dell'area di Predazzo (Alpi Meridionali, Italia). In A. Castellarin e G.B. Vai (Eds), Guida alla Geologia del Sudalpino centro-orientale: Guide Geologiche Regionali Società Geologica Italiana, p. 221-230.

Marocchi, M., Morelli, C., Mair, V., Klötzli, U. and Bargossi, G. M., 2008, Evolution of large silicic magma systems: new U–Pb zircon data on the NWPermian Athesian Volcanic Group (Southern Alps, Italy): Journal of Geology, v. 116, p. 480-498.

Marrocchino, E., Coltorti, M., Visonà, D. and Thirwall, M.F., 2002, Petrology of Predazzo magmatic complex (Trento, Italy): Geochimica et Cosmochimica Acta, v. 66, no. 15A, suppl. 1, p. A486-A486.

Marzari Pencati, G., 1820, Notizia sopra un granito in massa terziario sovrapposto al calcare secondario nel fiume Avisio: Supplemento al "Nuovo Osservatorio Veneziano", v. 118-127.

Menegazzo Vitturi, L., Visonà, D. and Zantedeschi, C., 1995, Amphibole composition in rocks from Predazzo volcano-plutonic complex (Southern Alps, Italy): Memorie di Scienze Geologiche, v. 47, p. 87-94.

Mietto, P., Manfrin, S., Preto, N., Rigo, M., Roghi, G., Furin, S., Gianolla, P., Posenato, R., Muttoni, G., Nicora, A., Buratti, N., Cirilli, S., Spötl, C., Ramezani, J. and Bowring, S.A., 2012, The Global Boundary Stratotype Section and Point (GSSP) of the Carnian Stage (Late Triassic) at Prati di Stuores/ Stuores Wiesen Section (Southern Alps, NE Italy): Episodes, v. 35, no. 3, p. 414-430.

Mundil, R., Brack, P. and Laurenzi, M. A., 1996, High resolution U/ Pb single zircon age determinations: new constrints on the timing of Middle Triassic magmatism in the Southern Alps: Libro dei Riassunti, 78° Riunione estiva S.G.I.

Mundil, R., Brack, P., Meier, M., Rieber, H. and Oberli, F., 1996, High resolution U-Pb dating of middle Triassic volcaniclastics: time-scale calibration and verification of tuning parameters for carbonate sedimentation: Earth and Planetary Science Letters, v. 141, p. 137-151.

Nimis, P., Omenetto, P., Giunti, I., Artioli, G. and Angelini, I., 2012, Lead isotope systematics in hydrothermal sulphide deposits from the central-eastern Southalpine (northern Italy): European Journal of Mineralogy, v. 24, p. 23-37.

Paganelli, L. and Tiburtini, R., 1964, The Predazzo granite, North Italy: Mineralogica et Petrographica Acta, v. 10, p. 57-79.

Pearce, J. A., 1982, Trace elements characteristics of lavas from destructive plate boundaries, in Thorpe E. S. ed., Andesites: New York, John Wiley and Sons, p. 525-548.

Petersen, J. S., Morten, L., Simboli, G. and Lucchini, F., 1980, REE abundances in the Predazzo-Monzoni intrusive complex, Dolomites, North Italy: Rivista Italiana di Paleontologia e Stratigrafia, v. 85, p. 1065-1080.

Piccardo, G. B., Rampone, E., Vannucci, R. and Cimmino, F., 1994, Upper mantle evolution of ophiolitic peridotites from the Northern Apennine: Petrological constraints to the geodynamic processes: Memorie della Società Geologica Italiana, v. 8, p. 137-148.

Pisa, G., Castellarin, A., Lucchini, F., Rossi, P.L., Simboli, G., Bosellini, A. and Sommavilla, E., 1979, Middle Triassic magmatism in Southern Alps. I: a review of general data in the Dolomites: Rivista Italiana di Paleontologia e Stratigrafia, v. 85, no. 3-4, p. 1093-1110.

Quick, J. E., Sinigoi, S., Snoke, A.W., Kalakay, T. J., Mayer, A. and Peressini, G., 2003, Geologic map of the Southern Ivrea-Verbano Zone, Northwestern Italy: U.S. Geological Survey.

Quick, J. E., Sinigoi, S., Peressini, G., Demarchi, G., Wooden, J. L. and Sbisà, A., 2009, Magmatic plumbing of a large Permian caldera exposed to a depth of 25 km: Geology, v. 37, p. 603-606.

Rampone, E. and Piccardo, G.B., 2000, The ophiolite-oceanic lithosphere analogue: new insights from the Northern Apennines (Italy), In Dilek J., Moores E., Elthon D. and Nicolas A. eds., Ophiolites and Oceanic Crust: New Insights from Field Studies and Ocean Drilling Program: Geological Society of America Memoir, Special Paper, v. 349, p. 21-34.

Rossi, P.L., Viel, G. and Simboli, G., 1976, Significato paleogeografico e magmatico-tettonico della serie vulcano-clastica ladinica superiore nell'area del Monte Civetta: Bollettino della Società Geologica Italiana, v. 95, p. 433-458.

Salomon, W., 1895, Geologische und palaontologische Studien fiber die Marmolata: Palaeontographica, v. 42, no. 1, p. 210.

Scandone, P., 1975, Triassic seaways and the Jurassic Thethis Ocean in the central Mediterranean area: Nature, v. 256, p. 5513.

Schmid, S. M., Bernoulli, D., Fügenschuh, B., Matenco, L., Schefer, S., Schuster, R., Tischler, M. and Ustaszewski, K., 2008, The Alpine-Carpathian-Dinaridic orogenic system: correlation and evolution of tectonic units: Swiss Journal of Geosciences, v. 101, no. 1, p. 139-183.

Schmid, M. S., Bernoulli, D., Fügenschuh, B., Georgiev, N., Kounov, A., Matenco, L., Oberhansli, R., Pleuger, J., Schefer, S., Ustaszewski, K. and Van Hinsbergen, D., 2016, Tectonic units of the Alpine collision zone between Eastern Alps and Western Turkey: Unpublished map.

Sinigoi, S., Quick, J. E., Demarchi, G. and Klotzli, U., 2011, The role of crustal fertility in the generation of large silicic magmatic systems triggered by intrusion of mantle magma in the deep crust: Contributions to Mineralogy and Petrology, v. 162, p. 691-707.

Shaw D. M., 1970. Trace-element fractionation during anataxis: Geochimica et Cosmochimica Acta, v. 34, p. 237-243.

Sinigoi, S., Quick, J. E., Demarchi, G. and Klotzli, U., 2016, Production of hybrid granitic magma at the advancing front of basaltic underplating: Inferences from the Sesia Magmatic System (south - western Alps, Italy): Lithos, v. 252-253, p. 109-122.

Sloman, L. E., 1989, Triassic shoshonites from the dolomites, northern Italy: Alkaline arc rocks in a strike-slip setting: Journal of Geophysical Research: Solid Earth, v. 94, no. B4, p. 4655-4666.

Stahle, V., Frenzel, G., Hess, J. C., Saupé, F., Schmidt, S. T. and Schneider, W., 2001, Permian metabasalt and Triassic alkaline dykes in the northern Ivrea zone: clues to the post-Variscan geodynamic evolution of the Southern Alps: Schweizerische Mineralogische und Petrographische Mitteilungen, v. 81, no. 1, p. 1-21.

Stampfli, G. M. and Borel, G. D., 2002, A plate tectonic model for the Paleozoic and Mesozoic constrained by dynamic plate boundaries and restored synthetic oceanic isochrones: Earth and Planetary Science Letters, v. 196, no. 1, p. 17-33.

Stampfli, G. M. and Borel, G. D., 2004, The TRANSMED transects in space and time: constraints on the paleotectonic evolution of the Mediterranean domain, in The TRANSMED Atlas: The Mediterranean region from crust to mantle, p. 53-80.

Stampfli, G. M., Borel, G. D., Marchant, R. and Mosar, J. (2002): Western Alps geological constraints on western Tethyan reconstructions: Journal of the Virtual Explorer, v. 8, p. 77.

Sun, S. and McDonough, W.F., 1989, Chemical and isotopic systematics of oceanic basalts: implication for mantle and processes, in Saunders A.D. and Norry M.J. eds., Magmatism in the Ocean Basins: Geological Society, Special Publications, v. 42, p. 313-345.

Traill, R. J. and Lachance, G.R., 1966, A practical solution to the matrix problem in X-ray analysis. II. Application to a multi-component alloy system: Canadian Spectroscopy, v. 11, p. 63-71.

Vardabasso, S., 1929, Rapporti tra attività magmatica e vicende tettoniche nella provincia petrografica di Predazzo: Studi Trentini di Scienze Naturali, v. 11.

Vardabasso, S., 1930, Carta geologica del territorio eruttivo di Predazzo e Monzoni: Ufficio Idrografico del Magistrato alle Acque di Venezia, PD, scale 1:25000, 2 sheet.

Visonà, D., 1997, The Predazzo multipulse intrusive body (Western Dolomites, Italy). Field and mineralogical studies: Memorie di Scienze Geologiche, v. 49, p. 117-125.

Zanetti, A., Mazzucchelli, M., Sinigoi, S., Giovanardi, T., Peressini, G. and Fanning, M., 2013, SHRIMP U–Pb Zircon Triassic intrusion age of the Finero mafic complex (Ivrea–Verbano zone, Western Alps) and its geodynamic implications: Journal of Petrology, v. 54, no. 11, p. 2235-2265.

Ziegler, P. A. and Stampfli, G. M., 2001, Late Palaeozoic-Early Mesozoic plate boundary reorganization: collapse of the Variscan orogen and opening of Neotethys: Natura Bresciana, v. 25, p. 17-34.

Figure Captions

Figure 1 (colour online).

(a) Distribution of the Triassic magmatism in the Alps. The tectonic units of the eastern portion of the Alps are partly modified from Dal Piaz *et al*. (2003) and Schmid *et al*. (2016). LO: Ligurian Ophiolites; AM: deformed Adriatic margin; AD: Adriatic Microplate; SA: Southern Alps; DI: Dinarides; SM: Southern margin of Meliata; HB: Eoalpine High-Pressure Belt; TW: Tauern tectonic Window; EW: Engadine tectonic Window; OTW: Ossola-Tessin tectonic Window; EA: Eastern Austroalpine; H: Helvetic domain; M: Molasse foredeep. In the Southern Alps domain the Triassic igneous bodies (see also Castellarin *et al*., 1988) are evidenced: (1) Brescian Alps (Cassinis *et al*., 2008); (2) Alto Vicentino (Bellieni *et al*., 2010); (3) Dolomitic Area; (4) Carnia region (Gianolla *et al*., 1992; Brack *et al*., 2005); (5) Karavanke, Austria (Lippolt and Pidgeon, 1976; Bellieni *et al*., 2010). (b) Distribution of

intrusives (Predazzo Intrusive Complex = PIC, Mt. Monzoni and Cima Pape), volcanics, and dike swarms in the Dolomitic Area.

Figure 2 (colour online).

Simplified geological map and cross-section of the Predazzo Intrusive Complex.

Figure 3 (colour online).

Photomicrographs and field reconstruction (modified from Google Earth) reporting the grain size gradual transition from volcanic to intrusive rocks of the Shoshonitic Silica Saturated Unit at the eastern edge of Predazzo Intrusive Complex. (a) Porphiritic trachyandesite (1850 m a.s.l., M.te Mulat) comprising large plagioclase and clinopyroxene phenocrysts embedded in a microcrystalline plagioclase + clinopyroxene + oxide groundmass (transmitted plane-polarized light). (b) Hypabissal monzonite (1900 m a.s.l., M.te Mulat) characterised by large plagioclase over a microcrystalline assemblage of quartz + K-feldspar + biotite + plagioclase + clinopyroxene + amphibole (transmitted plane-polarized light). (c, d) Holocrystalline monzo-diorite (1900 m a.s.l., M.te Mulat) composed of plagioclase + clinopyroxene + biotite + amphibole + oxides (c: transmitted plane-polarized light; d: cross polarized light).

Figure 4.

QAPF diagram showing the distribution of rocks from the Predazzo Intrusive Complex.

Figure 5.

Total alkali vs. silica (TAS) classification diagram (Le Maitre *et al*., 1989) showing whole rock compositions from the Predazzo Intrusive Complex.

Figure 6.

K_2O vs. SiO_2 classification diagram (Ewart, 1982) showing whole rock compositions from the Predazzo Intrusive Complex.

Figure 7.

K_2O vs. Na_2O classification diagram showing whole rock compositions from the Predazzo Intrusive Complex.

Figure 8.

(a, b) CaO and (c, d) FeO vs. SiO_2 variation diagrams showing whole rock compositions from the Predazzo Intrusive Complex. (a, c) Shoshonitic Silica Saturated, Granitic Unit, and Shoshonitic Silica Undersaturated suites are plotted together with the composition of the solid assemblages derived by the FC modelling. SA1SS = Gabbroic Solid Assemblage 1 with SS affinity; SA2SS = Monzo-gabbroic Solid Assemblage 2 with SS affinity; SA3SS = Monzo-dioritic Solid Assemblage 3 with SS affinity; SA1SU = Gabbroic Solid Assemblage 1 with SU affinity; SA2SU = Monzo-dioritic Solid Assemblage 2 with SU affinity. (b, d) FC vectors derived for the SS and SU suites using as starting compositions the monzo-gabbros (samples FC43B and EM10 respectively). The final compositions are syenites (samples EM110 and 11* respectively). For each step is also reported the relative percentage of the fractionating mineral phases, traslating to the compositions of the subtracted solid assemblages. Ol = olivine; Opx = orthopyroxene; Cpx = clinopyroxene; Plag = plagioclase; Ap = apatite; Mt = magnetite; Bt = biotite; K-Feld = K-feldspar; Amph = amphibole; Qz = quartz; Zirc = zircon.

Figure 9.

N-MORB-normalised trace element and REE patterns for representative Predazzo Intrusive Complex (a, b) pyroxenites, (c, d) GU, (e, f) SS and (g, h) SU rocks. Normalising values from Sun and McDonough (1989).

Figure 10.

(a, c) Rb and (b, d) Zr vs. SiO_2 variation diagrams of rocks from the Predazzo Intrusive Complex. (a, c) Shoshonitic Silica Saturated, Granitic Unit and Shoshonitic Silica Undersaturated suites. (b, d) FC vectors derived for the SS and SU suites using as starting compositions the monzo-gabbros (samples FC43B and EM10 respectively). The final compositions are syenites (samples EM110 and 11* respectively). For each step is also reported the relative percentage of the fractionating mineral phases, traslating to the compositions of the subtracted solid assemblages. Ol = olivine; Opx = orthopyroxene; Cpx = clinopyroxene; Plag = plagioclase; Ap = apatite; Mt = magnetite; Bt = biotite; K-Feld = K-feldspar; Amph = amphibole; Qz = quartz; Zirc = zircon.

Figure 11.

(a) Pyroxene, (b) magnetite, and (c) feldspar classification diagrams.

Figure 12.

(a) Al_2O_3 vs. SiO_2 and (b) K_2O vs. SiO_2 diagrams for Shoshonitic Silica Saturated and Shoshonitic Silica Undersaturated amphiboles. (c) Al_2O_3 vs. SiO_2 and (d) FeO vs. SiO_2 diagrams for Shoshonitic Silica Saturated, Shoshonitic Silica Undersaturated and Granitic Unit biotites. Field labels are based on amphibole and biotite classification from Leake *et al.* (1997) and Dymek (1983), respectively.

Figure 13.

Total alkali vs. silica (TAS) classification diagram (Le Maitre *et al.*, 1989) illustrating the fractional crystallization modelling of selected rock samples from the Predazzo Intrusive Complex, as well as the compositions of the cumulate assemblages calculated from the model

compared to the natural cumulate lithotypes. SA1SS = Gabbroic Solid Assemblage 1 with SS affinity; SA2SS = Monzo-gabbroic Solid Assemblage 2 with SS affinity; SA3SS = Monzo-dioritic Solid Assemblage 3 with SS affinity; SA1SU = Gabbroic Solid Assemblage 1 with SU affinity; SA2SU = Monzo-dioritic Solid Assemblage 2 with SU affinity.

Figure 14.

Interpretative sketch of the evolutionary sequence of rocks from the Predazzo Intrusive Complex. The first pulse at t1 (a) is characterised by Shoshonitic Silica Saturated affinity; the second pulse at t2 (b) is represented by the intrusion of the Granitic Unit granites and syenogranites; the final pulse at t3 (c), outcropping in the eastern part of the complex, is constituted by Shoshonitic Silica Undersaturated terms. t2 (237 Ma) is from Mundil *et al*. (1996). The cumulitic gabbros and pyroxenites are also shown at the border of the Shoshonitic Silica Saturated intrusion.

Petrological evolution of the Middle Triassic Predazzo Intrusive Complex, Italian Alps

Federico Casetta*

Department of Physics and Earth Sciences, University of Ferrara

Via Saragat 1, 44121 Ferrara, Italy

Massimo Coltorti

Department of Physics and Earth Sciences, University of Ferrara

Via Saragat 1, 44121 Ferrara, Italy

Elena Marrocchino

Department of Physics and Earth Sciences, University of Ferrara

Via Saragat 1, 44121 Ferrara, Italy

* Corresponding author.

Phone +39 0532 974721.

E-mail: cstfrc@unife.it

Petrological evolution of the Middle Triassic Predazzo Intrusive Complex, Italian Alps

Abstract

The Predazzo Intrusive Complex (PIC), a Ladinian plutonic body located in the Southern Alps (NE Italy), is made up of a 4.5 km^3 gabbroic to syenitic and syenogranitic intrusion, basaltic to latitic volcanic products (about 6 km^3 in volume) and by an extended dike swarm intruding both intrusive and volcanic rocks. An extensive field survey of the complex, followed by detailed petrographic and geochemical analyses, allowed the identification of three different magmatic units: a Shoshonitic Silica Saturated Unit (SS), 3.1 km^3 in volume, a Shoshonitic Silica Undersaturated Unit (SU), 0.3 km^3 in volume, and a Granitic Unit (GU), 1.1 km^3 in volume. K-affinity, marked Nb and Ti negative anomalies and a strong Pb enrichment are distinctive markers for all PIC lithotypes. A general HFSE (Th, U, Pb), LREE (La, Ce, Pr, Nd) and Na enrichment characterises the SU suite with respect to the SS series. Mass balance calculations, based on major and trace element whole rock and mineral compositions, have been used to simulate the fractionation process of SS and SU suites, showing (i) the complexity of the evolutionary stages of the PIC and (ii) the analogy between the calculated subtracted solid assemblages and the natural cumulitic lithotypes outcropping in the area. The field relationships between the various portions of the intrusive complex, the volcanic products and the dike swarm define the temporal evolution of the PIC, in which the SS magma batch was followed by the GU and later on by the SU intrusion. The presence, in both eastern and western portions of the complex, of a transitional magmatic contact between the intrusive rocks of the SS suite and the volcanics is not in favour of the hypothesis of a caldera collapse to explain the ring-like shape of the PIC.

Keywords

Predazzo Intrusive Complex; Caldera collapse; Triassic shoshonitic magmatism; Multi-pulse intrusion

1. Introduction

The Predazzo Intrusive Complex (PIC), together with Mt. Monzoni and Cima Pape areas, represents one of the main intrusive expressions of the Triassic magmatism within the Dolomites (Southern Alps domain, Italy), which is strongly dominated by the presence of volcanics and dikes throughout all the Schlern/Seiser Alm (NW) and the Cadore (NE) regions (Figure 1). This ring-shaped intrusive body is surrounded by a large amount of volcanic products, covering an area of nearly 25 km^2. PIC is a Late Ladinian complex (237.3 ± 1.0 Ma) intruded in Permian to Middle Triassic volcanic and sedimentary formations (Mundil *et al*., 1996; Brack *et al*., 1996, 1997, 2005; Mietto *et al*., 2012). The occurrence of a well-defined metamorphic contact and the relationships between the igneous rocks and the surrounding limestones attracted the interest of scientists since the XIX century, making the Predazzo - Mt. Monzoni volcano-plutonic area one of the main subjects of the debate on the origin of igneous rocks, also known as the neptunistic - plutonistic controversy (Fondazione Dolomiti UNESCO). Mt. Monzoni intrusion played also a central role for the development of the petrography, giving the name to the monzonitic rocks themselves. Many petrological studies were carried out in order to explain the orogenic character of these complexes and the intrusion sequence: the clearly shoshonitic affinity of the Middle Triassic magmatism, both in effusive, subvolcanic and intrusive terms, is in fact concomitant with the general anorogenic tectonic regime of the region during the Ladinian (Rossi *et al*., 1976; Castellarin, 1983; Bonin, 1988; Zanetti *et al*., 2013). The origin of this magmatic event was afterwards linked to an extensional tectonic regime, dominated by vertical differential movements and subsidence (Gianolla *et al*., 2010), which were able to generate shoshonitic magmas by decompression melting of a subduction-related, previously metasomatized mantle source (Sloman, 1989;

Bonadiman *et al*., 1994). After having been at the heart of the petrographic debate for decades, the study of PIC was abandoned, despite its key role in the interpretation of the Southern Alps Triassic magmatism. This volcano-plutonic complex has been in fact almost completely preserved, in both its intrusive and volcanic portions, from the action of the alpine tectonic event, resulting one of the rare places worldwide where the relationship between an ancient magma chamber, its volcanic products and the host rocks could be observed. PIC, unlike Mt. Monzoni and Cima Pape, is characterised by the presence of multiple shoshonitic silica saturated, oversaturated and undersaturated plutons, whose genetic relationships gave rise to various debates (Sloman, 1989; Bonadiman *et al*., 1994; Menegazzo Vitturi *et al*., 1995; Visonà, 1997; Marrocchino *et al*., 2002). The present study is aiming at a complete geological and petrological reconstruction of the complex, which can also foster a deeper understanding of the Triassic magmatism in the Southern Alps. Detailed field survey and sampling, togheter with an accurate petrological investigations (whole rock and mineral major/trace element analyses) on more than 180 samples, were carried out in order to define i) the differentiation processes occurring within the feeding system, ii) the relationships between the various intrusive bodies and iii) their petrological signature.

2. Geological setting and geodynamic

At the end of the Hercynian orogenesis, the Dolomitic Area was initially involved in a ductile tectonic regime, characterised by greenschist facies metamorphism, and then uplifted and eroded (Gianolla *et al*., 2010). During this period, the Southern Alps were involved in a continental rifting phase (Doglioni and Bosellini, 1987; Bertotti *et al*., 1993) with a gradual, asymmetric, passive extension of the European and African continental lithosphere (Lemoine *et al*., 1987; Piccardo *et al*., 1994). Permian intrusions, such as the Ivrea-Verbano Mafic Complex (Western Alps, Italy, Quick *et al*., 2003; Sinigoi *et al*., 2011, 2016), Mt. Cervino (Western Alps, Italy) and Mt. Collon (Western Alps, Switzerland), are the result of extension-

related mantle partial melting as consequence of the thinning of the continental lithosphere displaced along a master detachment fault at the northwestern margin of the future Adria plate (Dal Piaz, 1993). This event was characterised by the activation of a brittle/ductile intra-lithospheric shear zone, thermal perturbations connected with mantle-derived basic intrusions in the lower crust, and hybrid anatectic to mafic-derived acidic magmatism in the upper crust (Barth *et al*., 1993; Quick *et al*., 2003; Marocchi *et al*., 2008; Sinigoi *et al*., 2016). Passive mechanisms for the extension of the subcontinental lithospheric mantle have been also proposed for the onset of the Ligure-Piemontese oceanic basin (Beccaluva *et al*., 1984), associated with precursory Permian magmatic episodes (Rampone and Piccardo, 2000). The mature stage of the continental rifting is marked by Middle-Late Triassic widespread deposition of shallow-water carbonates and by the development of narrow seaways (Scandone, 1975; Gianolla, 2011). Several Triassic magmatic occurrences (Figure 1), mostly intercalated within the sedimentary sequence, are reported from the western margins of the Adria plate (Sicily, Calabria, Sardinia, Tuscany and Liguria) and the eastern Dynarides-Hellenides orogenic belts, these latter being characterised by calc-alkaline to shoshonitic affinity (Beccaluva *et al*., 2005).

The Triassic magmatism (Table 1) is also widely represented among the entire Southern Alps, from the Brescian Alps (Cassinis *et al*., 2008) and the Alto Vicentino Area (Bellieni *et al*., 2010), towards the Dolomitic Area, the Carnia region (Gianolla, 1992; Brack *et al*., 2005) and the Karavanke ragion in Austria (Lippolt and Pidgeon, 1976; Bellieni *et al*., 2010).

The Dolomitic Area represents a large part of the Southern Alps, and was characterised, during the Ladinian, by the presence of isolated carbonatic platforms, elevated over deep marine basins, formed as a conseguence of the extensional tectonic regime. Evidence for volcanic activity during the Ladinian and Carnian may be found, as above mentioned, throughout the Southern Alps, even if its main expressions developed in the western Dolomites (Salomon, 1895; Cornelius and Cornelius-Furlani, 1924; Vardabasso, 1929, 1930;

Leonardi, 1968; Brondi *et al*., 1977; Calanchi *et al*., 1977, 1978; Pisa *et al*., 1979; Castellarin *et al*., 1980; Lucchini *et al*., 1982; Sloman, 1989; Gianolla *et al*., 2010), where a thick sequence of calc-alkaline to shoshonitic subaerial lavas, pillow lavas, lava breccias, hyaloclastites and volcanoclastic sandstones, with associated intrusive bodies (PIC, Cima Pape and Mt. Monzoni) and dike swarms can be found (Bonadiman *et al*., 1994; Beccaluva *et al*., 1996; Coltorti *et al*., 1996; Gianolla, 2011). The orogenic affinity of this magmatism, contrasting with the geodynamic setting of the entire Southern Alps domain during the Triassic, has been the matter of a longstanding debate (Table 1). Bernoulli and Lemoine (1980) considered this area as part of an aborted rift in a passive margin contest, while Castellarin *et al*. (1980) placed it in a compressive margin, at the northwetsern limb of the Paleo-Tethys. More recent studies invoked also the involvement of an "active" mantle upwelling (Stähle *et al*., 2001), as well as a transition to back-arc conditions started in Carboniferous-Permian times, triggered by the northward subduction of the Paleotethys remnants (Ziegler and Stampfli, 2001; Stampfli and Borel, 2002; Stampfli *et al*., 2002; Armienti *et al*., 2003; Cassinis *et al*., 2008; Schmid *et al*., 2008). In order to explain the discrepancy between the orogenic affinity of the magmas and the "anorogenic" geodynamic setting, Bonadiman *et al*. (1994) proposed a partial melting of a mantle source previously metasomatised by subduction-related components during the Hercynian orogenic cycle. On the other hand, crustal and mantle rocks of the Ivrea-Verbano Zone recorded a subduction-related signature for the Middle Triassic magmatic event (Zanetti *et al*., 2013), where the closure of the Paleotethys activated the rotation and the strike-slip displacement of several micro-plates, generating local transtensional dynamics (Doglioni, 1984, 1987; Stampfli and Borel, 2002, 2004). This type of tectonic kinematics caused the development of block-faulting, flower-type and en-enchelon structures, and the development of the magmatism along a general N70E axis. This geodynamic setting may account for the discontinuous emplacement of deep-seated to shallow levels magmas through lithospheric transtensional

faults. These contemporary evidences of extensional and compressive dynamics have therefore led to put forward the existence of a back-arc basin in the Southern Alps, linked to the Paleotethys subduction or due to the collision of Apulia and Adria plates (Stampfli and Borel, 2002, 2004; Zanetti *et al*., 2013). This setting would be also in agreement with the rapid subsidence recorded for the Dolomitic Area (Doglioni, 2007) and the orogenic affinity of the magmas (Table 1).

The first petrographic studies on PIC rocks are dated back to about 200 years ago (Marzari Pencati, 1820), when the relationship between the Triassic magmatic intrusion and the surrounding limestone was documented for the first time. Since then, several authors (Vardabasso, 1930; Paganelli and Tiburtini, 1964; Petersen *et al*., 1980; Castellarin *et al*., 1982; Lucchini *et al*., 1982; Menegazzo Vitturi *et al*., 1995; Coltorti *et al*., 1996; Visonà, 1997) identified the multi-pulse nature of the ring-like shaped intrusion and the high variability of lithotypes of which it is composed. The large compositional spectrum of PIC rocks, resulting in the presence of both quartz- and nepheline-normative lithotypes, created a large number of debates on the petrogenesis of the magmatic complex (Vardabasso, 1930; Lucchini *et al*., 1982; Menegazzo Vitturi *et al*., 1995; Coltorti *et al*., 1996; Visonà, 1997). Commonly accepted is the monzo-gabbroic (i.e. trachybasaltic) nature of the PIC parental magmas and their orogenic affinity (Bonadiman *et al*., 1994; Marrocchino *et al*., 2002). However, the presence of various differentiates (quartz- and nepheline-bearing syenites, and oversaturated granites/syenogranites), as well as of clinopyroxenitic bodies at the intrusion borders makes the genetic processes of each portion of the complex extremely controversial. As a consequence, PIC petrographic and geochemical features have been interpreted either as a result of flow differentiation or mingling processes (Lucchini and Morten, 1977; Visonà, 1997), giving rise to a large number of uncertainties on the nature of one of the longer-term studied intrusive bodies of the Southern Alps.

3. Materials and methods

Whole rock major and trace element analyses of PIC samples have been carried out at the Department of Physics and Earth Sciences (University of Ferrara, Italy).

XRF analyses on a first batch of samples was performed by Marrocchino *et al*. (2002). Further on PIC sampling was extended and a second analytical stage for major and trace elements, using a wavelength - dispersive ARL Advant'XP X-Ray fluorescence spectrometer was carried out. The full matrix correction procedure and the intensities were elaborated following Traill and Lachance (1966). Accuracy and precision are better than 2-5% for major elements and 5-10% for trace elements. The detection limit is 0.01% and 1-3 ppm for most of the major and trace element concentrations, respectively (Allahyari *et al*., 2014). Both batches of samples were compared with the same internal standards to assure the homogeneity and coherence of the results. Moreover, a set of representative samples from the first group was re-analyzed. Results indicate that differences between the two datasets are within analytical error.

Rare earth elements (REE) and Y were analysed using an inductively coupled plasma mass spectrometer (ICP-MS) VG Plasma Quad2 Plus with precision and accuracy better than 10% for all elements, well above the detection limit (see also Allahyari *et al*., 2014).

Mineral compositions were analysed at the IGG-CNR hosted at Department of Geosciences (University of Padova, Italy) using a Cameca-Camebax electron microprobe (EMP) system, operating at an accelerating voltage of 15 kV and specimen current of 15 nA with a counting time of 10s for peak and 20s for background. Natural and synthetic compounds and oxides were used as standards. Accuracy and precision were within 2% for major and 5 % for minor elements.

4. Field characters and volume estimation

The main part of PIC is made up of a monzo-gabbroic to syenitic external ring-shaped body (with minor gabbros and clinopyroxenites) and by subordinated more differentiated intrusions, outcropping in the central (granites to syenogranites) and in the eastern part of the ancient magma chamber (Figure 2). A huge amount of volcanic and volcanoclastic products, ranging in composition from basalts to latites, surrounds the intrusive portion, outcropping mainly in the northern and western sectors of the magmatic complex. A dike swarm, basaltic to trachytic in composition, variable in width from tens of centimetres to few metres and with two prevalent strike directions (NNW-SSE and E-W), cut sedimentary, volcanic and intrusive rocks. The entire complex is nowadays largely covered by vegetation, whereas during the XX century it was famous for the syenogranite quarries, as well as for the Bedovina Mine, a W, Mo, Sn, Bi, Cu, Pb, Zn, Ag, Te, Co and Ni mineralization (Frizzo *et al*., 2010) lying at the northeastern contact between PIC and the volcanic products (Figure 2).

A detailed geological survey together with an extensive sampling of the Predazzo area allowed the reconstruction of the outcrop geometries for the entire PIC, as well as the mapping of the volcanic and volcanoclastic deposits. As shown further on, this field work defined the existence of three different magmatic units. In an overall view, both intrusive and volcanic portions are exposed to the surface, making possible to study the relationship between the ancient magma chamber and the overlying extrusive rocks, mainly in the central and in the eastern parts (Figure 2). Here, in fact, the intrusion outcrops almost continuously over about 1000 m of vertical gap, preserving both its inner portions and its upper edges, where the contact with the corresponding volcanic products and the host rocks is clearly delineated. At the bottom of the PIC (about 900 m a.s.l.) the contact between the various lithotypes is well preserved: the relationships between the portions of the intrusion, as well as between them and the widespread dike swarm, contributed also to constrain the intrusive sequence that formed the magmatic complex. In addition, these intrusions show a gradual transition to the volcanic rocks over a distance of hundred metres, marked by the presence of

relatively fine-grained monzo-gabbroic to monzonitic lithotypes, with a hypabyssal texture (Figure 3). These rocks outcrop almost symmetrically above the Bedovina Mine (Mt. Mulat) on the eastern side of the complex and at the Malga Gardoné on its western side, suggesting the presence of a transitional, magmatic contact between the intrusion and the volcanics, i.e. the absence of a tectonic contact between these two lithotypes. The widespread vegetation covering the whole complex, together with the length of such transition, makes not possible to show these contacts.

For decades one of the most debated topics linked to the PIC has been the relationship between the intrusive and the volcanic portions. Due to its ring-like shape the historical definition of "Predazzo caldera" was introduced, suggesting a highly explosive volcanic event (Leonardi, 1968; Castellarin *et al*., 1982; Doglioni, 1984; Gianolla *et al*., 2010). The above-mentioned transitional contact, together with the absence of large caldera-fill deposits (Quick *et al*., 2009; Sinigoi *et al*., 2011), as clearly evidenced in the cross-section of Figure 2, cast however some doubts on the presence of a caldera structure for the Predazzo magmatic complex.

After the field survey, the use of QGis 2D and Polyworks (InnovMetrics) 3D softwares enabled us to convert the field relationships in a 3D surface model for the estimate of the volume of each portion of the complex. Due to the large volume of magmatic rocks that characterise the Predazzo complex, which is over 10 km^3 for an area of about 25 km^2, the edges of each magmatic unit within the complex were geometrically simplified to get a processable data, with an accuracy adequate for the focus of the present study. Such estimations were in fact aimed to obtain an order of magnitude for the volume of the different portions of the intrusion, as well as to develop a volumetric comparison between the intrusives and the volcanics. Results from the 3D modelling show that the entire PIC volume is 4.51 ± 0.136 *10^9 m^3, i.e. about 4.5 km^3; by contrast, the volume of the volcanic deposits

(lava flows, pillow lavas, lava breccias and explosive breccias) resulted slighlty larger, being $5.97 \pm 0.179 * 10^9$ m^3, i.e. about 6 km^3.

5. Petrography and whole rock geochemistry

Previous works on PIC (Visonà, 1997; Marrocchino *et al*., 2002) proposed a subdivision into four units, named M1 (shoshonitic silica-saturated series), M2 (shoshonitic silica-oversaturated series), M3 (potassic-alkaline series) and calc-alkaline series, this latter made up only by granitic and syenogranitic lithotypes. The improvement of the sample collection carried out in the present study, as well as new petrographic and geochemical data, suggest the subdivision of PIC into three main units (Figure 2), based on the silica saturation degree and the mineral assemblages, in which M1 and M2 have been merged into a single saturated (SS) series. According to our sampling, in fact, the rare oversaturated rocks that were found scattered within the complex do not support the existence of a clearly independent series (M2), which is also in contrast with the general overlap of the petrographic and geochemical features of the two previously defined M1 and M2 series. Silica saturation, resulting in the modal and normative presence of quartz, well displayed in the QAPF diagram (Figure 4), is in fact an important discriminating factor between the three units that constitute the PIC. The Shoshonitic Silica Saturated Unit (SS) is composed of a noticeable amount of quartz (up to 15-20%) from the less differentiated monzo-gabbroic to the evolved syenitic terms, while the Granitic Unit (GU) is constituted by granites and syenogranites with up to 35-40% of quartz. On the other side, the Shoshonitic Silica Undersaturated Unit (SU) suite is nepheline-normative along the entire differentiation trend.

5.1 Petrography

Shoshonitic Silica Saturated Unit (SS)

It represents the main portion of the intrusion (67% of PIC, with a volume of about 3.1 km^3), outcropping in the external part of the plutonic ring. This unit is mainly constituted by gabbros, monzo-gabbros, monzo-diorites, monzonites and syenites, and is thought to be derived from the first magmatic pulse. The gabbros crop out at the western border of the intrusion, dark-coloured, with medium to large grain size (1.2-6.8 mm) and, in some cases, mesocumulitc texture. The most common mineral phases are slightly zoned, light green and sometimes twinned augitic clinopyroxene (Cpx), olivine (Ol) and hypersthenic orthopyroxene (Opx). The intercumulus assemblage is composed of zoned plagioclase (Plag), magnetite (Mt), quartz (Qz) and pecilitic biotite (Bt). The monzo-gabbros represent the most abundant lithotype, with fine to large grain size (0.3-6.8 mm), hypidiomorphic texture and low colour index. Peculiar is the presence of augitic Cpx showing, in some cases, incipient local replacement by brown amphibole (Amph). The primary Amph are horneblende in composition, while Ol and Opx are absent. Other common phases are Plag, minor alkali feldspar (K-feld), Bt, sometimes altered to chlorite (Chlr), and Mt. Monzo-diorites are characterised by a grain size comparable to that of monzo-gabbros, and by a slightly higher colour index. Monzonites show fine to medium grain size (0.3-4.5 mm), with large K-feld, often characterised by perthitic structure, containing other mineral phases, (i.e. Bt and Plag). The augitic Cpx is often altered, while Amph is characterised by a compositional range from horneblende (primary formed terms) to actinolite-tremolite (replacing Cpx). Qz is also present, in an amount generally between 5 and 20%. Syenites are pink coloured, with granular structure: strongly perthitic K-feld is common, even if clouded by clay alteration; Qz and Plag are smaller in size and less abundant. The only mafic phases are represented by rare Cpx, Amph and Bt. Sphene (Sph), apatite (Ap) and zircon (Zirc), considered as accessory phases in almost all lithotypes, become quite abundant in syenites. At the southern border of the intrusion, directly in contact with the SS unit, outcrops a small dark-coloured mesocumulitic clinopyroxenitic body, with grain size ranging from medium to large (1.1-6.2 mm). It is

mainly constituted by Cpx, Ol, Bt, Mt and Plag. Its cumulitic nature, together with its marginal position, suggest that these rocks represent the first minerals crystallized at the border of the SS intrusion.

The SS hypabyssal monzo-gabbros and monzonites are mainly constituted by large Plag and Cpx embedded in a microcrystalline assemblage of K-feld, Bt, Plag, Cpx and Amph. They gradually pass into the volcanic lithotypes at the eastern and western side of the complex, as it is evident in the photomicrographs of Figure 3.

Granitic Unit (GU)

It outcrops in the central part of PIC, where forms a half-ring of about 2 km^2 in extension and about 1.1 km^3 in volume (25% of the intrusion). This unit is constituted by pink granites to syenogranites, sometimes with pegmatitic facies. The most abundant phase in such rocks is large-sized perthitic K-feld, with Plag, Qz and Fe-rich Bt in decreasing order of abundance. Accessory minerals are fluorite, allanite, Ap and Zirc, these two latters being often hosted in Qz crystals. Some samples are characterised by the presence of secondary Chlr crystals, formed over Bt, as well as centimetric black aggregates of tourmaline. Paganelli and Tiburtini (1964) and Menegazzo Vitturi *et al*. (1995) reported also the presence, in some cases, of small amounts of Amph intergrew with Bt. The relationships between granites and the SS series, suggest that the GU unit was intruded after SS, representing the second magmatic pulse of the PIC.

Shoshonitic Silica Undersaturated Unit (SU)

This series, about 0.3 km^3 in volume (8% of the PIC), outcrops in the easternmost part of the intrusion. It is characterised by the abundant presence of differentiated products, with subordinate gabbros, monzo-gabbros and monzonites, all of them nepheline (Ne)-normative in composition. The most mafic rocks (gabbros and monzo-gabbros) are characterised by the

presence of Plag, K-feld, salitic/aegirinaugitic Cpx, hastingsitic/Fe-pargasitic Amph, and minor Bt and Mt. Peculiar is also the presence of ugranditic-melanitic garnet (Grt). Monzonites are characterised by the absence of Qz, and by the presence of some altered Plag and K-feld, as well as rare altered Cpx, Amph and Bt. Syenites are grey coloured, with glomeroporphiric texture, where K-feld, melanitic Grt and minor altered Plag are the dominant phases. Small crystals of dark green Cpx and brown Amph are rarely present, embedded in a fine matrix constituted by K-feld, Plag, and dark green Cpx. Sph, ilmenite, Mt, Ap and epidote are present in the less differentiated lithotypes, while in the most differentiated rocks the accessory phases are Ti-Mt and Sph. In some differentiated samples the presence of nepheline has been documented (Vardabasso, 1930; Visonà, 1997). The finding of dike with similar undersaturated affinity cutting the GU unit suggest that the SU unit was the last pulse to enter the magma chamber.

5.2 Major element geochemistry

The three main units of the PIC (SS, SU and GU) show independent geochemical behaviour, well discriminated in QAPF (Figure 4), TAS (Figure 5) and K_2O vs. SiO_2 (Figure 6) diagrams. The entire dataset is characterised by a potassic affinity (Figure 7), only a few extremely differentiated syenogranites and syenites lie in the high-K affinity field.

The SS series is composed of gabbroic (mg# = 58-59) to monzo-gabbroic (mg# = 46-64), monzo-dioritic, monzonitic and syenitic samples, with SiO_2 and K_2O contents ranging from 42 to 68 wt% and 0.3 to 8.4 wt%, respectively, and Na_2O content up to 4.3 wt% in the most differentiated samples (Supplementary Table 1). Clinopyroxenites and cumulitic gabbros are characterised by a lower silica and potassium contents, ranging from 39 to 46 wt% and from 0.3 to 0.8 wt%, respectively (Supplementary Table 2). Their affinity is potassic and fits well with the SS series, although the abundant presence of Bt results in a normative (CIPW) silica undersaturation. These cumulitic samples are characterised by the highest MgO, TiO_2, CaO,

FeO and contents (Figure 8); except for the MgO/SiO_2 ratio, all diagrams confirm their affinity to the SS series. It is very likely that they could be derived from the early stage of fractional crystallization of the SS magma (Figure 8; see discussion below).

Rocks belonging to the GU are highly differentiated granitic to syenogranitic lithotypes, with high silica (up to 76 wt%) and alkali (7 to 11 $Na_2O + K_2O$ wt%) contents; their K/Na ratio is generally similar to that of SS series, except for few samples showing a low-K content (Supplementary Table 3). Granites and syenogranites are also characterised by TiO_2 and CaO contents comparable to those of the SS syenites, whereas their low MgO/SiO_2 and high FeO/SiO_2 ratios (Figure 8) highlight their peculiar petrological behaviour.

The SU series is composed of silica-undersaturated Ne-normative lithotypes, with K_2O (from 2.2 to 9.2 wt%) and Na_2O (0.4 up to 6.3 wt%) contents higher than those of SS rocks (Supplementary Table 4). A few gabbroic (mg# = 46-56) to monzogabbroic (mg# = 44) rocks belong to this series, that is generally composed of more differentiated terms (monzonites and syenites) with respect to the SS series, where the entire fractionation sequence is commonly represented. In Figure 8, the CaO and FeO contents of the entire dataset are plotted against silica and the parallel SS and SU differentiation patterns are clearly distinguishable. At comparable differentiation degree, SU samples are in fact characterised by higher Na_2O, but lower MgO, CaO, FeO and TiO_2 contents, further supporting their origin from an independent magmatic pulse, whose fractionation trend is related to the subtraction of compositionally and modally different mineral phases (see discussion below).

5.3 Trace element geochemistry

N-MORB-normalised (Sun and McDonough, 1989) trace element distributions for PIC lithotypes are reported in Figure 9. They show a general enrichment in Low Field Strength Elements (LFSE), such as Ba, Rb, Th, U, and K, and marked negative Nb and Ti anomalies. These features, together with the late Mt crystallisation and the consequent absence of Fe-Ti

enrichment trend, as well as with Bt, Amph and K-feld modal abundances, support the affinity to the shoshonitic series from active continental margins (Ewart, 1982).

All lithotypes show a marked enrichment in Pb, which ranges in composition from 20 up to about 90 ppm. Irrespective of lithotypes, this trace element represents a discrimination feature between SS and SU series, being slightly higher in the latter. Such a large positive anomaly is peculiar of the Dolomitic Triassic magmatism, as it is often accompanied by small polymetallic copper-bearing deposits (Nimis *et al*., 2012). Bedovina Mine represents in fact one of the most famous copper-wolfram deposits of the area, where the presence of a "sulphide copper phase", i.e. chalcopyrite, pyrite, sphalerite and galena, was genetically related to the effect of late magmatic lead-enriched fluids (Frizzo *et al*., 2010). Together with Pb, all HFSE are generally enriched in SU suite with respect to SS one. Clinopyroxenites and gabbros display normalised patterns lower than monzo-gabbros, monzo-diorites and monzonites, in agreement with their cumulitic nature. Sr and Ba show a behavior shifting from incompatible in mafic and intermediate lithologies to more compatible in sialic rocks, where the content of these elements decreases, in relation to Plag and K-feld fractionation, still manteining a slight positive anomaly. Similarly, from clinopyroxenites and gabbros to syenites a negative P anomaly is recorded, probably due to Ap fractionation. Extremely differentiated syenites are characterised by the highest content of incompatible elements (Rb, Th and Nb), but show moderate to strong Ba, Sr, P, Zr, Ti and Y depletions, suggesting a considerable removal of K-feld, Mt, Ap and Zirc (see discussion below).

N-MORB-normalised REE spidergrams (Sun and McDonough, 1989) show that PIC rocks are characterised by parallel but higher REE distribution (Figure 9, Supplementary Table 5) from clinopyroxenites and gabbros throughout monzo-gabbros, monzo-diorites, monzonites and syenites, as it would be expected by a normal fractionation trend. La_N/Yb_N ratio for the SS suite ranges from 5 to 7 in clinopyroxenites, up to 9 in gabbros, from 9 to 12 in monzo-gabbros and from 10 to 22 in monzo-diorites, monzonites and syenites. The SU lithotypes are

extremely enriched in LREE, with La_N/Yb_N reaching the highest values of 15-29. GU samples show a general REE enrichment, with La_N/Yb_N ranging between 8 and 21. Almost all SS and SU lithotypes, except for gabbros and clinopyroxenites, are also characterised by a negative Eu anomaly, probably related to feldspar fractionation: this anomaly, more evident in the differentiated syenite samples, is extremely marked in all GU samples.

The consistent increase of incompatible elements, like Rb, Nb, Zr, Th, Y, La, Ce, at increasing the differentiation index (SiO_2; Figure 10), is well evident. A gradual enrichment in Rb, Zr and Nb are observed both with increasing silica content and varying the serial alkalinity from SS to SU series. The highest values of Rb (ca. 330 ppm) and Zr (ca. 640 ppm) are observed in the syenitic rocks of the SU series. In Rb and Zr vs. SiO_2 diagrams (Figure 10), GU samples and clinopyroxenites plot in well separated fields. Clinopyroxenites are characterised by a Rb content below 50 ppm, while GU granites and syenogranites display higher concentrations (up to 440 ppm). At comparable SiO_2, Rb content is generally higher in the SU suite with respect to SS one. On the other hand, Zr content increases markedly from the less evolved monzo-gabbros (< 100 ppm) to SS and SU syenites, being the SU suite characterised by an average higher content. In GU lithotypes, the Zr content decreases markedly from 360 to 80 ppm with increasing silica content up to 77 wt%, probably due to Zirc fractionation.

6. Mineral chemistry

The composition of the most representative PIC mineral phases was carried out to better characterise the geochemical features of SS, SU and GU suites and to develop the mass balance fractionation model illustrated below (see also Figures 8 and 10). Fe^{2+}/Fe^{3+} ratio was stoichiometrically determined for the anhydrous phases, whereas for Amph and Bt it was calculated according to the models of Leake *et al*. (1997) and Dymek (1983) respectively.

6.1 Olivine

Ol (Supplementary Table 6), often altered to iddingsite, is present only in a few mafic samples of the SS series, like clinopyroxenites, gabbros and rare monzo-gabbros. Its compositional range varies from Fo_{62} to Fo_{38} in both gabbros and clinopyroxenites.

6.2 Magnetite

Magnetite (Figure 11, Supplementary Table 6) is characterised by an almost homogeneous composition among the three magmatic suites. The TiO_2 content is in fact always below 5 wt%, reaching its lowest values in the more differentiated samples (i. e. monzonites) as well as in the GU syenogranites, where is slightly above zero.

6.3 Pyroxenes

As for Ol, Opx (Figure 11, Supplementary Table 7) is present only in a few mafic samples of the SS series. It occurs in reaction relationship with Ol in clinopyroxenites and gabbros, and in a few cases it is also present in monzonites. Its composition ranges from En_{71-61} in clinopyroxenites, En_{69-63} in gabbros to En_{60-52} in monzonites. Cpx (Figure 11, Supplementary Table 7) is reported from both SS and SU suites, with different composition for the two suites. Cpx from SS series are quite homogeneous, being diopsidic and augitic in composition with a Wo content < 50. On the other hand, SU Cpx show a generally higher CaO content, with Wo > 50, ranging from salitic to ferro-salitic in composition, almost comparable to Cpx from alkaline rocks as described by Dal Negro *et al*. (1986).

6.4 Amphibole

Analogously to Cpx, Amph (Figure 12, Supplementary Table 8) is very different between the two series, the alkali content is a peculiar feature of the SU lithotypes. Amph from SS gabbros to syenites are mainly Mg-hornblende to actinolite in composition, followed by edenite and

Fe-edenite terms. In this series, actinolite is a reaction product upon primary Mg-hornblende and Cpx. On the other hand, Amph from SU gabbros to syenites range in composition between hastingsite, Mg-hastingsitie and Fe-pargasite. At comparable evolution degree (from gabbros to syenites), Amph composition show a remarkable differences between the two suites (Figure 12), SS Amph being higher in SiO_2, as well as lower in K_2O, Na_2O and Al_2O_3 contents with respect to Amph from SU series. In this latter, Na_2O and K_2O contents of Amph can reach up to 2.6 and 2.2 wt% respectively. Amph is absent in GU granites and syenogranites.

6.5 Biotite

Bt (Figure 12, Supplementary Table 9) occurs in SS, SU and GU lithotypes, testifying to the K-affinity of the PIC magmas. This phase is generally characterised by a high TiO_2 (0.9-6.1 wt%) content, except for granites and syenogranites of the GU suite ($TiO_2 \leq 3.3$ wt%), where Bt have also low Al_2O_3 and SiO_2 contents. At comparable SiO_2 content, Bt from SU monzo-gabbros are slightly enriched in Al_2O_3 with respect to those from SS monzo-gabbros (Figure 12). Discriminating feature is also the FeO content of Bt, separating the iron-rich GU Bt (FeO content up to 28.5 wt%) from the SS and SU ones. On the base of the FeO vs. SiO_2 content, SS Bt plot into two distinct fields: a first one is characterised by a lower Fe/Si ratio, and a second one, is described by an higher Fe content. Both of them are representative for Bt from gabbros to monzonites. SU Bt composition, whose iron content range from 10.0 to 11.4 wt%, fall within the second compositional spectrum (Figure 12).

6.6 Feldspars

Plag (Figure 11, Supplementary Table 10) is a common phase in all PIC rocks**,** often characterised by oscillatory zoning. In SS samples, Plag shows a compositional range from An_{81-56} in clinopyroxenites, An_{78-49} in monzo-gabbros and An_{50-43} in monzonites and An_7 in

the syenites. In the SU series, the average composition is about An_{48-29} in monzo-gabbros and monzonites. Orthoclase content in more differentiated lithotypes generally reaches values up to about 7%. K-feld (Figure 11, Supplementary Table 10), one of the main phases that characterise GU granites and syenogranites, has an almost negligible An content, as the orthoclase term increases up to 90%.

7. FC processes in the magma chamber

Petersen *et al*. (1980), Gasparotto and Simboli (1991), and Bonadiman *et al*. (1994) hypotesised the derivation of the intrusive rocks of the Dolomites from a monzo-gabbroic magma that mainly experienced fractional crystallization (FC) processes in an almost closed system, with subsequent generation of Cpx cumulates. PIC is the only multi-pulse intrusion of the Dolomitic Area in which more than one geochemical suite can be identified. Thus, major/trace element whole rock compositions, as well as major element mineral chemistry, were used for develop a mass balance calculation for modelling the main differentiation trends for the geochemical suites of the PIC (SS, GU and SU). This model is typically applied to effusive rocks. In closed system crystallization, assuming equilibrium conditions, also coarse grained intrusive rocks can be considered as magmatic liquids. According to the previous studies on this area (Petersen *et al*., 1980; Gasparotto and Simboli, 1991; Bonadiman *et al*., 1994) and on the petrographic features above mentioned, PIC rocks crystallization occurred in closed system-like conditions, making it possible to model their genesis via FC processes. This statement is also streghten by the comparison with the very similar composition of basaltic and hypoabyssal rocks outcropping in the area (Casetta *et al*., in prep.).

Aim of our model is to better constrain the genetic relationships between the various lithotypes (Figures 8, 10 and 13). In this respect, for example, the link between clinopyroxenites and gabbros or monzo-gabbros of both SS and SU series is not well defined.

Thus, two FC models were developed, for both SS and SU suites. FC calculations have been firstly attempted by using MELTS and Rhyolite-MELTS softwares: however, being the SS and SU magmatic suites enriched in Amph and Bt, no reliable results have been produced. In fact, application of such softwares to magmas fractionating under wet conditions is limited by the lack of appropriate thermodynamic models for hydrous mafic silicates, particularly Amph and Bt (Gualda *et al*., 2012). As a consequence, least squares mass balance calculations have been computed to simulate the FC processes that generated the PIC.

Monzo-gabbros were taken as starting material, while the final products were syenites. Accuracy on the major element mass balance model has been evaluated by means of the least squares error (r^2) between natural and calculated compositions. Trace element distribution in the calculated compositions was obtained using the partition coefficients (Kd, Supplementary Table 11) extracted by the GERM Database (earthref.org/KDD) and using the formulation of Shaw (1970) for Rayleigh fractionation, $C_L=C_0*F^{(D-1)}$, where: C_0 is the amount of the chosen element in the starting (natural) magma; C_L the amount of trace element calculated in the arrival magma; F the residual melt percentage; D the partition coefficients weighted for the percentage of fractionated minerals obtained by the mass balance calculation.

7.1 SS series

Monzo-gabbro FC43B was chosen as the nearest composition to a primary magma for this series (Supplementary Table 12) for its low SiO_2 and high mg#, Ni and Co amounts. The first step towards the more differentiated monzo-gabbro EM53 (Figure 13) accounts for the removal of 54% of a solid assemblage (SA1SS, $r^2 = 0.89$) made up of Ol (8.3%), Opx (5.1%), Cpx (21.3%), Plag (49.4%), Ap (2.3%), Mt (3.5%) and Bt (10.1%) with an overall gabbroic composition. The errors in the model for most of the trace elements are lower than 2% (Supplementary Table 12), except for Th and La, due to their low concentrations in the primary sample. The second stage from monzo-gabbro EM53 to monzonite EM85 is modelled

by removing 73% of a monzo-gabbroic assemblage (SA2SS, $r^2 = 0.68$), constituted by K-feld (6.2%), Amph (0.7%), Cpx (17.6%), Plag (52.2%), Ap (1.4%), Mt (5.3%) and Bt (16.6%), with errors on trace element contents lower than 14%. The last step from monzonite EM85 to syenite EM110 is derived by removal of 47% of a solid assemblage (SA3SS, $r^2 = 0.26$) of K-feld (16.3%), Amph (2.6%), Cpx (12.1%), Plag (41.9%), Ap (1.1%), Mt (4.1%), Bt (10.5%), Qz (10.6%), and Zirc (0.8%), with monzo-dioritic composition. Having Qz and Zirc the same effect on SiO_2 balance, Zirc modal fractionation (0.8%) was calculated based on Zr trace element modelling (Figure 10). Trace element composition of theoretical melt match very well with that of the natural magma, resulting in an error lower than 2% for all the elements except for Th (20%), due to its low concentration in the syenitic sample (9 ppm), and La (16%). Syenite is the result of 94% fractionation (Figures 8 and 10) corresponding to a solid residuum made up of gabbroic to monzo-gabbroic and monzo-dioritic lithotypes. The compositions calculated for the three solid assemblages (Figure 13) are similar to those of natural clinopyroxenitic and gabbroic to monzo-dioritic lithotypes found within the SS suite (Figure 8 and Figure 10), lending further support to the theoretical results. Moreover, several FC modelling attempts have been made to find a link between the SS suite and the GU granites and syenogranites. However, the mass balance calculation did not explain the genesis of the GU rocks via simple FC trends belonging to the SS suite.

7.2 SU series

The parent magma chosen as starting point for the modelling of the fractionation of this suite (Supplementary Table 13) was the nepheline normative monzo-gabbro EM10, characterised by high mg#, Ni and Co amounts (Figure 13). Monzo-gabbro EM10 can reach the monzonite EM7 by 63% fractionation of a solid assemblage (SA1SU, $r^2 = 0.98$), constituted by K-feld (4.7%), Amph (12.2%), Cpx (27.5%), Plag (35.9%), Ap (1.7%), Mt (11.0%) and Bt (7.0%), with gabbroic composition. The trace element (Rb, Ba, Th, Nb, La, Ce, Pb, Sr, Nd, Zr and Y)

distribution for this first step has an errors < 4%. The second stage from monzonite EM7 to syenite 11* can be modelled by removal of 44% of a monzo-dioritic assemblage (SA2SU, r^2 = 0.73) constituted by K-feld (32.1%), Amph (14.6%), Plag (44.2%), Ap (2.4%), Mt (4.1%) and Bt (2.6%). Trace element distribution errors are <1%, except for Pb and Th, whose errors are respectively 14% and 23%, being this latter due to the high amount of Th in the more differentiated rock. SU Syenite is the result of 79% fractionation (Figures 8 and 10) corresponding to a solid residuum made up of gabbroic to monzo-dioritic rocks (Figure 13), that fits well with the compositional spectrum of the similar lithotypes found within this portion of the complex, as highlighted also by the variation diagrams of Figure 8 and Figure 10.

8. Discussion

Whole rock major and trace element composition, as well as mineral chemistry and detailed field surveys, allowed to discriminate between the three magmatic suites that compose the PIC, after a re-evaluation of the petrogenetic subdivision proposed by Visonà (1997) and Marrocchino *et al*. (2002). All the three suites, namely SS, SU and GU are characterised marked Nb and Ti negative anomalies and a high positive Pb anomaly. Modal abundance of Bt, Amph and K-Feld, as well as late Mt crystallisation, leading to the lack of a Fe-Ti enrichment trend, support the by K-affinity of the magmas, typical of the shoshonitic series from active continental margins (Ewart, 1982). The progressive differentiation trend for both SS and SU series is marked by the appearance of a significant Eu negative anomaly, particularly in the more evolved syenites. On the other side, SU suite is characterised by lower K/Na ratios, as well as by higher LFSE and LREE content than SS and GU. Amph, absent in GU lithotypes, is markedly enriched in Al_2O_3, Na_2O and K_2O in the SU with respect to the SS suite, while iron-rich Bt is a peculiar feature of GU rocks. All these features lead to speculate

about the belonging of the SU suite to a magma pulse different to that of the SS one, likely related to spatial and/or temporal heterogeneities of their sources.

By means of this discrimination, mass balance calculations have been developed for both SS and SU series in order to model the FC processes in an almost closed system (Petersen *et al*., 1980; Gasparotto and Simboli, 1991; Bonadiman *et al*., 1994) responsible for the genesis of all PIC lithologies (Figures 8, 10 and 13). The calculated subtracted solids are quite similar in composition to the natural pyroxenitic and gabbroic to monzo-dioritic samples found within the complex, further supporting the accuracy of the model and suggesting that FC is the main differentiation process controlling the magmatic evolution. Still unsolved remains the relationship between the GU granites and syenogranites and the SS-SU suites, because of the independent geochemical behaviour of the formers. The alkali and silica content of the GU body, together with a marked Eu negative anomaly, may indicate a differentiation from a silica-oversaturated series, but the lack of any differentiated volcanic rock with similar features in the area surrounding PIC, as well as of any petrological relationships with the intrusive rocks of the complex, does not allow to put forward a robust cogenetic mechanism. Visonà (1997) proposed the existence of a calc-alkaline and/or oversaturated trend able to generate the granites and syenogranites. However, several attempts to reconstruct the geochemical features of the GU lithotypes via FC processes from the SS suite have been unsuccesfull. It has also to be noted that no rhyolitic products are found within the volcanics, thus, contrary of what occurs for the other two seires, there would not be a correspondence between GU and its effusive counterpart.

Together with the petrological distinction of the three suites, an accurate study of the field relationships of the intrusive portions, the volcanics, and the dike swarm outlines a detailed PIC temporal evolution (Figure 14) and defines the relationships with the effusive portions of the complex. According to our findings, PIC evolution is characterised by the emplacement of three magma batches with different petrological affinities in a relatively short time. The first

most voluminous SS pulse (3.1 km^3) was emplaced as what nowadays appears as an external ring. It was followed by the GU intrusion (1.1 km^3) in the central part of the complex, and then by the alkaline SU batch (0.3 km^3) in the eastern portion of the PIC. From field survey and volume estimates, it is evident that the SU series represents a minor contribution to the whole PIC: it likely constitutes the ultimate melt produced in the vanishing stage of the magmatic intrusion. During this last stage, several undersaturated dikes intruded the SS and GU lithotypes, indirectly constraining the temporal relationships between the three intrusive bodies by means of these cross-cutting relationships.

The presence of a fourth silica-oversaturated suite, identified by Visonà (1997) and Marrocchino *et al*. (2002) has been furthermore ruled out because of the paucity of oversaturated rocks scattered within the PIC, and of the overlap of their petrographic and geochemical features with the SS suite, in case of both whole rock and mineral chemistry. The origin of such rocks, whose Qz modal content lies between 4 and 15%, could be instead explained by the last stage of the FC processes for the SS suite (Figure 13). In this, the genesis of a SS syenite from a monzonitic material results by the removal of a monzo-dioritic solid assemblage with up to 11% Qz content (Supplementary Table 12), that is close to the natural monzo-diorites defined as "oversaturated" by Visonà (1997) and Marrocchino *et al*. (2002). This evidence suggests that the rare oversaturated rocks in PIC are fractionation products of the SS suite, making unlikely the existence of an independent oversaturated suite from which the GU lithotypes could have been derived.

The extended fieldwork along the contact between the PIC and the surrounding volcanites provided also important constraints about the so-called "Predazzo caldera" definition, introduced by Leonardi (1968), Castellarin *et al*. (1982), Doglioni (1984) and Gianolla *et al*. (2010) to take somehow into account the ring-shape of the PIC. In this context the transitional magmatic contact between the volcanics and the SS lithotypes (Figure 3) that has been found

on both the eastern and western part of the complex, as well as the lack of evolved caldera-filling materials, casts some doubts on the existence of a structure of this type.

9. Conclusions

Within the Dolomitic Area, the Predazzo magmatic complex is the most developed volcano-plutonic centre, being characterised by a 6 km^3 of volcanites surrounding 4.5 km^3 of intrusive rocks (PIC). This area is an entirely preserved magmatic complex, in which the relationships between the intrusion, the dike swarm, the host rocks and the volcanic products are exposed onto the surface, making it a perfect petrographic and petrological laboratory. Moreover, the PIC multi-pulse nature and high petrological variability point out its key role to constrain the main features of the Triassic magmatism in the Dolomites and in the whole Southern Alps domain. The combination of field, petrographic and petrological studies leads to the following considerations:

1. The K-affinity, the marked Nb and Ti negative anomalies, as well as the widespread occurrence of Amph and Bt in almost all PIC rocks, indicate a relationship with the shoshonitic series from active continental margins, suggesting the presence of a subduction setting in the Southern Alps domain, as already hypotised by Zanetti *et al.* (2013). However, the model of mixing between mantle-derived basic and crustal-derived acid magmas put forward by Sinigoi *et al*. (2011, 2016) for the Ivrea-Verbano magmatic complex and the related upper crustal section leaves the question still unanswered.

2. The PIC is a multi-pulse body, dominated by three main magmatic suites (SS, GU and SU), characterised by different HFSE and LREE contents, as well as by peculiar mineral assemblages, where Amph and Bt are a clear distinctive feature.

3. SS and SU differentiation trends explain the occurrence of cumulitic gabbros and pyroxenites within the complex, as well as the scattered presence of silica oversaturated lithotypes. The origin and nature of the GU suite remains uncertain, because of the absence of similar effusive products in the surrounding area and due to the impossibility to model the genesis of granites and syenogranites via simple FC process for the SS suite. Further studies are under way to investigate the relationships between such rocks, the PIC intrusive and effusive products.

4. The magmatic transitional contact identified between the PIC and the volcanites, as well as the lack of "caldera-filling"-like materials, lead to exclude the presence of a calderic collapse structure in the area, invoked by several authors to explain the ring-shape of the complex. By means of these considerations, the outcropping relationships between the PIC, the volcanic products, and the host rocks have to be considered in a different light. Such a finding will constitute a fundamental starting point to develope future accurate models on the magma chamber emplacement history and timing, in one of the few worldwide examples of an entirely preserved and "frozen" volcano-plutonic system.

Acknowledgements

Authors thank Raul Carampin (Department of Geosciences and CNR-IGG, University of Padova, Italy), for the electron microprobe (EMP) analyses. Authors would also acknowledge the Editor Robert J. Stern, whose suggestions significantly improved the manuscript, as well as Silvio Mollo and two anonymous Reviewers for their thoughtful comments.

References

Allahyari, K., Saccani, E., Rahimzadeh, B. and Zeda, O., 2014, Mineral chemistry and petrology of highly magnesian ultramafic cumulates from the Sarve-Abad (Sawlava)

ophiolites (Kurdistan, NW Iran): New evidence for boninitic magmatism in intra-oceanic fore-arc setting in the Neo-Tethys between Arabia and Iran: Journal of Asian Earth Sciences, v. 79, p. 312-328.

Armienti, P., Corazzato, C., Groppelli, G., Natoli, E. and Pasquarè, G., 2003, Geological and petrographical study of Montecampione Triassic subvolcanic bodies (Southern Alps, Italy): preliminary geodynamic results: Bollettino della Società Geologica Italiana, v. 2, p. 67-78.

Barth, S., Oberli, F., Meier, M., Blattner, P., Bargossi, G. M. and Di Battistini, G., 1993, The evolution of a calc-alkaline basic to silicic magma system: geochemical and Rb–Sr, Sm–Nd, and $^{18}O/^{16}O$ isotopic evidence from the Late Hercynian Atesina-Cima d'Asta volcanoplutonic complex, northern Italy: Geochimica et Cosmochimica Acta, v. 57, p. 4285-4300.

Beccaluva, L., Dal Piaz, G.V. and Macciota, G., 1984, Transitional to normal MORB affinities in ophiolitic metabasites from the Zermatt-Saas, Combin and Antrona units, Western Alps: implications for the paleogeographic evolution of the Western Tethyan Basin: Geologie en Mijnbouw, v. 63, p. 165-177.

Beccaluva, L., Coltorti, M., Saccani, E., Siena, F. and Zeda, O., 1996, Triassic Magmatism and Jurassic Ophiolites at the Margins of the Adria Plate, in Finetti I. R. ed., Crop Project: Deep Seismic Exploration of the Central Mediterranean and Italy: Elsevier, v. 28, p. 607-622.

Beccaluva, L., Bianchini, G., Bonadiman, C., Coltorti, M., Macciotta, G., Siena, F. and Vaccaro, C., 2005, Within-plate Cenozoic volcanism and lithospheric mantle evolution in the western-central Mediterranean area, in Finetti I. R. ed., Crop Project: Deep Seismic Exploration of the Central Mediterranean and Italy: Elsevier Special Volume, p. 641-664.

Bellieni, G., Fioretti, A. M., Marzoli, A. and Visonà, D., 2010, Permo–Paleogene magmatism in the eastern Alps: Rendiconti Lincei, v. 21, p. S51-S71.

Bernoulli, D. and Lemoine, M., 1980, Birth and Early Evolution of the Tethys: the Overall Situation: Mémoires du Bureau de recherches géologiques et minières, v. 115, p. 168-179.

Bertotti, G., Picotti, V., Bernoulli, D. and Castellarin, A., 1993, From rifting to drifting: tectonic evolution of the South-Alpine upper crust from the Triassic to the Early Cretaceous: Sedimentary Geology, v. 86, p. 53-76.

Bonadiman, C., Coltorti, M. and Siena, F., 1994, Petrogenesis and T-fO_2 estimates of Mt. Monzoni complex (Central Dolomites, Southern Alps): a Triassic shoshonitic intrusion in a trascurrent geodynamic setting: European Journal of Mineralogy, v. 6, p. 943-966.

Bonin, B., 1988, From orogenic to anorogenic environments: evidence from associated magmatic episodes: Schweizerische Mineralogische und Petrographische Mitteilungen, v. 68, p. 301-311.

Brack, P., Mundil, R., Oberli, F., Meier, M. and Rieber, H., 1996, Biostratigraphic and radiometric age data question the Milankovitch characteristics of the Latemar cycles (Southern Alps, Italy): Geology, v. 24, no. 4, p. 371-375.

Brack, P., Mundil, R., Oberli, F., Meier, M. and Rieber, H., 1997, Biostratigraphic and radiometric age data question the Milankovitch characteristics of the Latemar cycles (Southern Alps, Italy): Reply: Geology, v. 25, no. 5, p. 471-472.

Brack, P., Rieber, H., Nicora, A. and Mundil, R., 2005, The Global boundary Stratotype Section and Point (GSSP) of the Ladinian Stage (Middle Triassic) at Bagolino (Southern Alps, Northern Italy) and its implications for the Triassic time scale: Episodes, v. 28, no. 4, p. 233-244.

Brondi, A., Mittempergher, M., Panizza, M., Rossi, D., Sommavilla, E. and Vuillermin, F., 1977, Note Illustrative della Carta Geologica d'Italia, Foglio 028 La Marmolada: Servizio Geologico d'Italia, Roma, scale 1:50.000, 1 sheet.

Calanchi, N., Lucchini, F. and Rossi, P.L., 1977, M. Agnello: un apparato a condotto centrale delle Dolomiti: Mineralogica et Petrografica Acta, v. 21, p. 221-229.

Calanchi, N., Lucchini, F. and Rossi, P.L., 1978, The volcanic rocks from the Mount Agnello area (Fiemme Valley, Italy): a contribution to the knowledge of the Mid-Triassic magmatism of the Southern Alps: Tschermaks Mineralogische und Petrographische Mitteilungen, v. 25.

Cassinis, G., Cortesogno, L., Gaggero, L., Perotti, C. R. and Buzzi, L., 2008, Permian to Triassic geodynamic and magmatic evolution of the Brescian Prealps (eastern Lombardy, Italy): Bollettino della Società Geologica Italiana, v. 127, no. 3, p. 501-518.

Castellarin, A., Lucchini, F., Rossi, P.L., Simboli, G., Bosellini, A. and Sommavilla, E., 1980, Middle Triassic magmatism in Southern Alps II: A geodynamic model: Rivista Italiana di Paleontologia e Stratigrafia, v. 85, no. 3-4, p. 1111-1124.

Castellarin, A., Lucchini, F., Rossi, P.L., Sartori, L., Simboli, G. and Sommavilla, E., 1982, Note geologiche sulle intrusioni di Predazzo e dei M. Monzoni. Guida alla geologia del Sudalpino centro-orientale: Guide geologiche regionali S.G.I., p. 211-219.

Castellarin, A., Lucchini, F., Rossi, P.L., Selli, L. and Simboli, G., 1988, The Middle-Triassic magmatic-tectonic arc development in the Southern Alps: Tectonophysics, v. 146, p. 79-89.

Castellarin, A., 1983, Alpi Meridionali. Magmatismo e tettonica triassica: Memorie della Società Geologica Italiana, v. 24, p. 5-7.

Coltorti, M., Siena, F. and Visonà, D., 1996, Aspetti petrologici del magmatismo Triassico dell'area di Predazzo: Libro dei Riassunti, 78° Riunione Estiva S.G.I.

Cornelius, H.P. and Cornelius-Furlani, M., 1924, Zur Geologie der Tuffbildungen im Marmolatagebiet (Südtirol): Zentralblatt für Geologie und Paläontologie, v. 12, p. 366-373.

Dal Negro, A., Cundari, A., Piccirillo, E.M., Molin, G.M. and Uliana, D., 1986, Distinctive Crystal-chemistry and Site Configuration of the Clinopyroxene from Alkali Basaltic Rocks - the Nyambeni Clinopyroxene Suite, Kenya: Contributions to Mineralogy and Petrology, v. 92, p. 35-43.

Dal Piaz, G., 1993, Evolution of Austro-Alpine and Upper Penninic basement in the northwestern Alps from Varisican convergence to post-Varisican extension: Pre-Mesozoic geology in the Alps: Springer-Verlag, p. 327-344.

Dal Piaz, G., Bistacchi, A. and Massironi, M., 2003, Geological outline of the Alps: Episodes, v. 26, no. 3, p. 175-180.

Doglioni, C., 1984, Triassic diapiric structure in the central Dolomites (Northen Italy): Eclogae Geologicae Helvetiae, v. 77, p. 2.

Doglioni, C., 1987, Tectonics of the Dolomites (Southern Alps, Northern Italy): Journal of Structural Geology, v. 9, p. 181-193.

Doglioni, C. and Bosellini, A., 1987, Eoalpine and Mesoalpine tectonics in the Southern Alps: Geologische Rundschau, v. 76, no. 3, p. 735-754.

Doglioni, C. and Carminati, E., 2008, Structural styles and Dolomites field trip: Memorie Descrittive della Carta Geologica d'Italia, v. 82, p. 280.

Dymek, F.R., 1983, Titanium, aluminium and interlayercalation substitution in biotite from high-grade gneisses, West Greenland: American Mineralogist, v. 68, p. 880-899.

Ewart, A., 1982, The mineralogy and petrology of Tertiary-Recent orogenic volcanic rocks: with special reference to the andesitic-basaltic compositional range, in Thorp R.S. ed., Andesites: Orogenic Andesites and Related Rocks: John Wiley and Sons, New York, v. 724, p. 25-95.

Fondazione Dolomiti Dolomiten Dolomites Dolomitis UNESCO, Sito web ufficiale delle Dolomiti Patrimonio dell'Umanità UNESCO, www.dolomitiunesco.info

Frizzo, P., Peruzzo, L. and Dellantonio, E., 2010, The copper-wolfram deposit of Bedovina (Trento, Italy): Geo.Alp, v. 7, p. 55-70.

Gasparotto, G. and Simboli, G., 1991, Mineralogia, petrografia e schemi evolutivi delle magmatiti triassiche del complesso di Cima Pape (Dolomiti Orientali): Mineralogica et Petrografica Acta, v. 34, p. 205-234.

GERM, Partition Coefficient (Kd) Database, development and maintenance by the EarthRef.org Database Team, Data contribution by Roger Nielsen. Earthref.org/KDD.

Gianolla, P., Avanzini, M., Breda, A., Kustatscher, E., Preto, N., Roghi, G., Furin, S., Massari, F., Picotti, V. and Stefani, M., 2010, Dolomites, 7th International Triassic Field Workshop, Field trip to the World Heritage Site of the Tethyan Triassic. September 5-10 2010, Dolomites, Southern Alps, Italy. With the adesion of Fondazione Dolomiti-Dolomiten-Dolomites-Dolomitis Unesco.

Gianolla, P., 1992, Evoluzione mediotriassica del vulcanismo di Rio Freddo (Api Giulie, Italia): Memorie di Scienze Geologiche, v. 44, p. 193-209.

Gianolla, P., 2011, Il Libro di Roccia: Cierre Edizioni.

Gualda, G. A. R., Ghiorso, M. S., Lemons, R. V., Carley, T. L., 2012, Rhyolite-MELTS: a Modified Calibration of MELTS Optimized for Silica-rich, Fluid-bearing Magmatic Systems: Journal of Petrology, v. 53, p. 875-890.

Le Maitre, R. W., Bateman, P., Dudek, A., Keller, J., Lameyre Le Bas, M. J., Sabine, P. A., Schmid, R., Sorensen, H., Streckeisen, A., Woolley, A. R. and Zanettin, B., 1989, A classification of igneous rocks and glossary of terms: Blackwell, Oxford.

Leake, B. E., Arps, C. E. S. and Birch, W. D., 1997, Nomenclature of amphiboles: Report of the Subcommittee on Amphiboles of the International Mineralogica Association, Commission on New Minerals and Mineral Names: American Mineralogist, v. 82, p. 1019-1037.

Lemoine, M., Tricart, P. and Boillot, G., 1987, Ultramafic and gabbroic ocean floor of the Ligurian Tethys (Alps, Corsica, Appennines): In search of a genetic model: Geology, v. 15, p. 622-625.

Leonardi, P., 1968, Centro eruttivo di Predazzo: Le Dolomiti, Geologia dei monti tra Isarco e Piave, v. 52.

Lippolt, H. and Pidgeon, R., 1974, Isotopic mineral ages of a diorite from the Eisenkappel intrusion, Austria: Zeitschrift für Naturforschung, v. 29a.

Lucchini, F. and Morten, L., 1977, An example of flow differentiation: clinopyroxenite of the Predazzo igneous complex (north Italy): Lithos, v. 10, p. 39-47.

Lucchini, F., Rossi, P.L. and Simboli, G., 1982, Il magmatismo triassico dell'area di Predazzo (Alpi Meridionali, Italia). In A. Castellarin e G.B. Vai (Eds), Guida alla Geologia del Sudalpino centro-orientale: Guide Geologiche Regionali Società Geologica Italiana, p. 221-230.

Marocchi, M., Morelli, C., Mair, V., Klötzli, U. and Bargossi, G. M., 2008, Evolution of large silicic magma systems: new U–Pb zircon data on the NWPermian Athesian Volcanic Group (Southern Alps, Italy): Journal of Geology, v. 116, p. 480-498.

Marrocchino, E., Coltorti, M., Visonà, D. and Thirwall, M.F., 2002, Petrology of Predazzo magmatic complex (Trento, Italy): Geochimica et Cosmochimica Acta, v. 66, no. 15A, suppl. 1, p. A486-A486.

Marzari Pencati, G., 1820, Notizia sopra un granito in massa terziario sovrapposto al calcare secondario nel fiume Avisio: Supplemento al "Nuovo Osservatorio Veneziano", v. 118-127.

Menegazzo Vitturi, L., Visonà, D. and Zantedeschi, C., 1995, Amphibole composition in rocks from Predazzo volcano-plutonic complex (Southern Alps, Italy): Memorie di Scienze Geologiche, v. 47, p. 87-94.

Mietto, P., Manfrin, S., Preto, N., Rigo, M., Roghi, G., Furin, S., Gianolla, P., Posenato, R., Muttoni, G., Nicora, A., Buratti, N., Cirilli, S., Spötl, C., Ramezani, J. and Bowring, S.A., 2012, The Global Boundary Stratotype Section and Point (GSSP) of the Carnian Stage (Late Triassic) at Prati di Stuores/ Stuores Wiesen Section (Southern Alps, NE Italy): Episodes, v. 35, no. 3, p. 414-430.

Mundil, R., Brack, P. and Laurenzi, M. A., 1996, High resolution U/ Pb single zircon age determinations: new constrints on the timing of Middle Triassic magmatism in the Southern Alps: Libro dei Riassunti, 78° Riunione estiva S.G.I.

Mundil, R., Brack, P., Meier, M., Rieber, H. and Oberli, F., 1996, High resolution U-Pb dating of middle Triassic volcaniclastics: time-scale calibration and verification of tuning parameters for carbonate sedimentation: Earth and Planetary Science Letters, v. 141, p. 137-151.

Nimis, P., Omenetto, P., Giunti, I., Artioli, G. and Angelini, I., 2012, Lead isotope systematics in hydrothermal sulphide deposits from the central-eastern Southalpine (northern Italy): European Journal of Mineralogy, v. 24, p. 23-37.

Paganelli, L. and Tiburtini, R., 1964, The Predazzo granite, North Italy: Mineralogica et Petrographica Acta, v. 10, p. 57-79.

Pearce, J. A., 1982, Trace elements characteristics of lavas from destructive plate boundaries, in Thorpe E. S. ed., Andesites: New York, John Wiley and Sons, p. 525-548.

Petersen, J. S., Morten, L., Simboli, G. and Lucchini, F., 1980, REE abundances in the Predazzo-Monzoni intrusive complex, Dolomites, North Italy: Rivista Italiana di Paleontologia e Stratigrafia, v. 85, p. 1065-1080.

Piccardo, G. B., Rampone, E., Vannucci, R. and Cimmino, F., 1994, Upper mantle evolution of ophiolitic peridotites from the Northern Apennine: Petrological constraints to the geodynamic processes: Memorie della Società Geologica Italiana, v. 8, p. 137-148.

Pisa, G., Castellarin, A., Lucchini, F., Rossi, P.L., Simboli, G., Bosellini, A. and Sommavilla, E., 1979, Middle Triassic magmatism in Southern Alps. I: a review of general data in the Dolomites: Rivista Italiana di Paleontologia e Stratigrafia, v. 85, no. 3-4, p. 1093-1110.

Quick, J. E., Sinigoi, S., Snoke, A.W., Kalakay, T. J., Mayer, A. and Peressini, G., 2003, Geologic map of the Southern Ivrea-Verbano Zone, Northwestern Italy: U.S. Geological Survey.

Quick, J. E., Sinigoi, S., Peressini, G., Demarchi, G., Wooden, J. L. and Sbisà, A., 2009, Magmatic plumbing of a large Permian caldera exposed to a depth of 25 km: Geology, v. 37, p. 603-606.

Rampone, E. and Piccardo, G.B., 2000, The ophiolite-oceanic lithosphere analogue: new insights from the Northern Apennines (Italy), In Dilek J., Moores E., Elthon D. and Nicolas A. eds., Ophiolites and Oceanic Crust: New Insights from Field Studies and Ocean Drilling Program: Geological Society of America Memoir, Special Paper, v. 349, p. 21-34.

Rossi, P.L., Viel, G. and Simboli, G., 1976, Significato paleogeografico e magmatico-tettonico della serie vulcano-clastica ladinica superiore nell'area del Monte Civetta: Bollettino della Società Geologica Italiana, v. 95, p. 433-458.

Salomon, W., 1895, Geologische und palaontologische Studien fiber die Marmolata: Palaeontographica, v. 42, no. 1, p. 210.

Scandone, P., 1975, Triassic seaways and the Jurassic Thethis Ocean in the central Mediterranean area: Nature, v. 256, p. 5513.

Schmid, S. M., Bernoulli, D., Fügenschuh, B., Matenco, L., Schefer, S., Schuster, R., Tischler, M. and Ustaszewski, K., 2008, The Alpine-Carpathian-Dinaridic orogenic system: correlation and evolution of tectonic units: Swiss Journal of Geosciences, v. 101, no. 1, p. 139-183.

Schmid, M. S., Bernoulli, D., Fügenschuh, B., Georgiev, N., Kounov, A., Matenco, L., Oberhansli, R., Pleuger, J., Schefer, S., Ustaszewski, K. and Van Hinsbergen, D., 2016, Tectonic units of the Alpine collision zone between Eastern Alps and Western Turkey: Unpublished map.

Sinigoi, S., Quick, J. E., Demarchi, G. and Klotzli, U., 2011, The role of crustal fertility in the generation of large silicic magmatic systems triggered by intrusion of mantle magma in the deep crust: Contributions to Mineralogy and Petrology, v. 162, p. 691-707.

Shaw D. M., 1970. Trace-element fractionation during anataxis: Geochimica et Cosmochimica Acta, v. 34, p. 237-243.

Sinigoi, S., Quick, J. E., Demarchi, G. and Klotzli, U., 2016, Production of hybrid granitic magma at the advancing front of basaltic underplating: Inferences from the Sesia Magmatic System (south - western Alps, Italy): Lithos, v. 252-253, p. 109-122.

Sloman, L. E., 1989, Triassic shoshonites from the dolomites, northern Italy: Alkaline arc rocks in a strike-slip setting: Journal of Geophysical Research: Solid Earth, v. 94, no. B4, p. 4655-4666.

Stahle, V., Frenzel, G., Hess, J. C., Saupé, F., Schmidt, S. T. and Schneider, W., 2001, Permian metabasalt and Triassic alkaline dykes in the northern Ivrea zone: clues to the post-Variscan geodynamic evolution of the Southern Alps: Schweizerische Mineralogische und Petrographische Mitteilungen, v. 81, no. 1, p. 1-21.

Stampfli, G. M. and Borel, G. D., 2002, A plate tectonic model for the Paleozoic and Mesozoic constrained by dynamic plate boundaries and restored synthetic oceanic isochrones: Earth and Planetary Science Letters, v. 196, no. 1, p. 17-33.

Stampfli, G. M. and Borel, G. D., 2004, The TRANSMED transects in space and time: constraints on the paleotectonic evolution of the Mediterranean domain, in The TRANSMED Atlas: The Mediterranean region from crust to mantle, p. 53-80.

Stampfli, G. M., Borel, G. D., Marchant, R. and Mosar, J. (2002): Western Alps geological constraints on western Tethyan reconstructions: Journal of the Virtual Explorer, v. 8, p. 77.

Sun, S. and McDonough, W.F., 1989, Chemical and isotopic systematics of oceanic basalts: implication for mantle and processes, in Saunders A.D. and Norry M.J. eds., Magmatism in the Ocean Basins: Geological Society, Special Publications, v. 42, p. 313-345.

Traill, R. J. and Lachance, G.R., 1966, A practical solution to the matrix problem in X-ray analysis. II. Application to a multi-component alloy system: Canadian Spectroscopy, v. 11, p. 63-71.

Vardabasso, S., 1929, Rapporti tra attività magmatica e vicende tettoniche nella provincia petrografica di Predazzo: Studi Trentini di Scienze Naturali, v. 11.

Vardabasso, S., 1930, Carta geologica del territorio eruttivo di Predazzo e Monzoni: Ufficio Idrografico del Magistrato alle Acque di Venezia, PD, scale 1:25000, 2 sheet.

Visonà, D., 1997, The Predazzo multipulse intrusive body (Western Dolomites, Italy). Field and mineralogical studies: Memorie di Scienze Geologiche, v. 49, p. 117-125.

Zanetti, A., Mazzucchelli, M., Sinigoi, S., Giovanardi, T., Peressini, G. and Fanning, M., 2013, SHRIMP U–Pb Zircon Triassic intrusion age of the Finero mafic complex (Ivrea–Verbano zone, Western Alps) and its geodynamic implications: Journal of Petrology, v. 54, no. 11, p. 2235-2265.

Ziegler, P. A. and Stampfli, G. M., 2001, Late Palaeozoic-Early Mesozoic plate boundary reorganization: collapse of the Variscan orogen and opening of Neotethys: Natura Bresciana, v. 25, p. 17-34.

Figure Captions

Figure 1 (colour online).

(a) Distribution of the Triassic magmatism in the Alps. The tectonic units of the eastern portion of the Alps are partly modified from Dal Piaz *et al*. (2003) and Schmid *et al*. (2016). LO: Ligurian Ophiolites; AM: deformed Adriatic margin; AD: Adriatic Microplate; SA: Southern Alps; DI: Dinarides; SM: Southern margin of Meliata; HB: Eoalpine High-Pressure Belt; TW: Tauern tectonic Window; EW: Engadine tectonic Window; OTW: Ossola-Tessin tectonic Window; EA: Eastern Austroalpine; H: Helvetic domain; M: Molasse foredeep. In the Southern Alps domain the Triassic igneous bodies (see also Castellarin *et al*., 1988) are evidenced: (1) Brescian Alps (Cassinis *et al*., 2008); (2) Alto Vicentino (Bellieni *et al*., 2010); (3) Dolomitic Area; (4) Carnia region (Gianolla *et al*., 1992; Brack *et al*., 2005); (5) Karavanke, Austria (Lippolt and Pidgeon, 1976; Bellieni *et al*., 2010). (b) Distribution of

intrusives (Predazzo Intrusive Complex = PIC, Mt. Monzoni and Cima Pape), volcanics, and dike swarms in the Dolomitic Area.

Figure 2 (colour online).

Simplified geological map and cross-section of the Predazzo Intrusive Complex.

Figure 3 (colour online).

Photomicrographs and field reconstruction (modified from Google Earth) reporting the grain size gradual transition from volcanic to intrusive rocks of the Shoshonitic Silica Saturated Unit at the eastern edge of Predazzo Intrusive Complex. (a) Porphiritic trachyandesite (1850 m a.s.l., M.te Mulat) comprising large plagioclase and clinopyroxene phenocrysts embedded in a microcrystalline plagioclase + clinopyroxene + oxide groundmass (transmitted plane-polarized light). (b) Hypabissal monzonite (1900 m a.s.l., M.te Mulat) characterised by large plagioclase over a microcrystalline assemblage of quartz + K-feldspar + biotite + plagioclase + clinopyroxene + amphibole (transmitted plane-polarized light). (c, d) Holocrystalline monzo-diorite (1900 m a.s.l., M.te Mulat) composed of plagioclase + clinopyroxene + biotite + amphibole + oxides (c: transmitted plane-polarized light; d: cross polarized light).

Figure 4.

QAPF diagram showing the distribution of rocks from the Predazzo Intrusive Complex.

Figure 5.

Total alkali vs. silica (TAS) classification diagram (Le Maitre *et al*., 1989) showing whole rock compositions from the Predazzo Intrusive Complex.

Figure 6.

K_2O vs. SiO_2 classification diagram (Ewart, 1982) showing whole rock compositions from the Predazzo Intrusive Complex.

Figure 7.

K_2O vs. Na_2O classification diagram showing whole rock compositions from the Predazzo Intrusive Complex.

Figure 8.

(a, b) CaO and (c, d) FeO vs. SiO_2 variation diagrams showing whole rock compositions from the Predazzo Intrusive Complex. (a, c) Shoshonitic Silica Saturated, Granitic Unit, and Shoshonitic Silica Undersaturated suites are plotted together with the composition of the solid assemblages derived by the FC modelling. SA1SS = Gabbroic Solid Assemblage 1 with SS affinity; SA2SS = Monzo-gabbroic Solid Assemblage 2 with SS affinity; SA3SS = Monzo-dioritic Solid Assemblage 3 with SS affinity; SA1SU = Gabbroic Solid Assemblage 1 with SU affinity; SA2SU = Monzo-dioritic Solid Assemblage 2 with SU affinity. (b, d) FC vectors derived for the SS and SU suites using as starting compositions the monzo-gabbros (samples FC43B and EM10 respectively). The final compositions are syenites (samples EM110 and 11* respectively). For each step is also reported the relative percentage of the fractionating mineral phases, traslating to the compositions of the subtracted solid assemblages. Ol = olivine; Opx = orthopyroxene; Cpx = clinopyroxene; Plag = plagioclase; Ap = apatite; Mt = magnetite; Bt = biotite; K-Feld = K-feldspar; Amph = amphibole; Qz = quartz; Zirc = zircon.

Figure 9.

N-MORB-normalised trace element and REE patterns for representative Predazzo Intrusive Complex (a, b) pyroxenites, (c, d) GU, (e, f) SS and (g, h) SU rocks. Normalising values from Sun and McDonough (1989).

Figure 10.

(a, c) Rb and (b, d) Zr vs. SiO_2 variation diagrams of rocks from the Predazzo Intrusive Complex. (a, c) Shoshonitic Silica Saturated, Granitic Unit and Shoshonitic Silica Undersaturated suites. (b, d) FC vectors derived for the SS and SU suites using as starting compositions the monzo-gabbros (samples FC43B and EM10 respectively). The final compositions are syenites (samples EM110 and 11* respectively). For each step is also reported the relative percentage of the fractionating mineral phases, traslating to the compositions of the subtracted solid assemblages. Ol = olivine; Opx = orthopyroxene; Cpx = clinopyroxene; Plag = plagioclase; Ap = apatite; Mt = magnetite; Bt = biotite; K-Feld = K-feldspar; Amph = amphibole; Qz = quartz; Zirc = zircon.

Figure 11.

(a) Pyroxene, (b) magnetite, and (c) feldspar classification diagrams.

Figure 12.

(a) Al_2O_3 vs. SiO_2 and (b) K_2O vs. SiO_2 diagrams for Shoshonitic Silica Saturated and Shoshonitic Silica Undersaturated amphiboles. (c) Al_2O_3 vs. SiO_2 and (d) FeO vs. SiO_2 diagrams for Shoshonitic Silica Saturated, Shoshonitic Silica Undersaturated and Granitic Unit biotites. Field labels are based on amphibole and biotite classification from Leake *et al.* (1997) and Dymek (1983), respectively.

Figure 13.

Total alkali vs. silica (TAS) classification diagram (Le Maitre *et al.*, 1989) illustrating the fractional crystallization modelling of selected rock samples from the Predazzo Intrusive Complex, as well as the compositions of the cumulate assemblages calculated from the model

compared to the natural cumulate lithotypes. SA1SS = Gabbroic Solid Assemblage 1 with SS affinity; SA2SS = Monzo-gabbroic Solid Assemblage 2 with SS affinity; SA3SS = Monzo-dioritic Solid Assemblage 3 with SS affinity; SA1SU = Gabbroic Solid Assemblage 1 with SU affinity; SA2SU = Monzo-dioritic Solid Assemblage 2 with SU affinity.

Figure 14.

Interpretative sketch of the evolutionary sequence of rocks from the Predazzo Intrusive Complex. The first pulse at t1 (a) is characterised by Shoshonitic Silica Saturated affinity; the second pulse at t2 (b) is represented by the intrusion of the Granitic Unit granites and syenogranites; the final pulse at t3 (c), outcropping in the eastern part of the complex, is constituted by Shoshonitic Silica Undersaturated terms. t2 (237 Ma) is from Mundil *et al.* (1996). The cumulitic gabbros and pyroxenites are also shown at the border of the Shoshonitic Silica Saturated intrusion.

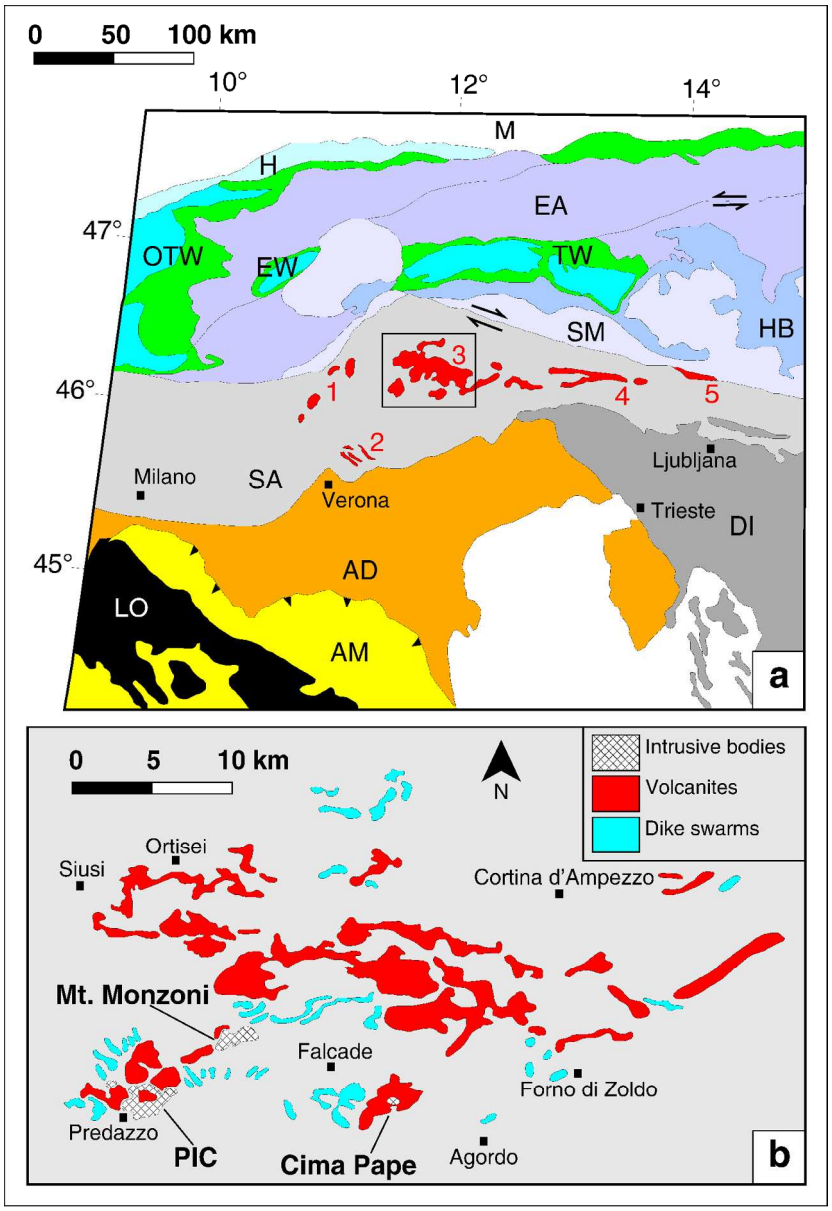

Figure 1 (colour online).
(a) Distribution of the Triassic magmatism in the Alps. The tectonic units of the eastern portion of the Alps are partly modified from Dal Piaz et al. (2003) and Schmid et al. (2016). LO: Ligurian Ophiolites; AM: deformed Adriatic margin; AD: Adriatic Microplate; SA: Southern Alps; DI: Dinarides; SM: Southern margin of Meliata; HB: Eoalpine High-Pressure Belt; TW: Tauern tectonic Window; EW: Engadine tectonic Window; OTW: Ossola-Tessin tectonic Window; EA: Eastern Austroalpine; H: Helvetic domain; M: Molasse foredeep. In the Southern Alps domain the Triassic igneous bodies (see also Castellarin et al., 1988) are evidenced: (1) Brescian Alps (Cassinis et al., 2008); (2) Alto Vicentino (Bellieni et al., 2010); (3) Dolomitic Area; (4) Carnia region (Gianolla et al., 1992; Brack et al., 2005); (5) Karavanke, Austria (Lippolt and Pidgeon, 1976; Bellieni et al., 2010). (b) Distribution of intrusives (Predazzo Intrusive Complex = PIC, Mt. Monzoni and Cima Pape), volcanics, and dike swarms in the Dolomitic Area.

205x299mm (200 x 200 DPI)

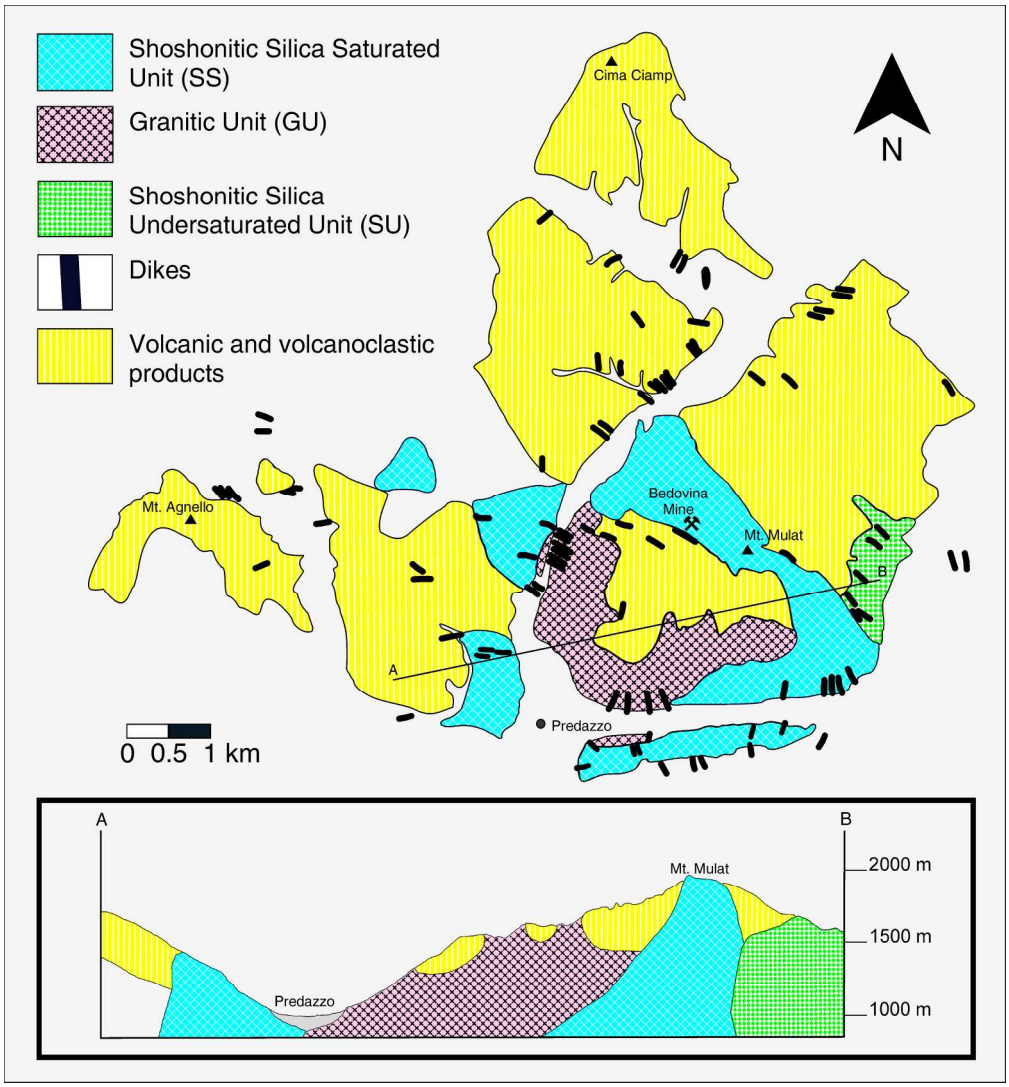

Figure 2 (colour online).
Simplified geological map and cross-section of the Predazzo Intrusive Complex.

212x228mm (300 x 300 DPI)

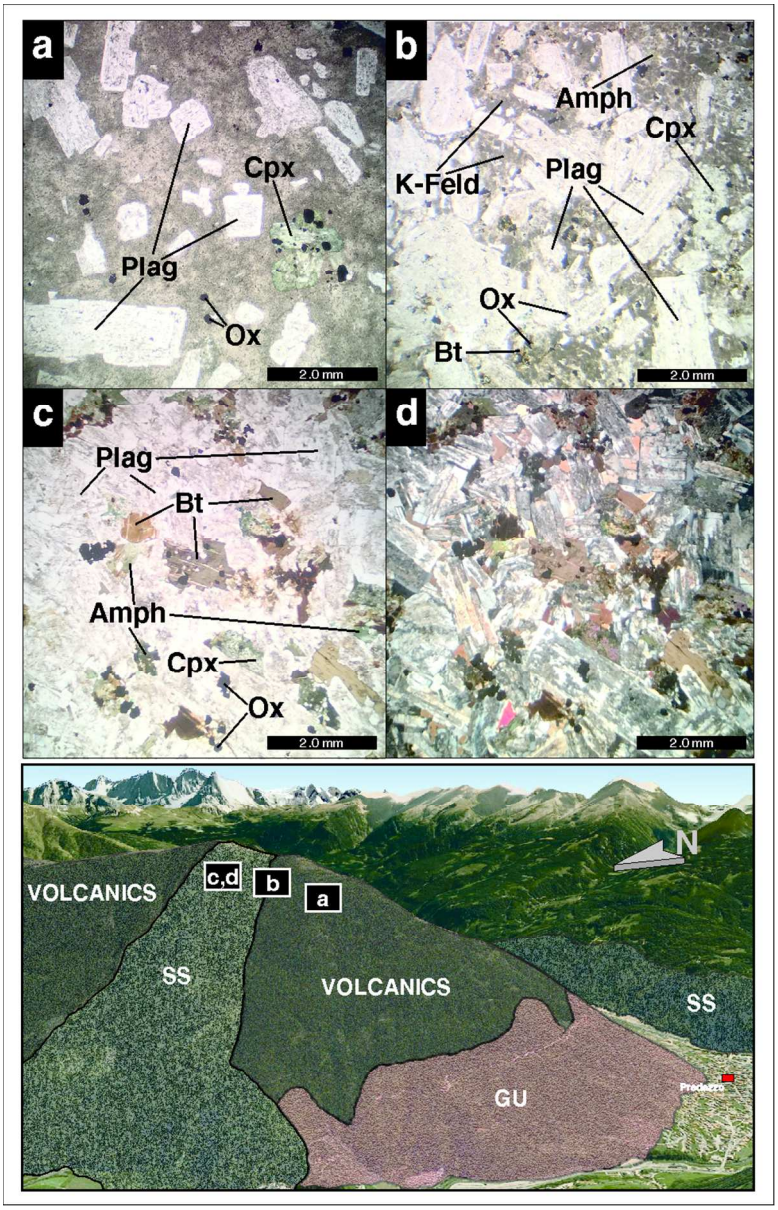

Figure 3 (colour online).
Photomicrographs and field reconstruction (modified from Google Earth) reporting the grain size gradual transition from volcanic to intrusive rocks of the Shoshonitic Silica Saturated Unit at the eastern edge of Predazzo Intrusive Complex. (a) Porphiritic trachyandesite (1850 m a.s.l., M.te Mulat) comprising large plagioclase and clinopyroxene phenocrysts embedded in a microcrystalline plagioclase + clinopyroxene + oxide groundmass (transmitted plane-polarized light). (b) Hypabissal monzonite (1900 m a.s.l., M.te Mulat) characterised by large plagioclase over a microcrystalline assemblage of quartz + K-feldspar + biotite + plagioclase + clinopyroxene + amphibole (transmitted plane-polarized light). (c, d) Holocrystalline monzo-diorite (1900 m a.s.l., M.te Mulat) composed of plagioclase + clinopyroxene + biotite + amphibole + oxides (c: transmitted plane-polarized light; d: cross polarized light).

246x383mm (100 x 100 DPI)

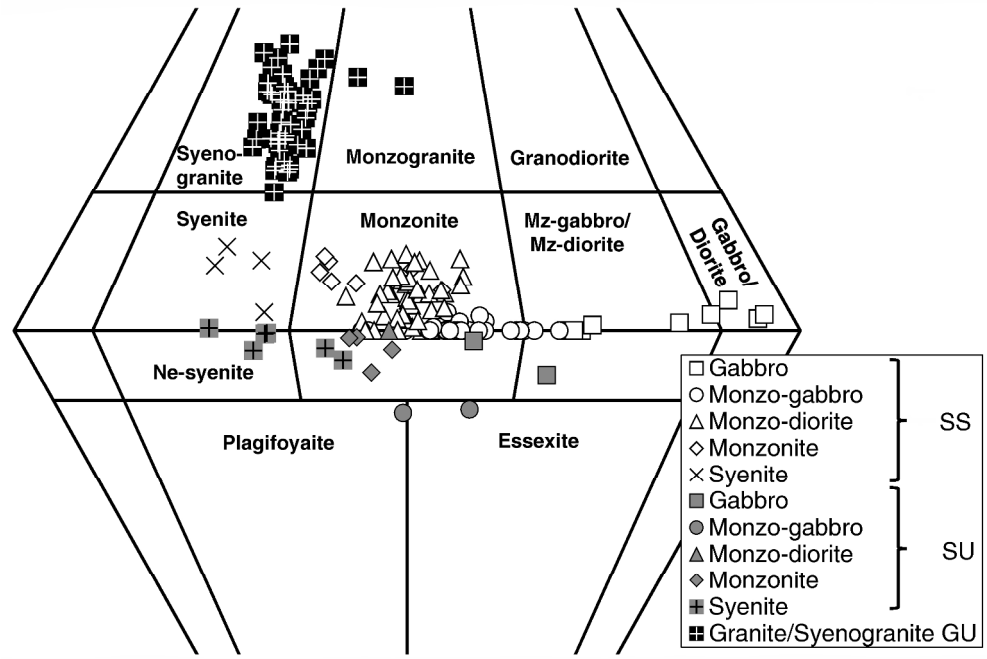

Figure 4.
QAPF diagram showing the distribution of rocks from the Predazzo Intrusive Complex.

265x178mm (300 x 300 DPI)

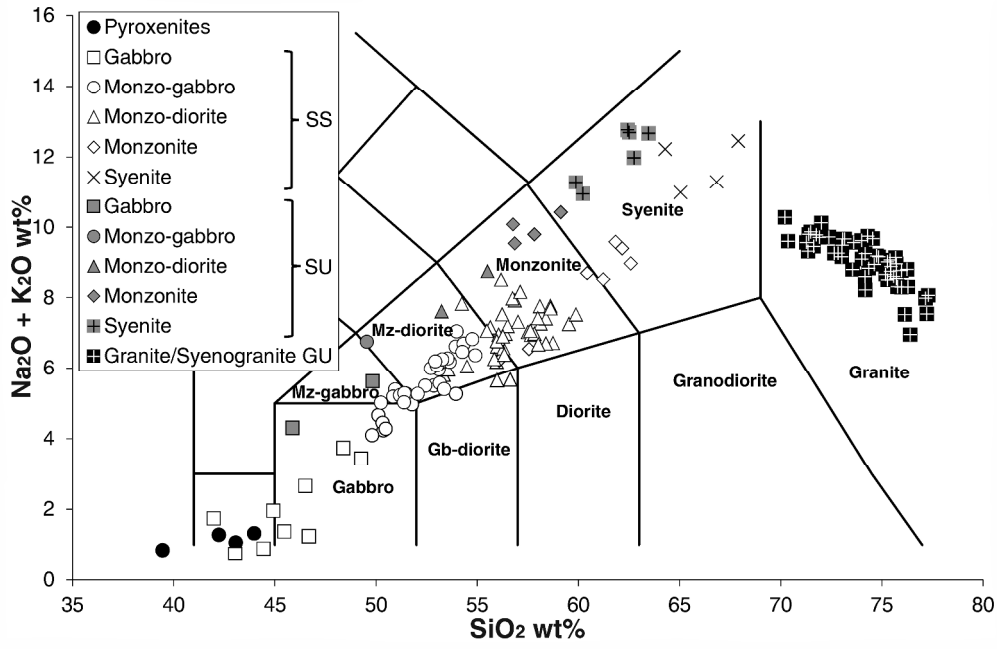

Figure 5.
Total alkali vs. silica (TAS) classification diagram (Le Maitre et al., 1989) showing whole rock compositions from the Predazzo Intrusive Complex.

347x227mm (300 x 300 DPI)

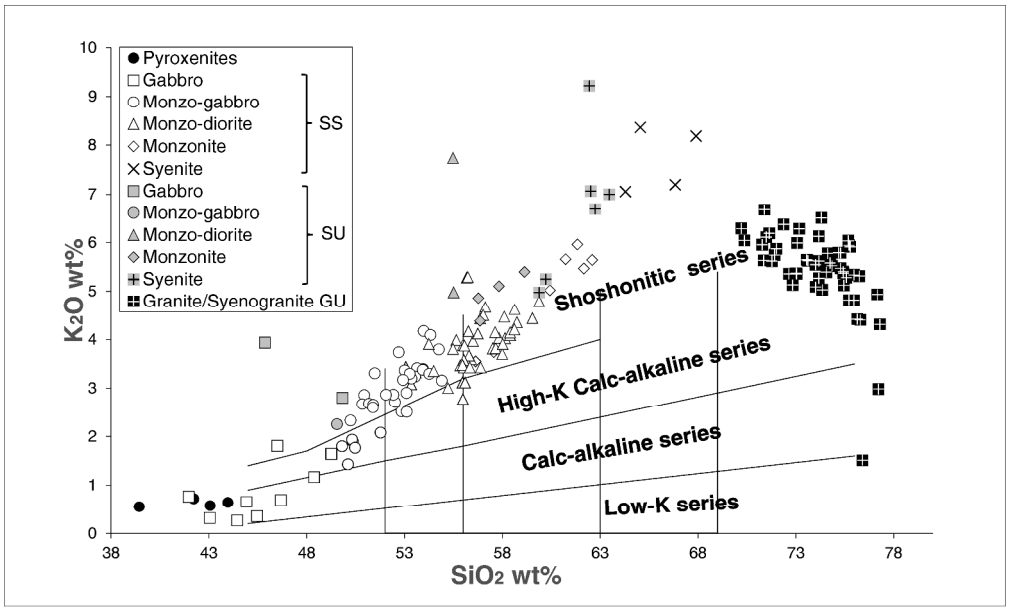

Figure 6.
K2O vs. SiO2 classification diagram (Ewart, 1982) showing whole rock compositions from the Predazzo Intrusive Complex.

487x292mm (200 x 200 DPI)

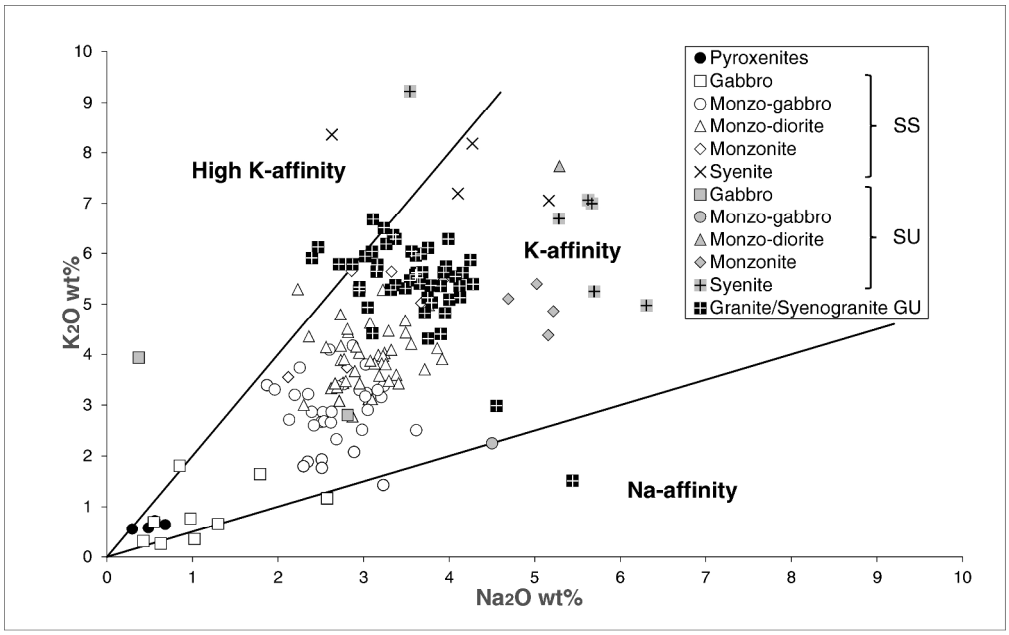

Figure 7.
K2O vs. Na2O classification diagram showing whole rock compositions from the Predazzo Intrusive Complex.

467x292mm (200 x 200 DPI)

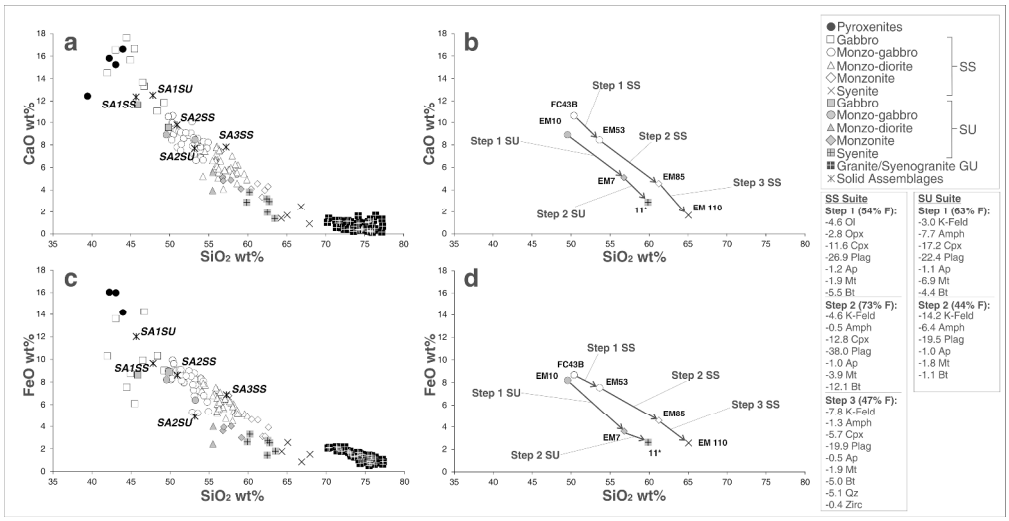

Figure 8.
(a, b) CaO and (c, d) FeO vs. SiO2 variation diagrams showing whole rock compositions from the Predazzo Intrusive Complex. (a, c) Shoshonitic Silica Saturated, Granitic Unit, and Shoshonitic Silica Undersaturated suites are plotted together with the composition of the solid assemblages derived by the FC modelling. SA1SS = Gabbroic Solid Assemblage 1 with SS affinity; SA2SS = Monzo-gabbroic Solid Assemblage 2 with SS affinity; SA3SS = Monzo-dioritic Solid Assemblage 3 with SS affinity; SA1SU = Gabbroic Solid Assemblage 1 with SU affinity; SA2SU = Monzo-dioritic Solid Assemblage 2 with SU affinity. (b, d) FC vectors derived for the SS and SU suites using as starting compositions the monzo-gabbros (samples FC43B and EM10 respectively). The final compositions are syenites (samples EM110 and 11* respectively). For each step is also reported the relative percentage of the fractionating mineral phases, traslating to the compositions of the subtracted solid assemblages. Ol = olivine; Opx = orthopyroxene; Cpx = clinopyroxene; Plag = plagioclase; Ap = apatite; Mt = magnetite; Bt = biotite; K-Feld = K-feldspar; Amph = amphibole; Qz = quartz; Zirc = zircon.

845x432mm (150 x 150 DPI)

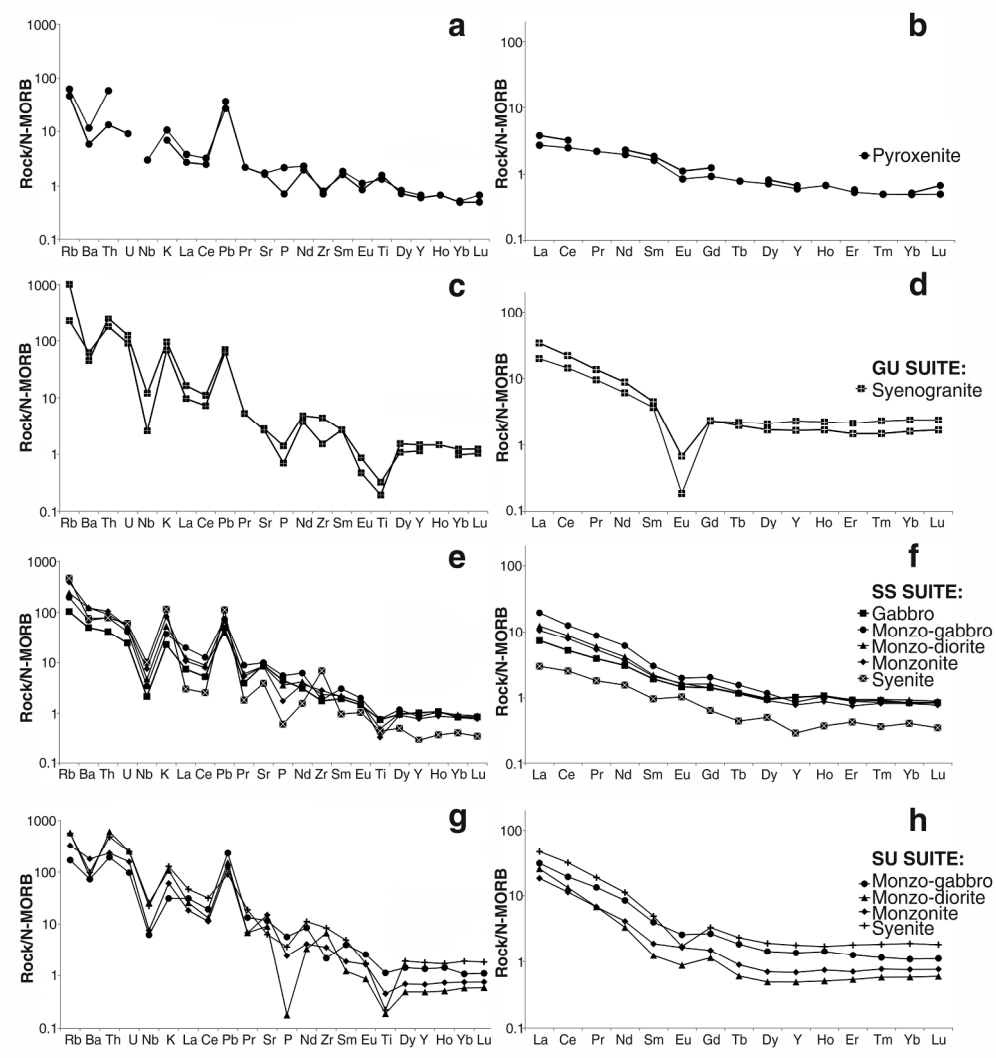

Figure 9.
N-MORB-normalised trace element and REE patterns for representative Predazzo Intrusive Complex (a, b) pyroxenites, (c, d) GU, (e, f) SS and (g, h) SU rocks. Normalising values from Sun and McDonough (1989).

661x702mm (100 x 100 DPI)

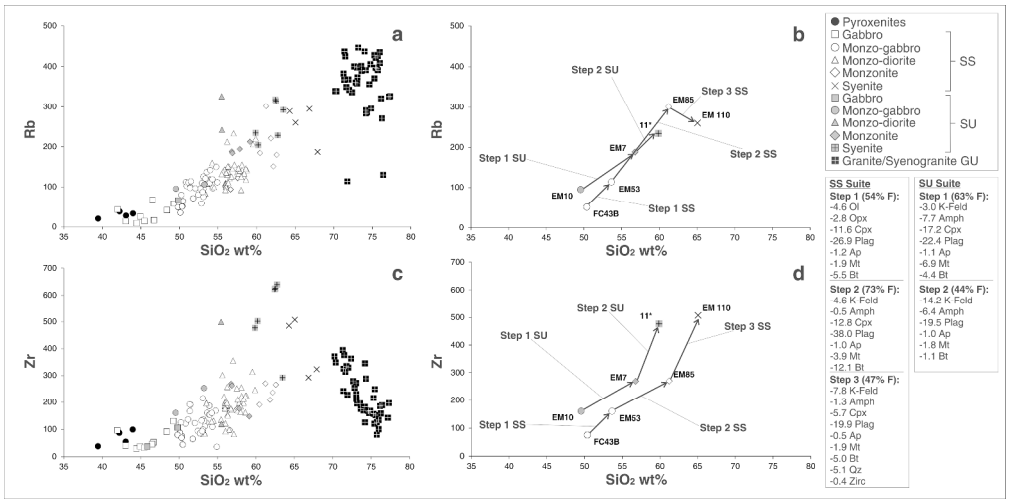

Figure 10.
(a, c) Rb and (b, d) Zr vs. SiO2 variation diagrams of rocks from the Predazzo Intrusive Complex. (a, c) Shoshonitic Silica Saturated, Granitic Unit and Shoshonitic Silica Undersaturated suites. (b, d) FC vectors derived for the SS and SU suites using as starting compositions the monzo-gabbros (samples FC43B and EM10 respectively). The final compositions are syenites (samples EM110 and 11* respectively). For each step is also reported the relative percentage of the fractionating mineral phases, traslating to the compositions of the subtracted solid assemblages. Ol = olivine; Opx = orthopyroxene; Cpx = clinopyroxene; Plag = plagioclase; Ap = apatite; Mt = magnetite; Bt = biotite; K-Feld = K-feldspar; Amph = amphibole; Qz = quartz; Zirc = zircon.

874x430mm (150 x 150 DPI)

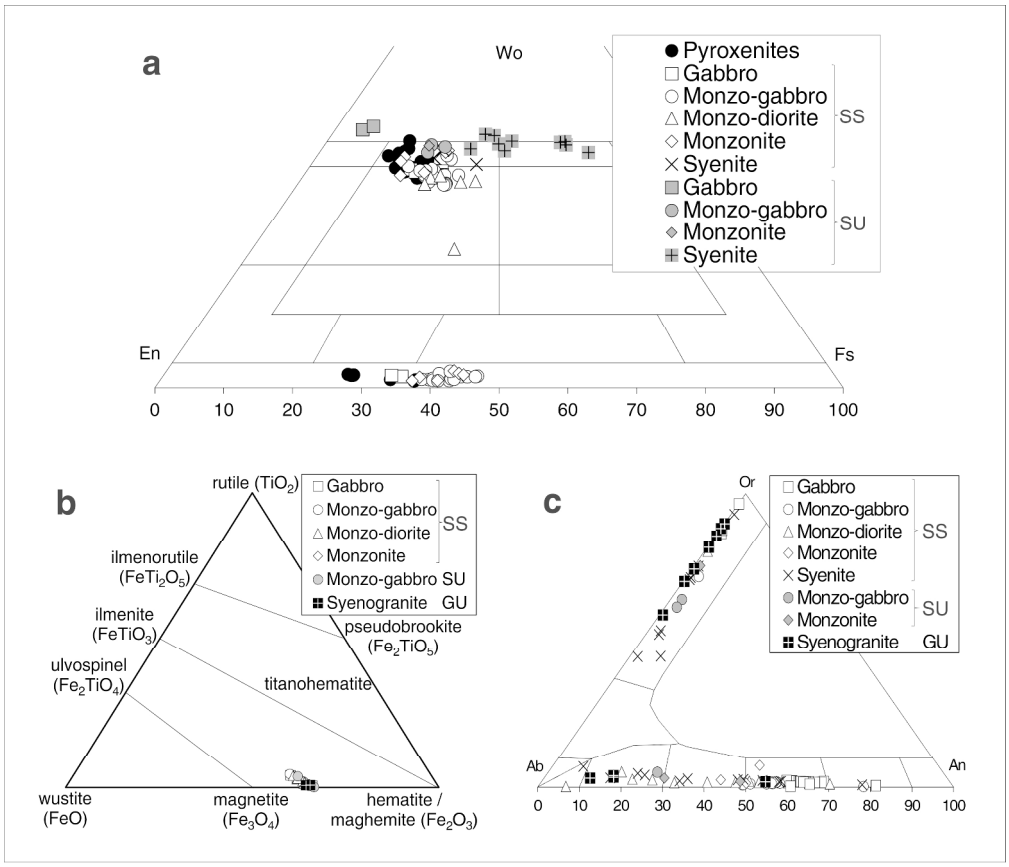

Figure 11.
(a) Pyroxene, (b) magnetite, and (c) feldspar classification diagrams.

513x439mm (150 x 150 DPI)

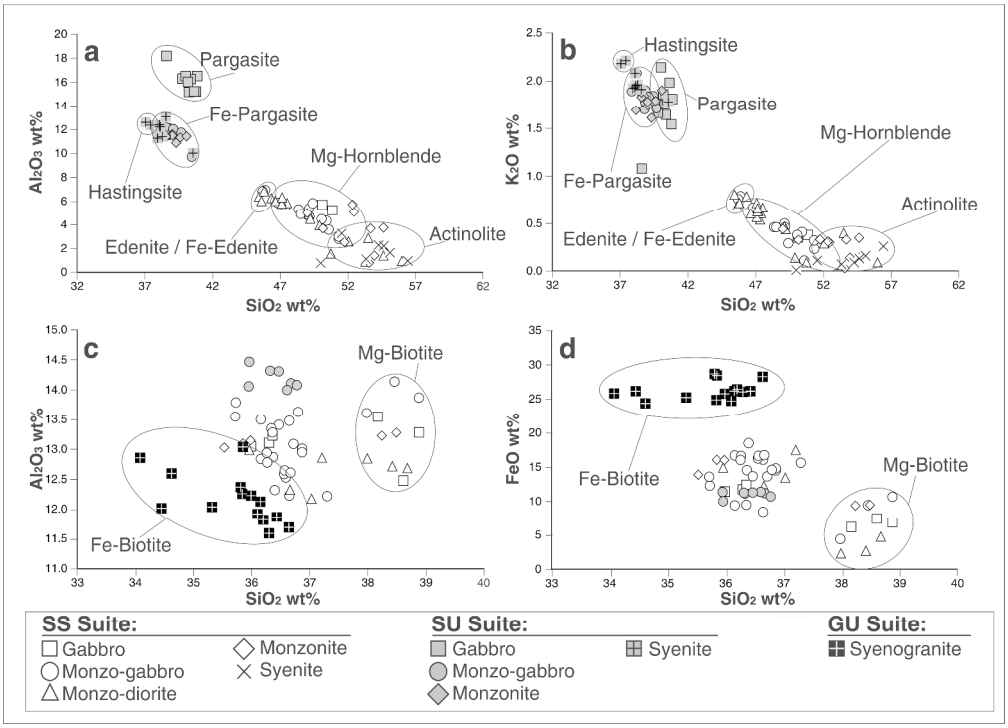

Figure 12.
(a) Al2O3 vs. SiO2 and (b) K2O vs. SiO2 diagrams for Shoshonitic Silica Saturated and Shoshonitic Silica Undersaturated amphiboles. (c) Al2O3 vs. SiO2 and (d) FeO vs. SiO2 diagrams for Shoshonitic Silica Saturated, Shoshonitic Silica Undersaturated and Granitic Unit biotites. Field labels are based on amphibole and biotite classification from Leake et al. (1997) and Dymek (1983), respectively.

372x267mm (300 x 300 DPI)

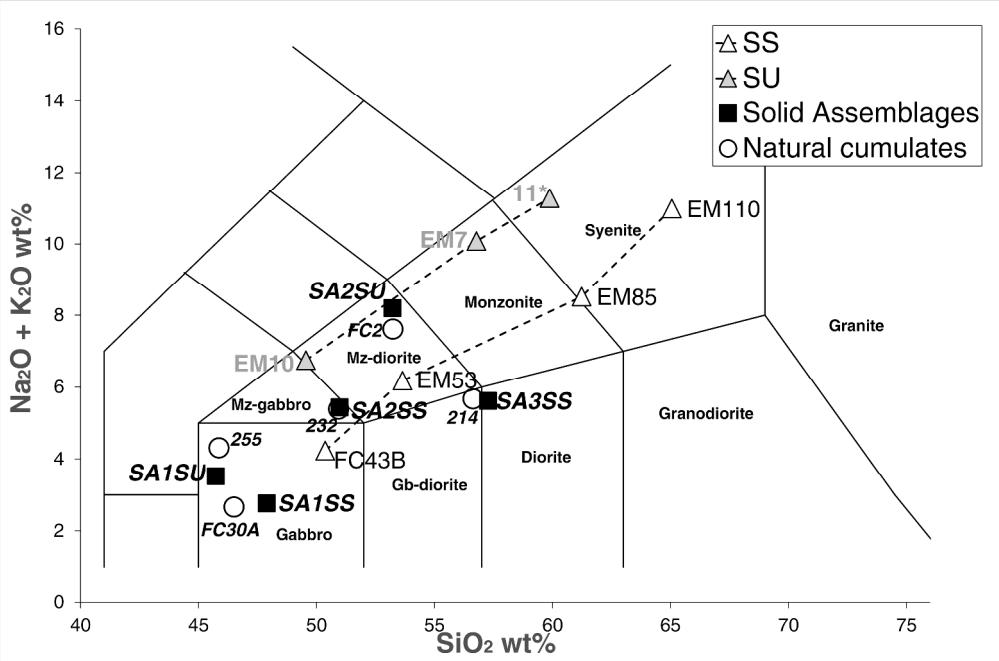

Figure 13.
Total alkali vs. silica (TAS) classification diagram (Le Maitre et al., 1989) illustrating the fractional crystallization modelling of selected rock samples from the Predazzo Intrusive Complex, as well as the compositions of the cumulate assemblages calculated from the model compared to the natural cumulate lithotypes. SA1SS = Gabbroic Solid Assemblage 1 with SS affinity; SA2SS = Monzo-gabbroic Solid Assemblage 2 with SS affinity; SA3SS = Monzo-dioritic Solid Assemblage 3 with SS affinity; SA1SU = Gabbroic Solid Assemblage 1 with SU affinity; SA2SU = Monzo-dioritic Solid Assemblage 2 with SU affinity.

448x297mm (300 x 300 DPI)

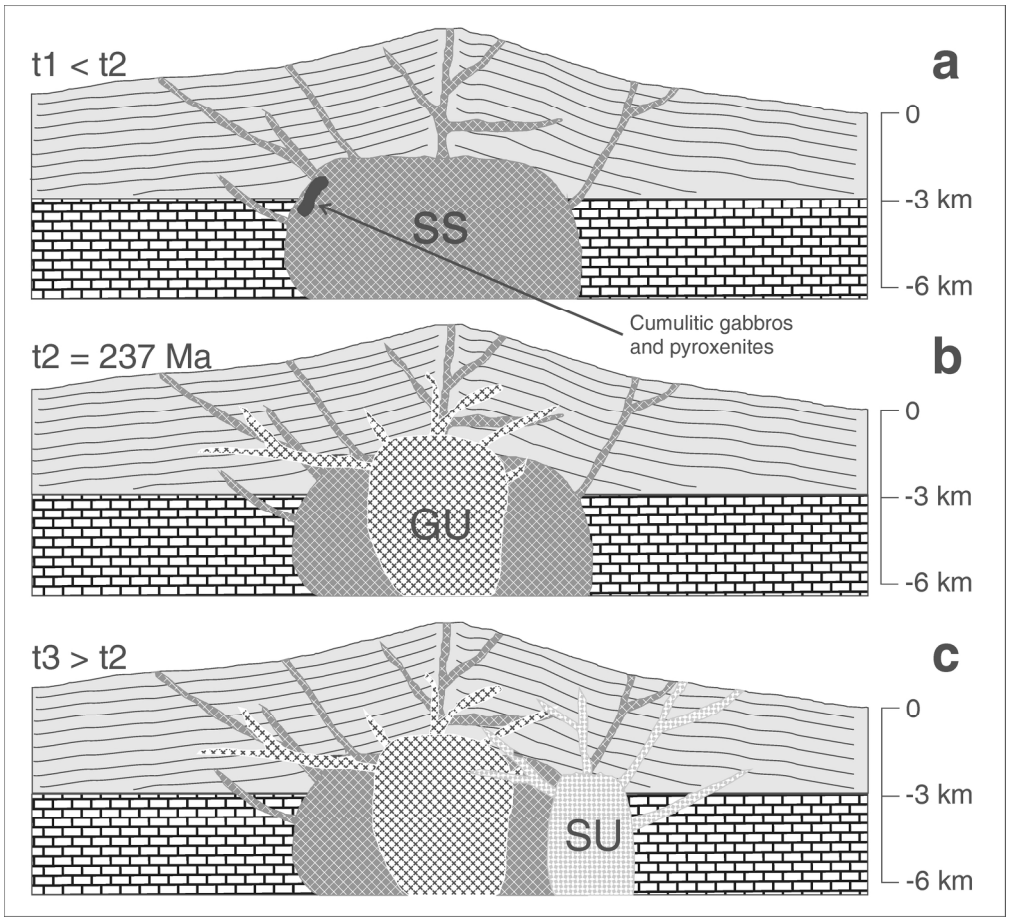

Figure 14.
Interpretative sketch of the evolutionary sequence of rocks from the Predazzo Intrusive Complex. The first pulse at t1 (a) is characterised by Shoshonitic Silica Saturated affinity; the second pulse at t2 (b) is represented by the intrusion of the Granitic Unit granites and syenogranites; the final pulse at t3 (c), outcropping in the eastern part of the complex, is constituted by Shoshonitic Silica Undersaturated terms. t2 (237 Ma) is from Mundil et al. (1996). The cumulitic gabbros and pyroxenites are also shown at the border of the Shoshonitic Silica Saturated intrusion.

189x172mm (300 x 300 DPI)

Table 1: Age, magma type and tectonic setting of the main Triassic magmatic occurrences in the Alps

Locality	Age (Ma)	Dating	Magma Type	Tectonic Setting	References
Mt. Muffetto, Brescian Alps (Italy)	231 ± 5	Ar/Ar	Alkaline - Calc-alkaline	Arc/back-arc	Armienti *et al*., 2003
S. Giovanni Bianco, Brescian Alps (Italy)	217 ± 3	Ar/Ar	Tholeiitic - Transitional	Extensional rifting	Cassinis *et al*., 2008
Alto Vicentino (Italy)	232 ± 2	Rb/Sr	Alkaline - Calc-alkaline	Arc/back-arc	Borsi, unpublished data
Dolomitic Area (Italy)	237.3 ± 1	U/Pb	Alkaline - Calc-alkaline	Arc/back-arc	Mundil *et al*., 1996
Carnia region (Italy)	Ladinian	-	Alkaline	Arc/back-arc	Gianolla, 1992
Karavanke ragion (Austria)	230 ± 9	U/Pb	Alkaline	Within Plate	Lippolt and Pidgeon, 1974

Supplementary Table 1: Major, trace elements analysis and normative (CIPW) calculation of SS lithotypes.

SAMPLE	FC50	FC30A	FC43B	MA9	MA10	EM53	A95	FC36	A40	FC37	EM79	EM85	EM64	EM110	JB2	
LITHOLOGY	Gb	Gb	Mz-Gb	Mz-Gb	Mz-Gb	Mz-Gb	Mz-Dr	Mz-Dr	Mz-Dr	Mz-Dr	Mz	Mz	Sy	Sy	Int. Std.	Det. Lim.
SiO_2	41.92	45.30	49.82	51.70	53.27	53.13	55.40	53.93	55.00	55.89	60.79	60.39	67.24	64.06	52.94	0.05
TiO_2	1.46	1.07	1.08	0.77	0.79	0.83	0.68	0.93	0.62	0.81	0.42	0.69	0.17	0.56	1.16	0.01
Al_2O_3	11.05	16.03	16.38	16.01	14.59	17.27	19.38	15.45	19.07	16.50	19.48	16.81	16.38	17.18	15.56	0.05
Fe_2O_3	1.99	1.45	1.29	0.99	1.00	1.12	0.80	1.15	0.89	0.94	0.46	0.68	0.22	0.38	13.92*	0.10
FeO	13.24	9.66	8.59	6.60	6.68	7.49	5.36	7.67	5.95	6.28	3.06	4.53	1.50	2.53	-	-
MnO	0.21	0.16	0.22	0.17	0.17	0.16	0.16	0.18	0.14	0.18	0.07	0.11	0.07	0.05	0.21	0.05
MgO	10.62	7.77	6.08	6.54	6.42	4.08	3.04	5.81	3.19	4.14	1.12	2.26	0.22	1.18	3.33	0.01
CaO	16.12	13.31	10.50	8.22	8.14	8.36	4.99	7.36	6.01	6.52	3.28	4.49	0.89	1.64	9.68	0.04
Na_2O	0.42	0.83	2.32	3.52	2.55	2.74	3.18	2.66	3.02	3.19	3.56	2.82	4.23	2.59	2.42	0.01
K_2O	0.30	1.76	1.87	2.44	4.01	3.38	5.21	3.32	3.80	3.93	5.86	5.58	8.10	8.23	0.42	0.01
P_2O_5	0.04	0.06	0.76	0.38	0.42	0.48	0.40	0.49	0.41	0.52	0.20	0.26	0.00	0.07	0.07	0.01
LOI	2.62	2.60	1.09	2.67	1.96	0.95	1.40	1.05	1.90	1.10	1.72	1.37	0.99	1.54	0.31	-
tot	100	100	100	100	100	100	100	100	100	100	100	100	100	100	100	-
mg#	58.75	58.83	55.68	63.77	63.06	46.11	47.11	57.35	45.73	53.90	36.56	43.95	18.47	42.37	-	-
Quartz	0.00	0.00	0.00	0.00	0.00	0.00	0.00	0.31	2.34	1.49	7.52	8.32	8.98	10.97	-	-
Plagioclase	28.10	42.18	48.94	51.83	38.85	48.49	49.83	43.39	53.82	46.62	46.14	41.14	37.94	30.19	-	-
Orthoclase	0.00	10.64	11.17	14.83	24.17	20.15	31.20	19.80	22.87	23.46	35.22	33.45	48.34	49.40	-	-
Nepheline	1.97	0.42	0.00	0.00	0.00	0.00	0.00	0.00	0.00	0.00	0.00	0.00	0.00	0.00	-	-
Leucite	1.44	0.00	0.00	0.00	0.00	0.00	0.00	0.00	0.00	0.00	0.00	0.00	0.00	0.00	-	-
Diopside	40.87	26.05	15.58	15.02	17.80	11.55	0.00	10.97	0.08	8.50	0.00	3.42	2.37	0.00	-	-
Hypersthene	0.00	0.00	12.34	0.06	7.44	13.41	12.73	20.51	17.07	15.48	7.28	10.46	1.61	6.29	-	-
Olivine	19.73	15.79	5.81	14.05	7.40	1.65	2.12	0.00	0.00	0.00	0.00	0.00	0.00	0.00	-	-
Ilmenite	2.85	2.09	2.07	1.50	1.54	1.60	1.31	1.79	1.20	1.54	0.82	1.33	0.32	1.08	-	-
Magnetite	3.73	2.73	2.38	1.86	1.87	2.07	1.49	2.13	1.67	1.74	0.86	1.26	0.42	0.71	-	-
Apatite	0.09	0.14	1.78	0.90	1.00	1.11	0.95	1.16	0.97	1.23	0.46	0.60	0.00	0.16	-	-
Zircon	0.01	0.01	0	0.01	0.01	0.03	0.04	0.03	0.03	0.01	0.04	0.06	0.06	0.10	-	-
Pb	23	10	16	11	15	24	20	18	12	25	21	26	23	34	11	1
Ni	31	30	4	14	22	17	9	12	9	5	6	16	5	6	17	2
Co	51	53	40	41	41	34	21	37	20	27	9	14	6	8	40	2
Cr	75	79	21	87	158	34	15	38	15	10	9	33	5	9	64	2
V	821	565	238	284	256	188	111	210	109	163	32	89	15	34	536	2
Rb	14	67	51	75	97	114	212	99	135	122	221	301	187	260	8	1
Sr	390	513	1140	780	704	801	468	749	760	837	755	554	284	350	172	2
Ba	67	189	275	464	607	504	690	531	775	536	772	530	553	481	236	3
Nb	6	5	9	9	10	8	14	13	11	13	18	31	24	24	4	1
Zr	41	46	75	98	109	160	188	131	175	98	208	270	323	507	48	2
Hf	6	7	6	6	7	-	4	9	4	9	2	2	5	2	1	1
U	-	-	-	-	-	-	2	-	2	-	2	4	4	3	-	1
Th	2	2	3	0	0	12	9	6	11	8	13	21	27	9	1	1
Y	10	11	14	14	16	28	24	18	29	19	22	24	25	8	25	2
La	19	14	16	54	57	14	26	24	31	26	27	32	24	8	-	5
Ce	22	11	39	0	0	60	69	52	66	54	59	70	57	19	10	8

mg# = 100 * Mg/[Mg + Fe^{2+}]

Gb: gabbro; Mz-Gb: monzo-gabbro; Mz-Dr: monzo-diorite; Mz: monzonite; Sy: syenite

Int. Std.: International Standard JB2; Det. Lim.: Detection Limits from Allahyari *et al.* (2014)

*** Total iron expressed as Fe_2O_3**

Supplementary Table 2: Major, trace elements analysis and normative (CIPW) calculation of pyroxenites.

SAMPLE	FC31B	EM13	EM23	373	JB2	
LITHOLOGY	Px	Px	Px	Px	Int. Std.	Det. Lim.
SiO_2	39.45	42.22	43.84	42.58	52.94	0.05
TiO_2	2.22	1.51	1.36	1.56	1.16	0.01
Al_2O_3	7.02	7.04	5.78	6.56	15.56	0.05
Fe_2O_3	3.18	2.40	2.12	8.07	13.92*	0.10
FeO	21.21	16.01	14.14	10.66	-	-
MnO	0.21	0.22	0.20	0.21	0.21	0.05
MgO	13.39	13.19	14.02	13.58	3.33	0.01
CaO	12.44	15.80	16.57	15.07	9.68	0.04
Na_2O	0.30	0.56	0.68	0.48	2.42	0.01
K_2O	0.55	0.72	0.64	0.57	0.42	0.01
P_2O_5	0.03	0.30	0.34	0.10	0.07	0.01
LOI	0.00	0.03	0.31	0.57	0.31	-
tot	100	100	100	100	100	-
mg#	52.85	56.40	60.89	57.45	-	-
Quartz	0.00	0.00	0.00	0.00	-	-
Plagioclase	16.18	14.57	10.86	14.18	-	-
Orthoclase	0.00	0.00	0.00	0.00	-	-
Nepheline	1.38	2.57	3.12	2.25	-	-
Leucite	2.55	3.34	2.97	2.69	-	-
Diopside	32.56	41.92	51.04	46.59	-	-
Hypersthene	0.00	0.00	0.00	0.00	-	-
Olivine	35.43	26.37	22.69	25.54	-	-
Ilmenite	4.22	2.87	2.58	3.00	-	-
Magnetite	5.81	4.39	3.89	4.38	-	-
Apatite	0.07	0.70	0.79	0.23	-	-
Zircon	0.01	0.01	0.01	0.01	-	-
Chromite	0.03	0.01	0.04	0.01	-	-
Pb	8	9	8	-	11	1
Ni	60	53	66	56	17	2
Co	108	83	77	84	40	2
Cr	130	69	214	84	64	2
V	1419	770	656	730	536	2
Rb	20	38	33	28	8	1
Sr	122	172	108	176	172	2
Ba	131	153	134	105	236	3
Nb	6	2	3	17	4	1
Zr	38	87	99	55	48	2
Th	3	6	4	-	1	1
Y	8	14	13	11	25	2
La	9	0	4	0	-	5
Ce	16	18	29	13	10	8

mg# = 100 * Mg/[Mg + Fe^{2+}]

Px: pyroxenite

Int. Std.: International Standard JB2; Det. Lim.: Detection Limits from Allahyari *et al.* (2014)

*** Total iron expressed as Fe_2O_3**

Supplementary Table 3: Major, trace elements analysis and normative (CIPW) calculation of GU lithotypes.

SAMPLE	EM22	EM90B	EM94	2*	EM59	EM84	EM1	EM131	JB2	
LITHOLOGY	Gr	Gr	Sy-Gr	Sy-Gr	Sy-Gr	Sy-Gr	Sy-Gr	Sy-Gr	Int. Std.	Det. Lim.
SiO_2	75.98	75.24	70.65	72.42	71.06	74.06	75.38	70.86	52.94	0.05
TiO_2	0.02	0.04	0.24	0.09	0.14	0.06	0.06	0.23	1.16	0.01
Al_2O_3	12.53	13.58	15.19	14.18	16.27	13.94	13.01	14.50	15.56	0.05
Fe_2O_3	0.10	0.11	0.31	0.44	0.27	0.17	0.16	0.27	13.92*	0.1
FeO	0.64	0.73	2.07	1.14	1.81	1.12	1.08	1.78	-	-
MnO	0.03	0.02	0.04	0.06	0.04	0.01	0.02	0.04	0.21	0.05
MgO	0.37	0.28	0.22	0.05	0.15	0.00	0.00	0.24	3.33	0.01
CaO	1.30	1.62	0.55	1.05	0.56	0.36	0.82	0.52	9.68	0.04
Na_2O	4.48	5.36	3.08	3.34	3.67	4.25	3.92	4.18	2.42	0.01
K_2O	2.94	1.49	6.61	6.22	5.61	5.36	4.78	5.78	0.42	0.01
P_2O_5	0.00	0.00	0.00	0.01	0.00	0.00	0.00	0.01	0.07	0.01
LOI	1.61	1.53	1.04	0.99	0.41	0.67	0.76	1.57	0.31	-
tot	100	100	100	100	100	100	100	100	100	-
mg#	47.64	37.50	14.41	5.48	11.68	0.00	0.00	17.69	-	-
Quartz	35.64	34.46	24.76	26.19	25.61	27.41	32.05	22.10	-	-
Plagioclase	43.98	54.24	29.12	33.73	34.03	38.00	37.23	38.55	-	-
Orthoclase	17.67	8.92	39.48	37.11	33.27	31.91	28.48	34.69	-	-
Corundum	0.00	0.20	1.98	0.08	3.15	0.49	0.00	0.43	-	-
Diopside	0.89	0.00	0.00	0.00	0.00	0.00	0.28	0.00	-	-
Hypersthene	1.59	1.88	3.60	2.30	3.15	1.75	1.54	3.23	-	-
Ilmenite	0.04	0.08	0.46	0.17	0.27	0.11	0.11	0.44	-	-
Magnetite	0.17	0.20	0.58	0.38	0.49	0.30	0.30	0.49	-	-
Apatite	0.00	0.00	0.00	0.02	0.00	0.00	0.00	0.02	-	-
Zircon	0.03	0.04	0.06	0.04	0.04	0.03	0.01	0.06	-	-
Pb	6	0	26	19	15	9	16	17	11	1
Ni	8	4	7	8	8	7	8	2	17	2
Co	-	-	5	3	1	3	1	3	40	2
Cr	6	5	7	13	5	8	8	3	64	2
V	-	13	6	-	6	-	-	8	536	2
Rb	239	130	437	446	367	436	435	342	8	1
Sr	33	109	109	22	64	14	16	97	172	2
Ba	71	121	107	61	89	38	51	62	236	3
Nb	93	26	48	43	41	57	31	44	4	1
Zr	152	188	325	194	242	165	100	329	48	2
Th	47	64	49	-	63	60	57	41	1	1
Y	83	51	37	86	55	42	20	39	25	2
La	-	6	88	51	106	13	38	51	-	5
Ce	23	20	131	93	150	42	65	97	10	8

mg# = 100 * Mg/[Mg + Fe^{2+}]

Gr: granite; Sy-Gr: syenogranite

Int. Std.: International Standard JB2; Det. Lim.: Detection Limits from Allahyari *et al.* (2014)

*** Total iron expressed as Fe_2O_3**

Supplementary Table 4: Major, trace elements analysis and normative (CIPW) calculation of SU lithotypes.

SAMPLE	255	EM15	EM10	FC2	EM7	EM6	138	359	EM3	EM4	EM5	11*	JB2	
LITHOLOGY	Gb	Gb	Mz-Gb	Mz-Dr	Mz	Mz	Mz	Mz	Sy	Sy	Sy	Sy	Int. Std.	Det. Lim.
SiO_2	44.30	49.23	48.66	52.40	55.71	56.22	58.04	56.97	63.04	61.58	59.85	58.11	52.94	0.05
TiO_2	0.84	0.92	1.11	1.14	0.58	0.57	0.50	0.66	0.26	0.34	0.46	0.37	1.16	0.01
Al_2O_3	20.29	17.69	18.40	16.04	21.01	21.46	20.46	19.88	19.52	18.64	19.46	21.12	15.56	0.05
Fe_2O_3	4.39	1.32	1.21	0.95	0.53	0.58	1.68	2.25	0.27	0.40	0.49	0.97	13.92*	0.10
FeO	5.51	8.80	8.06	6.31	3.55	3.90	1.84	2.48	1.79	2.70	3.29	2.02	-	-
MnO	0.15	0.18	0.47	0.40	0.23	0.19	0.18	0.17	0.10	0.14	0.16	0.29	0.21	0.05
MgO	5.96	4.91	3.97	5.03	1.36	1.48	1.08	1.44	0.39	0.28	0.83	0.41	3.33	0.01
CaO	11.22	9.44	8.74	8.34	5.01	4.76	4.01	4.81	1.37	1.92	3.78	2.81	9.68	0.04
Na_2O	0.36	2.78	4.42	5.02	5.12	5.10	4.93	4.62	5.63	5.54	5.66	6.12	2.42	0.01
K_2O	3.80	2.77	2.21	2.47	4.77	4.33	5.30	5.03	6.95	6.96	5.22	4.83	0.42	0.01
P_2O_5	0.07	0.75	0.65	0.32	0.25	0.28	0.25	0.37	0.00	0.00	0.18	0.06	0.07	0.01
LOI	3.11	1.21	2.11	1.58	1.87	1.13	1.71	1.32	0.69	1.49	0.60	2.89	0.31	-
tot	100	100	100	100	100	100	100	100	100	100	100	100	100	-
mg#	55.94	46.36	43.60	58.62	37.49	40.25	39.37	39.18	25.56	15.55	28.45	22.21	-	-
Quartz	0.00	0.00	0.00	0.00	0.00	0.00	0.00	0.00	0.00	0.00	0.00	0.00	-	-
Plagioclase	44.03	49.89	47.96	43.04	54.97	61.55	59.07	57.05	54.41	48.20	56.35	60.29	-	-
Orthoclase	19.83	16.55	13.30	14.83	28.72	25.88	31.91	30.20	41.37	41.78	31.03	29.43	-	-
Nepheline	1.70	1.00	7.79	7.72	5.33	2.48	0.97	0.84	0.33	2.64	2.26	3.94	-	-
Leucite	2.66	0.00	0.00	0.00	0.00	0.00	0.00	0.00	0.00	0.00	0.00	0.00	-	-
Diopside	10.93	12.32	13.23	21.36	2.90	0.00	0.81	2.89	0.00	3.74	4.71	0.00	-	-
Hypersthene	0.00	0.00	0.00	0.00	0.00	0.00	0.00	0.00	0.00	0.00	0.00	0.00	-	-
Olivine	16.69	14.35	11.28	8.37	5.43	7.06	4.97	5.89	2.74	2.17	3.43	3.95	-	-
Ilmenite	1.65	1.77	2.73	2.20	1.12	1.10	0.97	1.27	0.49	0.66	0.87	0.72	-	-
Magnetite	2.36	2.44	2.25	1.75	0.99	1.09	0.83	1.10	0.49	0.75	0.91	0.72	-	-
Apatite	0.16	1.76	1.53	0.76	0.58	0.65	0.58	0.88	0.00	0.00	0.42	0.14	-	-
Zircon	0.00	0.01	0.03	0.04	0.06	0.06	0.03	0.03	0.06	0.12	0.10	0.09	-	-
Pb	4	13	69	42	88	37	74	33	40	36	28	52	11	1
Ni	31	15	14	28	7	5	4	4	6	8	8	9	17	2
Co	42	40	21	29	9	9	7	8	4	3	7	3	40	2
Cr	113	23	11	80	10	3	5	4	6	5	5	25	64	2
V	374	239	217	208	66	80	64	86	29	42	67	29	536	2
Rb	216	66	95	106	188	184	212	194	292	314	204	234	8	1
Sr	425	1247	1054	845	1194	1351	1468	1390	624	406	800	325	172	2
Ba	236	782	459	498	853	1129	1123	982	546	351	498	329	236	3
Nb	13	3	15	37	26	18	19	15	26	39	28	29	4	1
Zr	37	106	160	253	269	262	147	175	292	625	502	477	48	2
U	-	-	5	-	-	-	-	-	5	-	-	-	-	1
Th	-	5	24	13	44	40	-	-	27	89	54	-	1	1
Y	8	24	38	44	31	26	23	25	12	36	42	46	25	2
La	0	22	78	99	113	106	72	71	25	102	120	102	-	5
Ce	10	64	145	173	171	128	110	113	54	141	178	182	10	8

mg# = 100 * Mg/[Mg + Fe^{2+}]

Gb: gabbro; Mz-Gb: monzo-gabbro; Mz-Dr: monzo-diorite; Mz: monzonite; Sy: syenite

Int. Std.: International Standard JB2; Det. Lim.: Detection Limits from Allahyari *et al.* (2014)

*** Total iron expressed as Fe_2O_3**

Supplementary Table 5: REE analysis of representative SS, SU and GU lithotypes.

AFFINITY	SS							SU					GU				
SAMPLE	A4	A9	EM111	EM113	EM95	EM79	EM64	EM10	EM9	EM6	EM107	EM3	EM22	EM31	EM84	JB2	
LITHOLOGY	Gb	Mz-Gb	Mz-Gb	Mz-Dr	Mz-Dr	Mz	Sy	Mz-Gb	Mz-Dr	Mz	Sy	Sy	Gr	Sy-Gr	Sy-Gr	Int. Std.	Det. Lim.
La	18.5	29.3	27.0	39.3	60.0	26.6	24.3	77.6	63.9	45.9	117	24.5	1.56	9.75	1.63	2.32	0.051
Ce	39.4	64.0	57.6	82.7	73.5	59.5	56.8	145	100	85.1	237	54.4	4.94	33.6	7.31	6.36	0.051
Pr	5.20	8.97	7.32	9.83	9.81	7.10	6.96	17.6	9.0	8.95	24.9	5.56	0.80	2.51	0.49	1.13	0.009
Nd	22.6	28.2	31.2	37.5	37.7	27.2	27.1	62.1	24.3	30.1	81.8	23.1	4.37	9.21	1.80	6.43	0.023
Sm	5.08	5.94	6.23	7.08	7.52	5.60	5.34	10.5	3.24	4.94	12.9	4.11	2.22	1.55	0.46	2.27	0.004
Eu	1.50	1.86	1.72	1.72	1.52	1.70	1.07	2.63	0.89	1.68	1.75	1.30	0.03	0.09	0.01	0.82	0.05
Gd	5.27	6.17	5.94	6.29	6.90	5.20	4.74	9.81	4.18	5.46	12.2	3.87	2.42	1.44	0.50	2.76	0.007
Tb	0.79	0.92	0.94	0.85	0.92	0.78	0.76	1.24	0.41	0.60	1.55	0.39	0.63	0.21	0.11	0.60	0.057
Dy	4.33	4.89	4.97	4.68	5.06	4.16	4.35	6.49	2.24	3.18	8.67	2.77	4.40	1.08	0.72	3.83	0.002
Y	28.7	28.1	27.9	27.8	29.7	21.9	24.5	37.9	13.7	19.2	49.9	11.7	33.0	4.96	4.09	24.18	0.02
Ho	1.09	1.13	1.01	0.89	0.90	0.89	0.92	1.44	0.52	0.75	1.72	0.45	1.08	0.23	0.17	0.86	0.046
Er	2.75	2.63	2.71	2.54	2.67	2.25	2.57	3.73	1.59	2.09	5.34	1.56	3.68	0.73	0.54	2.49	0.005
Tm	0.42	0.39	0.43	0.37	0.35	0.38	0.44	0.52	0.26	0.35	0.84	0.21	0.76	0.13	0.10	0.42	0.017
Yb	2.57	2.15	2.80	2.44	2.54	2.51	3.08	3.30	1.78	2.30	5.78	1.60	5.50	0.89	0.67	2.59	0.01
Lu	0.39	0.35	0.45	0.37	0.35	0.35	0.47	0.51	0.27	0.35	0.83	0.21	0.83	0.14	0.10	0.40	0.012

Gb: gabbro; Mz-Gb: monzo-gabbro; Mz-Dr: monzo-diorite; Mz: monzonite; Sy: syenite; Gr: granite; Sy-Gr: syenogranite

Int. Std.: International Standard JB2; Det. Lim.: Detection Limits from Allahyari *et al.* (2014)

Supplementary Table 6: Representative analysis of olivine (Ol) and magnetite (Mt) from SS, SU and GU lithotypes.

AFFINITY	SS				SS							SU		GU
MINERAL	Ol	Ol	Ol	Ol	Mt	Mt	Mt	Mt	Mt	Mt	Mt	Mt	Mt	Mt
SAMPLE	P 91-80	P 91-67	P 92-51	P 92-51	P 91-123	P91-80	P 91-3	P 92-14	P 92-12	P 91-145	P91-73	P91-17	P91-17	P 91-49
LITHOLOGY	Gb	Gb	Gb	Gb	Gb	Gb	Mz-Gb	Mz-Gb	Mz-Dr	Mz-Dr	Mz	Mz-Gb	Mz-Gb	Sy-Gr
SiO_2	35.13	32.83	36.23	35.89	0.00	0.00	0.00	0.00	0.00	0.00	0.00	0.00	0.00	0.00
TiO_2	0.01	0.26	0.05	0.02	4.19	0.52	0.90	4.66	4.11	1.11	0.07	0.09	3.78	0.63
Al_2O_3	0.00	0.46	0.00	0.00	1.80	0.68	0.49	0.27	0.14	2.24	0.26	0.14	0.04	3.83
Fe_2O_3	0.00	0.00	0.00	0.00	59.09	66.78	66.17	58.58	60.15	57.54	67.43	67.82	60.31	52.52
FeO	37.88	48.42	32.37	33.13	34.51	30.69	31.44	34.34	33.94	29.23	30.49	30.69	32.35	24.77
MnO	0.95	0.62	1.69	1.69	0.17	0.20	0.04	0.53	0.54	0.23	0.10	0.04	1.59	2.68
MgO	24.99	17.07	29.77	28.83	0.41	0.32	0.18	0.07	0.05	0.00	0.03	0.05	0.03	0.00
CaO	0.04	0.22	0.05	0.03	0.00	0.00	0.00	0.00	0.00	0.00	0.00	0.00	0.00	0.00
Cr_2O_3	0.02	0.00	0.00	0.00	0.04	0.01	0.14	0.15	0.04	0.00	0.00	0.10	0.11	0.04
tot	99.02	99.88	100.16	99.59	100.21	99.20	99.36	98.60	98.97	90.35	98.38	98.93	98.21	84.47
mg#	54.04	38.58	62.11	60.80										
Si	1.00	0.98	1.00	1.00	0.00	0.00	0.00	0.00	0.00	0.00	0.00	0.00	0.00	0.00
Ti	0.00	0.01	0.00	0.00	0.12	0.02	0.03	0.14	0.12	0.04	0.00	0.00	0.11	0.02
Al	0.00	0.02	0.00	0.00	0.08	0.03	0.02	0.01	0.01	0.11	0.01	0.01	0.00	0.20
Fe^{3+}	0.00	0.00	0.00	0.00	1.68	1.94	1.92	1.71	1.75	1.82	1.98	1.99	1.77	1.76
Fe^{2+}	0.90	1.21	0.74	0.77	1.09	0.99	1.02	1.12	1.10	1.03	1.00	1.00	1.06	0.92
Mn	0.02	0.02	0.04	0.04	0.01	0.01	0.00	0.02	0.02	0.01	0.00	0.00	0.05	0.10
Mg	1.06	0.76	1.22	1.19	0.02	0.02	0.01	0.00	0.00	0.00	0.00	0.00	0.00	0.00
Ca	0.00	0.01	0.00	0.00	0.00	0.00	0.00	0.00	0.00	0.00	0.00	0.00	0.00	0.00
Cr	0.00	0.00	0.00	0.00	0.00	0.00	0.00	0.01	0.00	0.00	0.00	0.00	0.00	0.00
Fo	54.04	38.58	62.11	60.80										
Fa	45.96	61.42	37.89	39.20										

mg# = 100 * Mg/[Mg + Fe^{2+}]

Gb: gabbro; Mz-Gb: monzo-gabbro; Mz-Dr: monzo-diorite; Mz: monzonite; Sy-Gr: syenogranite

Fo: forsterite; Fa: fayalite

Supplementary Table 7: Representative analysis of pyroxene from SS and SU lithotypes.

AFFINITY	SS						SU				
MINERAL	Cpx	Opx	Cpx	Cpx	Cpx	Cpx	Cpx	Cpx	Cpx	Cpx	Cpx
SAMPLE	P 91-58	P 91-123	P91-113	A 95	EM 85	P 91-10	P93-7	P91-17	EM 9	P93-10	P 96-4
LITHOLOGY	Gb	Gb	Mz-Gb	Mz-Dr	Mz	Sy	Gb	Mz-Gb	Mz-Dr	Mz	Sy
SiO_2	51.13	54.65	50.10	52.21	53.31	53.49	50.11	51.46	45.32	53.48	45.76
TiO_2	0.34	0.25	0.55	0.14	0.15	0.05	0.84	0.64	1.89	0.10	1.14
Al_2O_3	1.78	1.08	3.06	0.72	0.91	0.72	6.58	2.73	7.54	0.96	4.91
Fe_2O_3	0.85	0.14	0.57	0.55	0.00	0.25	0.49	0.58	1.79	0.30	1.58
FeO	8.86	17.53	10.13	10.17	17.70	10.13	2.70	8.45	10.37	8.25	16.73
MnO	0.52	0.52	0.39	0.85	0.43	0.61	0.11	0.37	0.64	0.95	1.50
MgO	14.16	25.94	12.97	11.94	13.39	11.81	14.53	11.88	8.32	12.41	4.90
CaO	21.64	1.30	21.41	23.54	12.43	23.39	25.74	23.22	22.73	23.84	21.62
Na_2O	0.30	0.00	0.19	0.34	0.24	0.63	0.07	0.85	1.22	0.64	1.15
K_2O	0.00	0.00	0.00	0.00	0.06	0.00	0.00	0.00	0.03	0.00	0.00
Cr_2O_3	0.00	0.00	0.00	0.07	0.00	0.06	0.04	0.00	0.00	0.03	0.05
tot	99.58	101.41	99.37	100.53	98.62	101.14	101.21	100.18	99.85	100.96	99.34
mg#	74.04	72.48	69.49	67.68	59.66	67.53	90.52	71.46	58.88	72.79	34.33
Si	1.91	1.96	1.89	1.96	2.09	1.99	1.81	1.92	1.72	1.98	1.80
Ti	0.01	0.01	0.02	0.00	0.00	0.00	0.02	0.02	0.05	0.00	0.03
Al	0.08	0.05	0.14	0.03	0.04	0.03	0.28	0.12	0.34	0.04	0.23
Fe^{3+}	0.02	0.00	0.02	0.02	0.00	0.01	0.01	0.02	0.05	0.01	0.05
Fe^{2+}	0.28	0.53	0.32	0.32	0.53	0.32	0.08	0.26	0.33	0.26	0.55
Mn	0.02	0.02	0.01	0.03	0.01	0.02	0.00	0.01	0.02	0.03	0.05
Mg	0.79	1.39	0.73	0.67	0.78	0.66	0.78	0.66	0.47	0.69	0.29
Ca	0.87	0.05	0.87	0.95	0.52	0.93	1.00	0.93	0.93	0.95	0.91
Na	0.02	0.00	0.01	0.03	0.02	0.05	0.01	0.06	0.09	0.05	0.09
K	0.00	0.00	0.00	0.00	0.00	0.00	0.00	0.00	0.00	0.00	0.00
Cr	0.00	0.00	0.00	0.00	0.00	0.00	0.00	0.00	0.00	0.00	0.00
Wo	43.95	2.52	44.57	47.90	28.25	48.37	53.09	49.34	51.47	49.17	49.35
En	40.00	69.92	37.52	33.79	42.35	33.96	41.69	35.14	26.21	35.57	15.58
Fs	16.05	27.56	17.91	18.31	29.39	17.68	5.22	15.52	22.31	15.26	35.06

mg# = 100 * Mg/[Mg + Fe^{2+}]

Gb: gabbro; Mz-Gb: monzo-gabbro; Mz-Dr: monzo-diorite; Mz: monzonite; Sy: syenite

Wo: wollastonite; En: enstatite; Fs: ferrosilite

Supplementary Table 8: Representative analysis of amphibole (Amph) from SS and SU lithotypes.

AFFINITY	SS								SU			
SAMPLE	P 91-123	P 91-3	EM111	A95	P 91-145	EM85	P 91-73	EM64	P 93-7	EM10	EM9	P 91-22
LITHOLOGY	Gb	Mz-Gb	Mz-Gb	Mz-Dr	Mz-Dr	Mz	Mz	Sy	Gb	Mz-Gb	Mz-Dr	Sy
SiO_2	50.12	49.15	51.35	49.01	56.00	53.31	54.62	50.00	38.61	37.87	37.06	38.09
TiO_2	1.21	0.47	0.55	0.65	0.14	0.15	0.12	0.13	0.52	2.51	2.84	3.08
Al_2O_3	5.71	5.39	2.80	5.02	0.95	0.91	0.80	0.77	18.19	11.87	12.61	12.39
Fe_2O_3	2.31	2.79	3.02	1.04	1.17	0.35	0.18	0.00	1.17	0.03	0.00	0.02
FeO	8.85	15.30	14.98	15.98	10.05	15.83	13.23	12.17	7.48	16.71	20.33	17.75
MnO	0.12	0.37	0.38	0.69	0.96	0.43	0.71	1.58	0.41	0.60	1.18	1.13
MgO	16.79	12.27	13.20	11.96	16.77	13.39	15.05	11.27	13.65	9.08	6.05	7.73
CaO	11.79	10.82	10.80	11.91	11.85	12.43	12.75	21.67	12.79	11.88	11.71	11.37
Na_2O	0.96	1.03	0.60	1.03	0.28	0.24	0.08	0.45	2.54	2.26	2.20	2.27
K_2O	0.35	0.50	0.23	0.44	0.09	0.06	0.03	0.01	1.08	1.89	2.18	1.93
Cr_2O_3	0.00	0.04	0.00	0.01	0.00	0.00	0.00	0.01	0.00	0.01	0.01	0.00
NiO	0.00	0.00	0.00	0.00	0.00	0.00	0.00	0.00	0.00	0.00	0.00	0.00
tot	98.21	98.13	97.91	97.75	98.26	97.11	97.57	98.06	96.44	94.71	96.17	95.76
mg#	77.17	58.84	61.08	57.16	74.82	60.13	66.97	62.28	76.49	49.21	34.65	43.69
Si	7.08	7.15	7.43	7.24	7.89	7.85	7.90	7.49	5.69	6.02	5.93	6.01
Ti	0.13	0.05	0.06	0.07	0.02	0.02	0.01	0.02	0.06	0.30	0.34	0.37
Al	0.95	0.92	0.48	0.88	0.16	0.16	0.14	0.14	3.16	2.22	2.38	2.31
Fe^{3+}	0.25	0.31	0.33	0.12	0.12	0.04	0.02	0.00	0.13	0.00	0.00	0.00
Fe^{2+}	1.05	1.86	1.81	1.97	1.18	1.95	1.60	1.52	0.92	2.22	2.72	2.34
Mn	0.01	0.05	0.05	0.09	0.12	0.05	0.09	0.20	0.05	0.08	0.16	0.15
Mg	3.54	2.66	2.85	2.63	3.52	2.94	3.24	2.52	3.00	2.15	1.44	1.82
Ca	1.79	1.69	1.67	1.89	1.79	1.96	1.98	3.48	2.02	2.02	2.01	1.92
Na	0.26	0.29	0.17	0.30	0.08	0.07	0.02	0.13	0.73	0.70	0.68	0.70
K	0.06	0.09	0.04	0.08	0.02	0.01	0.01	0.00	0.20	0.38	0.45	0.39
Cr	0.00	0.01	0.00	0.00	0.00	0.00	0.00	0.00	0.00	0.00	0.00	0.00
Ni	0.00	0.00	0.00	0.00	0.00	0.00	0.00	0.00	0.00	0.00	0.00	0.00

mg# = 100 * Mg/[Mg + Fe^{2+}]

Gb: gabbro; Mz-Gb: monzo-gabbro; Mz-Dr: monzo-diorite; Mz: monzonite; Sy: syenite

Supplementary Table 9: Representative analysis of biotite (Bt) from SS, SU and GU lithotypes.

AFFINITY	SS					SU	GU	
SAMPLE	P 91-67	P 92-14	P 91-145	P91-38A	P 91-72	P 91-17	P 91-44	P 91-44
LITHOLOGY	Gb	Mz-Gb	Mz-Dr	Mz	Mz	Mz-Gb	Sy-Gr	Sy-Gr
SiO_2	38.88	36.47	38.68	35.98	38.24	35.95	34.08	35.85
TiO_2	0.94	4.33	4.96	3.61	3.57	4.27	0.62	1.11
Al_2O_3	13.87	13.41	12.69	13.15	13.23	14.06	12.86	13.04
Fe_2O_3	2.52	6.90	7.03	8.24	6.28	6.51	5.89	1.77
FeO	10.64	13.65	4.76	16.02	9.37	11.35	25.83	28.45
MnO	0.08	0.22	0.17	0.29	0.57	0.45	0.44	0.40
MgO	18.17	11.34	16.98	10.03	15.23	12.40	6.65	6.21
CaO	0.05	0.00	0.00	0.03	0.08	0.00	0.07	0.04
Na_2O	0.13	0.20	0.17	0.02	0.07	0.40	0.04	0.12
K_2O	9.20	8.91	9.07	8.65	8.94	8.80	8.52	8.94
Cr_2O_3	0.05	0.00	0.00	0.00	0.00	0.06	0.01	0.03
tot	94.53	95.43	94.51	96.02	95.58	94.25	95.01	95.96
mg#	75.27	59.69	86.40	52.74	74.33	66.07	31.45	28.01
Si	2.88	2.76	2.83	2.75	2.82	2.73	2.76	2.86
Ti	0.05	0.25	0.27	0.21	0.20	0.24	0.04	0.07
Al	1.21	1.20	1.09	1.18	1.15	1.26	1.23	1.23
Fe^{3+}	0.14	0.39	0.39	0.47	0.35	0.37	0.36	0.11
Fe^{2+}	0.66	0.86	0.29	1.02	0.58	0.72	1.75	1.90
Mg	2.00	1.28	1.85	1.14	1.67	1.40	0.80	0.74
Mn	0.01	0.01	0.01	0.02	0.04	0.03	0.03	0.03
Ca	0.00	0.00	0.00	0.00	0.01	0.00	0.01	0.00
Na	0.02	0.03	0.02	0.00	0.01	0.06	0.01	0.02
K	0.87	0.86	0.85	0.84	0.84	0.85	0.88	0.91
Cr	0.00	0.00	0.00	0.00	0.00	0.00	0.00	0.00

mg# = 100 * Mg/[Mg + Fe^{2+}]

Gb: gabbro; Mz-Gb: monzo-gabbro; Mz-Dr: monzo-diorite; Mz: monzonite; Sy-Gr: syenogranite

Supplementary Table 10: Representative analysis of feldspars from SS, SU and GU lithotypes.

AFFINITY	SS										SU				GU	
SAMPLE	P 91-58	P 91-58	P91-80	P 92-14	P 92-14	P91-145	P91-145	P91-38A	P 93-6	P 93-6	P91-17	P91-17	P91-18	P91-18	P91-24	P91-24
CORE/RIM	core	rim		core	rim	core	rim									
LITHOLOGY	Gb	Gb	Gb	Mz-Gb	Mz-Gb	Mz-Dr	Mz-Dr	Mz	Sy	Sy	Mz-Gb	Mz-Gb	Mz	Mz	Sy-Gr	Sy-Gr
SiO_2	50.39	53.96	66.61	54.66	56.84	50.30	55.34	58.59	66.61	61.06	66.43	62.78	66.39	57.19	65.69	66.38
TiO_2	0.00	0.04	0.00	0.06	0.02	0.04	0.00	0.01	0.00	0.04	0.04	0.06	0.06	0.03	0.00	0.01
Al_2O_3	30.66	28.58	17.91	28.81	27.81	30.74	27.34	27.68	19.09	25.22	19.35	24.31	18.99	27.81	21.87	18.44
Fe_2O_3	0.54	0.59	0.09	0.47	0.41	0.44	0.42	0.50	0.12	0.28	0.20	0.22	0.12	0.24	0.30	0.07
MnO	0.02	0.06	0.03	0.06	0.00	0.01	0.01	0.02	0.08	0.03	0.04	0.00	0.00	0.01	0.08	0.02
MgO	0.06	0.05	0.00	0.01	0.02	0.08	0.00	0.12	0.00	0.00	0.00	0.03	0.00	0.00	0.01	0.00
CaO	14.52	12.78	0.02	11.56	10.19	15.07	10.25	7.73	0.25	7.06	0.58	5.74	0.22	9.71	3.15	0.02
Na_2O	3.58	4.43	0.33	4.70	5.80	3.49	6.25	3.69	3.02	7.65	4.08	8.30	2.68	5.66	8.54	1.13
K_2O	0.34	0.36	14.59	0.28	0.13	0.19	0.30	0.97	11.49	0.37	10.57	0.93	12.40	0.33	0.63	15.14
Cr_2O_3	0.00	0.01	0.00	0.03	0.01	0.00	0.00	0.00	0.05	0.00	0.02	0.00	0.01	0.00	0.01	0.04
tot	100.11	100.86	99.58	100.64	101.23	100.36	99.91	99.31	100.71	101.71	101.31	102.37	100.87	100.98	100.28	101.25
Si	2.29	2.43	3.11	2.46	2.53	2.28	2.48	2.70	3.02	2.68	2.97	2.72	3.01	2.55	2.92	3.02
Ti	0.00	0.00	0.00	0.00	0.00	0.00	0.00	0.00	0.00	0.00	0.00	0.00	0.00	0.00	0.00	0.00
Al	1.64	1.52	0.99	1.53	1.46	1.64	1.45	1.50	1.02	1.30	1.02	1.24	1.02	1.46	1.15	0.99
Fe^{3+}	0.02	0.02	0.00	0.02	0.01	0.02	0.02	0.02	0.00	0.01	0.01	0.01	0.00	0.01	0.01	0.00
Mn	0.00	0.00	0.00	0.00	0.00	0.00	0.00	0.00	0.00	0.00	0.00	0.00	0.00	0.00	0.00	0.00
Mg	0.00	0.00	0.00	0.00	0.00	0.01	0.00	0.01	0.00	0.00	0.00	0.00	0.00	0.00	0.00	0.00
Ca	0.71	0.62	0.00	0.56	0.49	0.73	0.49	0.38	0.01	0.33	0.03	0.27	0.01	0.46	0.15	0.00
Na	0.32	0.39	0.03	0.41	0.50	0.31	0.54	0.33	0.27	0.65	0.35	0.70	0.24	0.49	0.74	0.10
K	0.02	0.02	0.87	0.02	0.01	0.01	0.02	0.06	0.67	0.02	0.60	0.05	0.72	0.02	0.04	0.88
Cr	0.00	0.00	0.00	0.00	0.00	0.00	0.00	0.00	0.00	0.00	0.00	0.00	0.00	0.00	0.00	0.00
An	67.84	60.21	0.11	56.67	48.90	69.73	46.77	49.67	1.29	33.08	2.82	26.25	1.11	47.73	16.28	0.10
Ab	30.27	37.77	3.32	41.70	50.36	29.22	51.60	42.91	28.18	64.86	35.93	68.69	24.45	50.34	79.85	10.18
Or	1.89	2.02	96.57	1.63	0.74	1.05	1.63	7.42	70.53	2.06	61.25	5.06	74.44	1.93	3.88	89.72

Gb: gabbro; Mz-Gb: monzo-gabbro; Mz-Dr: monzo-diorite; Mz: monzonite; Sy: syenite; Sy-Gr: syenogranite

An: anortite; Ab: albite; Or: orthoclase

Supplementary Table 11: Trace elements partition coefficients (Kd) used in the FC model for the SS and SU suites. Values and references extracted by the GERM Database (earthref.org/KDD)

SS SUITE

STEP 1	K Feld	Ol	Amph	Opx	Cpx	Plag	Ap	Mt	Bt	Qz	Zirc
Rb	-	0.000179	-	0.0004	$8*10^{-5}$	0.008	-	0.011	-	-	-
Ba	-	0.05	-	0.0003	0.14	0.39	0.05	0.028	0.03	-	-
Th	-	$2.4*10^{-6}$	-	0.0002	0.00026	0.004	-	0.05	0.0014	-	-
Nb	-	$7*10^{-5}$	-	0.0001	1.24	1.3	-	1.8	0.088	-	-
La	-	0.03	-	0.0001	0.77	0.3017	21.7	0.45	0.7	-	-
Ce	-	0.01	-	0.005	0.53	0.167	11.2	0.016	-	-	-
Pb	-	0.0001	-	0.0001	0.008	0.94	-	0.38	0.1	-	-
Sr	-	0.00019	-	0.0001	0.56	2.48	1.3	0.11	0.7	-	-
Zr	-	0.00068	-	0.0005	0.16	0.0009	0.636	0.02	0.017	-	-
Y	-	0.009	-	0.003	0.245	0.16	-	0.0039	0.018	-	-

STEP 2	K Feld	Ol	Amph	Opx	Cpx	Plag	Ap	Mt	Bt	Qz	Zirc
Rb	0.11	-	0.0077	-	$8*10^{-5}$	0.008	-	0.011	1.52	-	-
Ba	-	-	0.044	-	0.00011	0.1	0.05	0.4	5.35	-	-
Th	0.02	-	0.5	-	0.29	0.19	17.1	0.42	0.31	-	-
Nb	-	-	0.006	-	0.0008	0.002	-	0.01	0.088	-	-
La	0.08	-	0.54	-	0.19	0.28	4.4	0.29	0.318	-	-
Ce	-	-	0.094	-	0.04	0.241	48	0.35	0.377	-	-
Pb	0.98	-	0.53	-	0.32	1.3	-	0.38	0.89	-	-
Sr	3.87	-	0.01	-	0.02	1.8	1.4	0.53	0.363	-	-
Zr	0.003	-	1.79	-	0.95	0.55	0.906	0.38	0.59	-	-
Y	0.5	-	0.4	-	3.28	0.51	-	0.84	0.6	-	-

STEP 3	K Feld	Ol	Amph	Opx	Cpx	Plag	Ap	Mt	Bt	Qz	Zirc
Rb	2.4	-	1	-	0.15	0.97	0.4	0.043	3.5	-	-
Ba	1.07	-	0.07	-	0.05	1.2	0.45	0.4	4.04	-	-
Th	0.3	-	0.45	-	3.44	0.382	41	13.1	2	-	22.1
Nb	3.4	-	1.25	-	0.03	0.88	-	-	4.6	-	-
La	0.026	-	2.06	-	21.7	0.0007	23.5	0.0029	0.76	-	1.4
Ce	0.02	-	0.094	-	0.044	0.15	52.5	26	11	-	23.5
Pb	1.37	-	0.53	-	0.13	0.4	0.03	2.9	0.1	-	7.5
Sr	6.7	-	3.56	-	0.0432	0.94	8	0.01	0.29	-	-
Zr	0.003	-	0.8	-	0.02	0.0009	0.636	0.02	0.09	-	-
Y	0.017	-	0.4	-	0.66	0.21	162	0.95	1.4	-	71.4

SU SUITE

STEP 1	K Feld	Amph	Cpx	Plag	Ap	Mt	Bt
Rb	0.659	0.58	0.3	0.3	0.4	0.15	2.48
Ba	-	0.6	0.15	0.56	0.3	0.12	3.68
Th	-	0.5	0.23	0.05	17.1	0.42	0.12
Nb	-	0.8	2.1	0.008	-	0.7	0.088
La	-	0.7219	0.77	0.49	21.7	0.45	0.7
Ce	-	0.98	1.31	0.57	52.5	0.42	0.377
Pb	-	0.12	0.008	2.453	-	2.9	0.1
Sr	-	0.188	0.5	3.2	1.3	0.11	0.7
Zr	-	0.127	1.53	0.27	0.636	1.78	0.017
Y	-	11.3	1.05	0.1	-	0.64	0.018

STEP 2	K Feld	Amph	Cpx	Plag	Ap	Mt	Bt
Rb	1.57	5.58	-	0.17	0.4	0.01	0.936
Ba	9.7	0.07	-	3.4	0.45	0.1	52
Th	0.007	0.06	-	0.001	-	0.01	0.03
Nb	0.16	4	-	2.5	-	-	4
La	0.1	2.06	-	0.23	27	29.6	15.1
Ce	0.06	4.23	-	0.34	31	9.7	4
Pb	4.1	9.77	-	2.2	-	1.3	2.1
Sr	7.3	0.01	-	10.89	8	0.01	0.2
Zr	0.003	0.047	-	0.0009	0.636	0.02	0.09
Y	0.017	4	-	0.022	-	3.21	1

Rb: Philpotts and Schnetzler (1970); Nagasawa and Schnetzler (1971); Hart and Brooks (1974); Ronov and Yaroshevskiy (1976); Matsui *et al.* (1977); Nash and Crecraft (1985); Villemant (1988); Mahood and Stimac (1990); McKenzie and O'Nions (1991); Green *et al.* (1993); Dunn and Sen (1994); Ewart and Griffin (1994); Latourrette *et al.* (1995); Bindeman *et al.* (1998); Marks *et al.* (2004); Adam and Green (2006)

Ba: Nagasawa and Schnetzler (1971); Ewart *et al.* (1973); Paster *et al.* (1974); Drake and Weill (1975); Okamoto (1979); Luhr and Carmichael (1980); Mahood and Hildreth (1983); Villemant (1988); Mahood and Stimac (1990); Beattie (1993); Green *et al.* (1993); Ewart and Griffin (1994); Skulski *et al.* (1994); Latourrette *et al.* (1995); Schmidt *et al.* (1999); Marks *et al.* (2004); Adam and Green (2006)

Th: Matsui *et al.* (1977); Larsen (1979); Luhr and Carmichael (1980); Villemant *et al.* (1981); Dostal *et al.* (1983); Mahood and Hildreth (1983); Luhr *et al.* (1984); Nash and Crecraft (1985); Bacon and Druitt (1988); Mahood and Stimac (1990); Stix and Gorton (1990); McKenzie and O'Nions (1991); Beattie (1993); Bea *et al.* (1994); Dunn and Sen (1994); Ewart and Griffin (1994); Latourrette *et al.* (1995); Salters and Longhi (1999); Wood and Trigila (2001); Marks *et al.* (2004); Adam and Green (2006)

Nb: Haskin *et al.* (1966); Nash and Crecraft (1985); McKenzie and O'Nions (1991); Nielsen (1992); Dalpe and Baker (1994); Dunn and Sen (1994); Ewart and Griffin (1994); Latourrette *et al.* (1995); Bindeman *et al.* (1998); Green *et al.* (2000); Johnson and Schwab (2004); Marks *et al.* (2004); Adam and Green (2006)

La: Dudas *et al.* (1971); Matsui *et al.* (1977); Luhr and Carmichael (1980); Watson (1980); Villemant *et al.* (1981); Mahood and Hildreth (1983); Fujimaki *et al.* (1984); Luhr *et al.* (1984); Nash and Crecraft (1985); Villemant (1988); Mahood and Stimac (1990); Stix and Gorton (1990); Nielsen *et al.* (1992); Wood and Trigila (2001); Marks *et al.* (2004); Adam and Green (2006)

Ce: Nagasawa (1970); Schnetzler and Philpotts (1970); Nagasawa (1973); Paster *et al.* (1974); Matsui *et al.* (1977); Luhr and Carmichael (1980); Reid (1983); Mahood and Hildreth (1983); Fujimaki *et al.* (1984); Luhr *et al.* (1984); Nash and Crecraft (1985); Lemarchand *et al.* (1987); Mahood and Stimac (1990); Stix and Gorton (1990); Bindeman and Davis (2000); Sisson (1994); Salters and Longhi (1999); Wood and Trigila (2001)

Pb: Leeman (1979); Nash and Crecraft (1985); McKenzie and O'Nions (1991); Bea *et al.* (1994); Dunn and Sen (1994); Ewart and Griffin (1994); Brenan *et al.* (1995); Latourrette *et al.* (1995); Marks *et al.* (2004); Adam and Green (2006); Aignertorres *et al.* (2007)

Sr: Philpotts and Schnetzler (1970); Nagasawa (1973); Villemant *et al.* (1981); Watson and Green (1981); Nash and Crecraft (1985); Bacon and Druitt (1988); Villemant (1988); Mahood and Stimac (1990); McKenzie and O'Nions (1991); Dunn and Sen (1994); Ewart and Griffin (1994); Vannucci *et al.* (1998); Marks *et al.* (2004); Adam and Green (2006)

Zr: Larsen (1979); Villemant *et al.* (1981); Fujimaki *et al.* (1984); Fujimaki (1986); Villemant (1988); Nielsen (1992); Kennedy *et al.* (1993); Dunn and Sen (1994); Ewart and Griffin (1994); Latourrette *et al.* (1995); Marks *et al.* (2004); Adam and Green (2006)

Y: Larsen (1979); Ronov and Yaroshevskiy (1976); Nash and Crecraft (1985); Nielsen *et al.* (1992); Green *et al.* (1993); Bea *et al.* (1994); Ewart and Griffin (1994); Hack *et al.* (1994); Latourrette *et al.* (1995); Sobolev *et al.* (1996); Nikogosian and Sobolev (1997); Wood and Trigila (2001); Adam and Green (2006)

Supplementary Table 12: Mass balance calculation and FC modelling for SS suite.

	STEP 1	r^2 =	0.89		STEP 2	r^2 =	0.68		STEP 3	r^2 =	0.26	
	FROM	TO	S.A.	NATURAL	FROM	TO	S.A.	NATURAL	FROM	TO	S.A.	NATURAL
	Mz-Gb	Mz-Gb	Gb	Gb	Mz-Gb	Mz	Mz-Gb	Mz-Gb	Mz	Sy	Mz-Dr	Mz-Dr
% Oxides	FC43B	EM53	SA1SS	FC30A	EM53	EM85	SA2SS	232	EM85	EM110	SA3SS	214
SiO_2	50.44	53.71	47.89	46.66	53.71	61.28	50.98	51.10	61.28	65.08	57.27	56.77
TiO_2	1.09	0.84	0.72	1.10	0.84	0.70	0.95	1.46	0.70	0.57	0.77	0.78
Al_2O_3	16.59	17.46	16.10	16.51	17.46	17.06	17.57	17.76	17.06	17.45	16.74	18.94
FeOtot	9.87	8.59	10.96	11.29	8.59	5.22	9.78	10.06	5.22	2.92	7.82	7.15
MgO	6.15	4.12	8.05	8.01	4.12	2.29	4.83	5.79	2.29	1.20	3.49	2.78
CaO	10.63	8.45	12.53	13.71	8.45	4.56	9.80	7.82	4.56	1.67	7.83	7.45
Na_2O	2.35	2.77	1.81	0.85	2.77	2.86	2.91	2.53	2.86	2.63	2.88	2.12
K_2O	1.89	3.42	0.94	1.81	3.42	5.66	2.53	2.87	5.66	8.36	2.73	3.56
P_2O_5	0.77	0.49	0.97	0.06	0.49	0.26	0.62	0.60	0.26	0.07	0.46	0.45
tot	100	100	100	100	100	100	100	100	100	100	100	100
	SA1SS (Gb)				SA2SS (Mz-Gb)				SA3SS (Mz-Dr)			
K-Feld	0.00	0.00			4.55	6.24			7.75	16.32		
Ol	4.54	8.33			0.00	0.00			0.00	0.00		
Amph	0.00	0.00			0.49	0.67			1.26	2.65		
Opx	2.76	5.07			0.00	0.00			0.00	0.00		
Cpx	11.61	21.31			12.80	17.57			5.73	12.07		
Plag	26.90	49.38			38.03	52.19			19.90	41.90		
Ap	1.24	2.28			1.01	1.39			0.51	1.07		
Mt	1.92	3.52			3.89	5.34			1.93	4.06		
Bt	5.50	10.10			12.10	16.60			5.00	10.53		
Qz	0.00	0.00			0.00	0.00			5.05	10.63		
Zirc	0.00	0.00			0.00	0.00			0.36	0.76		
tot	54.47	100.00			72.87	100.00			47.49	100.00		
	C_0	C_L nat.	C_L calc.	Err %	C_0	C_L nat.	C_L calc.	Err %	C_0	C_L nat.	C_L calc.	Err %
Rb	51	114	111	-2.32	114	301	304	0.94	301	260	262	0.86
Ba	275	504	504	-0.09	504	530	530	0.07	530	481	487	1.16
Th	3	12	7	-41.43	12	21	24	13.26	21	9	11	20.08
Nb	8	8	8	1.69	8	31	29	-6.27	31	24	24	0.10
La	16	14	17	24.01	14	32	34	6.63	32	8	9	15.90
Ce	39	60	60	0.29	60	70	70	0.32	70	19	19	-0.05
Pb	16	24	24	0.05	24	26	27	1.55	26	34	34	0.11
Sr	1140	801	801	0.00	801	554	547	-1.32	554	350	352	0.62
Zr	75	160	161	0.36	160	270	271	0.21	270	507	504	-0.55
Y	14	28	28	0.25	28	24	27	13.85	24	8	8	0.75

Gb: gabbro; Mz-Gb: monzo-gabbro; Mz-Dr: monzo-diorite; Mz: monzonite; Sy: syenite

S.A.: subtracted solid assemblage; NATURAL: sampled PIC lithotype; r^2: least squares error

C_0: trace element starting concentration; C_L nat.: trace element arrive natural concentration

C_L calc.: trace element arrive calculated concentration; Err %: percentage of error

Supplementary Table 13: Mass balance calculation FC modelling for SU suite.

	STEP 1	r^2 =	0.98		STEP 2	r^2 =	0.73	
	FROM	TO	S.A.	NATURAL	FROM	TO	S.A.	NATURAL
	Mz-Gb	Mz	Gb	Gb	Mz	Sy	Mz-Dr	Mz-Dr
% Oxides	EM10	EM7	SA1SU	255	EM7	11*	SA2SU	FC2
SiO_2	49.90	56.81	45.76	46.00	56.81	59.90	53.22	53.51
TiO_2	0.93	0.59	1.10	0.87	0.59	0.38	0.25	1.16
Al_2O_3	17.93	21.42	15.86	21.07	21.42	21.77	21.24	16.38
FeOtot	10.12	4.11	13.65	9.82	4.11	2.98	5.57	7.31
MgO	4.98	1.39	6.98	6.19	1.39	0.42	2.80	5.14
CaO	9.57	5.11	12.36	11.65	5.11	2.90	7.70	8.51
Na_2O	2.82	5.22	1.73	0.37	5.22	6.31	3.56	5.13
K_2O	2.81	4.86	1.80	3.95	4.86	4.98	4.63	2.52
P_2O_5	0.76	0.25	0.73	0.07	0.25	0.06	1.01	0.33
tot	100	100	100	100	100	100	100	100
	SA1SU (Gb)				SA2SU (Mz-Dr)			
K Feld	2.98	4.76			14.15	32.12		
Amph	7.65	12.23			6.44	14.62		
Cpx	17.20	27.49			0.00	0.00		
Plag	22.43	35.85			19.49	44.25		
Ap	1.06	1.69			1.04	2.36		
Mt	6.85	10.95			1.79	4.06		
Bt	4.39	7.02			1.14	2.59		
tot	62.56	100.00			44.05	100.00		
	C_0	C_L nat.	C_L calc.	Err %	C_0	C_L nat.	C_L calc.	Err %
Rb	95	188	188	-0.10	188	234	233	-0.38
Ba	459	853	852	-0.10	853	329	329	0.00
Th	23	44	46	3.54	44	102	79	-22.90
Nb	15	26	25	-3.46	26	29	29	-0.07
La	78	113	117	3.35	113	102	102	0.11
Ce	179	171	174	1.64	171	182	182	0.22
Pb	69	88	87	-1.11	88	52	59	13.67
Sr	1054	1194	1197	0.28	1194	325	325	-0.06
Zr	160	269	271	0.82	269	477	481	0.79
Y	36	31	32	4.02	31	46	46	-0.57

Gb: gabbro; Mz-Gb: monzo-gabbro; Mz-Dr: monzo-diorite; Mz: monzonite; Sy: syenite

S.A.: subtracted solid assemblage; NATURAL: sampled PIC lithotype; r^2: least squares error

C_0: trace element starting concentration; C_L nat.: trace element arrive natural concentration

C_L calc.: trace element arrive calculated concentration; Err %: percentage of error